BNWL-2216
UC-32

Investigation of Combined Free and Forced Convection in a 2 x 6 Rod Bundle

by
M. S. Quigley
C. A. McMonagle
J. M. Bates

July 1977

Prepared for the Energy Research and Development Administration under Contract EY-76-C-06-1830

Battelle
Pacific Northwest Laboratories

BNWL-2216

NOTICE

PACIFIC NORTHWEST LABORATORY
operated by
BATTELLE
for the
ENERGY RESEARCH AND DEVELOPMENT ADMINISTRATION
Under Contract EY-76-C-06-1830

Printed in the United States of America
Available from
National Technical Information Service
U.S. Department of Commerce
5285 Port Royal Road
Springfield, Virginia 22151
Price: Printed Copy $_____*; Microfiche $3.00

*Pages	NTIS Selling Price
001-025	$4.50
026-050	$5.00
051-075	$5.50
076-100	$6.00
101-125	$6.50
126-150	$7.00
151-175	$7.75
176-200	$8.50
201-225	$8.75
226-250	$9.00
251-275	$10.00
276-300	$10.25

FRDA-3: RICHLAND, WA

BNWL-2216
UC-32

INVESTIGATION OF COMBINED FREE AND FORCED CONVECTION IN A 2 x 6 ROD BUNDLE

by
M. S. Quigley
C. A. McMonagle
J. M. Bates

APPROVED BY _____
A. M. Sutey, Manager
Energy Systems Engineering Section

APPROVED BY _____
D. S. Trent, Manager
Fluid & Thermal Engineering Section

July 1977

BATTELLE
Pacific Northwest Laboratories
Richland, Washington 99352

SUMMARY

An experimental study was performed to obtain developing fluid temperature and detailed velocity measurements in combined free and forced convection flows within an electrically heated rod bundle containing steep radial power distributions. Mixed convection flows and steep radial power gradients are expected in the radial blanket of a Liquid Metal Fast Breeder Reactor (LMFBR), and it is important to predict thermal-hydraulic phenomena under these conditions. The objective of this study was to provide a data base for verification of thermal hydraulic computer codes. To meet this objective it was not necessary for this experiment to be completely prototypic of an assembly in the LMFBR radial blanket. Instead, a relatively simple rectangular rod bundle geometry without wire wraps was used. In addition, water was used rather than sodium so that measurements of the detail required for code verification could more easily be obtained in a flow having the basic buoyancy-dominated character of interest.

The experimental rod bundle contained twelve electrically heated rods in a 2 x 6 rectangular array. The rods were 0.475 in. in diameter with a 4-ft uniformly heated length and were spaced on a 0.575-in. pitch. The 12 rods were divided into two groups of six, each forming a 2 x 3 array which were connected to different, independently controlled power supplies. In this manner, radial power distributions of interest were established by setting the two power supplies at the desired values. The rod bundle was contained within a stainless steel flow housing having nine equally spaced windows located along its length. At these axial positions, detailed velocity profiles were measured with a one-dimensional laser Doppler anemometer (LDA) and fluid temperatures of the central subchannels were taken. This experiment was the first known attempt to apply the LDA velocity measurement technique to mixed free and forced convection in rod bundle flows.

Experiments were performed at bundle average temperatures from 60°F to 75°F with bundle average Reynolds numbers between 500 and 1500 and radial power distributions of 0:0, 1:0 and 2:1. These conditions spanned a range of buoyancy importance from isothermal flow (no buoyancy effects)

to buoyancy-dominated flow. Under isothermal conditions, velocity profiles at a given axial location were generally symmetrical, with peaking in subchannel centers. When the radial power distribution was applied, flow redistributed from the cold side of the bundle to the hot side. The distortion in the velocity and temperature profiles was a direct result of the increased buoyancy forces and was dependent on the Reynolds number and radial power distribution. At a given Reynolds number, the velocity and temperature profiles were more uniform at lower values of power skew, indicating less significant buoyancy effects. Likewise, for a selected power skew the profiles were more uniform at higher Reynolds numbers corresponding to decreased buoyancy importance. These results are consistent with other studies. At all values of Grashof and Reynolds number investigated including a case where recirculation occurred in the upper levels of the bundle, the inlet flow split was independent of downstream conditions.

During heated tests, thermal plumes were observed around the rods. These plumes were stable at low heating rates, but were turbulent and dynamic at high powers as evidenced both visually and by the time history of thermocouples located at subchannel centers. Results indicate that significant temperature gradients may have existed between subchannel centers and the heater rods. However, these suspected gradients were not measured because temperature measurements were made only at subchannel centers.

The magnitude and dynamic character of these density gradients caused considerable difficulty in making the LDA velocity measurements. The laser beams were often independently and dynamically deflected from their original courses. This caused measuring difficulty near the rods. Therefore, reported velocities are generally limited to profiles midway between rods or midway between a heater rod and the flow housing wall where density gradient disturbances were a minimum.

The COBRA computer code was used to numerically simulate all experimental cases. The code accurately predicted average subchannel velocities in mixed convection rod bundle flows even in regions with steep velocity gradients. COBRA also predicted a flow recirculation that was verified by

temperature measurements. Although subchannel average temperatures computed with COBRA showed the same trends as temperatures measured at subchannel centers, the magnitudes were different. A reason for these differences could be temperature gradients within the subchannels which would cause the average and point values to be different. Because COBRA comparisons with the velocity data were very good, it is thought that the computed temperatures are reasonable; however, more detailed local temperature gradient data are required to further test this hypothesis.

CONTENTS

FIGURES

TABLES

INVESTIGATION OF COMBINED FREE AND FORCED CONVECTION IN A 2 x 6 ROD BUNDLE

1.0 INTRODUCTION

This report documents a study performed by the Pacific Northwest Laboratory (PNL) for the Energy Research and Development Administration (ERDA). The experiment was designed to provide velocity and temperature data in a rod bundle geometry with low Reynolds number flows and severe radial power gradients. These data were then used to verify predictions by the COBRA computer program[1] in the combined free and forced convection flow regime. Comparable flow conditions may occur in the radial blanket of a Liquid Metal Fast Breeder Reactor (LMFBR), in which radial power gradients up to 4:1 may exist across an assembly. Under low flow rate conditions the power gradient may cause significant buoyancy forces potentially resulting in flow redistribution within the radial assemblies. Consequently, there is a need to evaluate whether available thermal-hydraulic design codes can accurately predict the corresponding temperature and velocity profiles.

Previous numerical analyses have simulated buoyancy-dominated flows in parallel plate geometries[2] and hexagonal wire-wrapped rod bundles[3] subjected to radial heat flux profiles. Results of these studies show that the Reynolds number, radial power gradient and the ratio of Grashof number to the square of Reynolds number (GR/Re^2) are of fundamental importance in the development of velocity and temperature distributions. The velocity and temperature profiles for most cases were shown to skew toward the higher power side of the channel, with the skewness dependent on the Reynolds number and the radial power distribution. For a given power skew, the velocity distribution was more uniform at higher Reynolds number, indicating less significant buoyancy effects. Conversely, at a given Reynolds number the buoyancy forces became more dominant and the velocity profile more distorted at higher power skew values. The range of radial power distribution investigated by Khan et al.[3] was not large enough to conclusively show the relationship between temperature profile and power skew in a hexagonal

wire-wrapped rod bundle, but Tsai et al.[2] reported their temperature profiles for a thin rectangular channel were generally flat except for Re $\geq$ 2000 when the temperature profile followed the power skew. Those authors also predicted that the temperature profiles would be noticeably more distorted if wall shear were included in the analysis because the velocity distribution would be more uniform. This effect was observed by Khan et al.[3] who showed that frictional drag considerably reduced the skewness in the velocity profile.

Another important result of these analyses was to show the dependence of buoyancy effects on the parameter GR/Re^2. Buoyancy effects became more noticeable as GR/Re^2 increased to the mixed convection regime. Khan et al.[3] utilized a modified form of this term, GR*, to account for the increased mixing caused by wire wraps and the rod bundle peak to average power ratio. Based on the results of that study it was suggested that $GR^*_C = 0.025$ is a critical value below which buoyancy effects are unimportant. When GR* > 0.025, the assembly is operating in the mixed convection regime and buoyancy effects should be considered.

A series of sodium experiments has been planned or completed to measure temperature distributions in complex electrically heated rod bundle simulations of LMFBR fuel and radial assemblies. These include the Westinghouse Advanced Reactor Division 61-pin, the Oak Ridge National Laboratory 19-pin, and the Hanford Engineering Development Laboratory 217-pin electrically heated rod bundle experiments. Although these experiments are prototypic of LMFBRs, they do not provide the detailed velocity profile measurements necessary to fully evaluate thermal-hydraulic code performance. Temperature measurements alone cannot be used with a high degree of confidence to calculate the velocity distributions in the mixed convection flows.

The purpose of this study was to provide temperature and detailed velocity profiles for subchannel code comparisons. The experimental program was designed to produce a given combination of the parameters Re, Q_H/Q_L and GR/Re^2 by controlling the flow conditions in a rod bundle geometry. For this study, the Reynolds number, $Re = UD_H/\nu$, was based on the average bundle flow rate, mean temperature, and total hydraulic diameter of the

flow housing. A modified Grashof number, $GR^* = [(g\beta\Delta T_B D_H^3)/\nu^2](\overline{Q} - 1)$, was formed by multiplying the bundle average GR by a radial power distribution factor, $(\overline{Q} - 1)$. The radial power distribution factor had a range $0 \leq (\overline{Q} - 1) \leq 1$, indicating the severity of the power skew from a uniform distribution, $(\overline{Q} - 1) = 0$, to an infinite distribution, $(\overline{Q} - 1) = 1$. $\overline{Q}$ was defined as $2Q_H/(Q_H + Q_L)$ where Q_H is the hot side rod power and Q_L is the cool side rod power. The ratio of buoyant forces to frictional forces, GR^*/Re^2, was identical to the similarity parameter, GR^*, discussed by Khan et al., except for the wire-wrap mixing terms. It was not determined in this study whether the critical value of GR^*, $GR^*_C = 0.025$, proposed by those authors as the transition between pure forced convection and mixed convection, applies to rod bundles like the one used for this study. Nevertheless, when GR^*/Re^2 is relatively large, the buoyancy effects are important and the bundle is operating in the mixed convection regime.

A rectangular rod bundle without wire wraps was chosen for this experiment rather than the LMFBR wire-wrapped hexagonal rod array because geometric simplicity was desirable and laser Doppler anemometer (LDA) measurements could not be made in an electrically heated wire-wrapped bundle. Water, the modeling fluid for these tests, simulated the Reynolds numbers and Grashof numbers of liquid sodium, but the differences in Prandtl number (Pr) were large and could not be modeled. This experiment was conducted for code verification in the mixed convection flow regime governed primarily by Re and GR. Since sodium Re and GR can be reasonably approximated by water, significant data for the purpose of code verification can be obtained. In addition, water has several obvious advantages over liquid sodium as a modeling fluid for this study. A few of these are:

1. low temperature and pressure;
2. no "exotic" materials required in the flow facility;
3. optical transparency for LDA velocity measurement;
4. low cost, ready availability;
5. no special handling requirements, minimal safety hazards;
6. well-defined properties and characteristics.

The conclusions and recommendations stemming from this investigation's results are presented and discussed in Section 2.0. The equipment and

experimental procedure are fully described in Section 3.0. Section 4.0 details the operating conditions under which the experiment was conducted. In Section 5.0, the accuracy of the data obtained under each test condition is discussed. Results of the investigation are presented in Section 6.0, with full discussions of the velocity and temperature profiles obtained. In Section 7.0, the experimentally-obtained velocity and temperature data are compared with COBRA computer code predictions of those parameters.

2.0 CONCLUSIONS AND RECOMMENDATIONS

This experiment provided velocity and temperature data in a rod bundle geometry with low Reynolds number flows and severe radial power gradients for comparison with predictions by the COBRA computer program in the combined free and forced convection flow regime. These buoyancy-dominated flow conditions, of the type encountered in the radial blanket of an LMFBR, were simulated using water and a rectangular bundle of smooth rods. Direct simulation of mixed convection flow in a sodium-cooled hexagonal wire-wrapped array was not possible since water cannot model the sodium Prandtl number. However, the parameters governing the free and forced convection regime are the Reynolds number (frictional forces) and the Grashof number (buoyancy effects) which can be modeled by water. The rectangular array of smooth electrical heater rods allowed the local mean axial velocity to be measured using a laser Doppler anemometer. The local temperature profile was measured at the same axial locations as the LDA measurements using a thermocouple rake. These data were compared to COBRA predictions of the subchannel average velocity and temperature for the corresponding flow and boundary conditions. These comparisons were made over a range of relative buoyancy importance indicated by the parameter GR^*/Re^2. In this case the modified Grashof number includes the effect of the radial power distribution on the buoyancy forces. When GR^*/Re^2 increased above zero the buoyancy effects became significant compared to frictional effects and the assembly operated in the mixed convection regime.

The experimental and analytical data indicate that as the ratio of buoyancy forces to frictional forces increased from the forced convection regime to the mixed convection regime, the axial flow redistributed with more fluid flowing through the heated regions. The distortion in the velocity and temperature profiles was a direct result of the increased buoyancy forces and was dependent on the Reynolds number and the radial power distribution. At a given Re the velocity and temperature profiles were more uniform at lower values of power skew, indicating less significant buoyancy effects. Likewise, for a selected power skew the profiles

were more uniform at higher Re corresponding to decreased buoyancy importance. These results are consistent with those of other studies.[2,3] These changes in the temperature and velocity distributions occurred downstream of the entrance to the heated length. For all values of GR^*/Re^2 investigated, including a case where recirculation occurred in the upper levels of the bundle, the inlet flow split was independent of the downstream conditions.

The time-dependent nature of the temperature data produced from thermocouples inserted into the rod bundle central subchannels indicates steep thermal gradients existed between the heater rods and the center of the subchannels. These gradients were not quantified by detailed measurements but visual observations confirmed the presence of dynamic thermal plumes around each heated rod. These plumes gradually expanded in size with increasing elevation until they merged together approximately one-half to two-thirds the axial length from the inlet. The motion of these plumes was analogous to a plume of smoke in still air that makes the transition from laminar to turbulent a certain distance from its source. Until the plumes merged, their motion was relatively smooth and undisturbed. After mixing, the region between the rods appeared to be highly turbulent even though the flow Reynolds number indicated a laminar condition for the bundle. These dynamic gradients created approximately ± 5 percent uncertainty in the temperature measurement. Because a detailed profile was not made, the temperature data for this experiment are considered a qualitative measure of the temperature distribution.

This experiment was the first known attempt to apply the LDA velocity measurement technique to mixed free and forced convection in rod bundle flows. The density gradients observed were not only responsible for the buoyancy effects investigated but also caused considerable difficulty in making the LDA measurements. When the two laser beams entered the dynamic thermal plumes surrounding the rods, they were each randomly deflected in different directions. The amount of deflection depended on the severity of the density gradient and the apparent turbulent intensity of the plumes. This often caused a large uncertainty in the location of the probe volume and unacceptable scatter in the velocity data. The net result was that LDA

velocity measurements were restricted to a narrow region along the centerline between the heater rods or between the rods and the flow housing walls. In this region the thermal plumes were not merged together (lower elevations) or were completely mixed (higher elevations) so that the probe volume movement was minimized. Because measurements were only taken when these effects were small, reasonably detailed and accurate velocity profiles were generated.

2.1 CONCLUSIONS

The specific conclusions resulting from this investigation are listed below by experimental condition.

Isothermal Flow

- The velocity profiles show a strong dependence on Reynolds number. As Re increased, the ratio between peak to average velocity for a given traverse decreased.
- All velocity profiles exhibit regular, orderly peak spacing indicating a uniform radial heater rod spacing.
- For a given axial location, the velocity profiles in the side channels exhibited some skewing, demonstrating that the rod bundle was not perfectly aligned with the flow housing. This effect is not thought to be significant for the central subchannel data reported.

Heated Cases

- The effects of rod bundle geometry on the velocity distribution were magnified in the mixed convection flows.
- Velocity profiles in heated subchannels are more uniform than the isothermal distribution.
- The amount of uniformity in the subchannel local velocity profiles corresponds to the degree of visually observed thermal plume interaction. As the apparent turbulence of the plumes increased, the ratio of local maximum to minimum velocity within a subchannel decreased.
- The ratio of hot side average velocity to cold side average velocity increased with elevation, corresponding to a continuous buoyancy-dominated development of the velocity profile.

- The distortion of the isothermal velocity and temperature profiles increased with increasing GR^*/Re^2.
- Case 2 velocity and temperature profiles indicate reverse flow occurred near the rod bundle exit plane. It was impossible to measure the velocity at that location to confirm this observation; however, the temperature data support the conclusion that a flow reversal took place.
- The velocity and temperature profiles at the entrance to the heated length were identical to the corresponding isothermal profiles for each case. Therefore the inlet flow split was independent of downstream conditions.
- In every case, the temperature measured in the subchannel nearest the window on the hotter side of the bundle (Subchannel 8) appears low and cannot be explained.
- Temperatures fluctuated in time as much as ± 5 percent about a mean value, with a period roughly equal to the period of motion observed in the thermal plumes.
- Insufficient data exist to quantify the suspected steep temperature gradients across the subchannels.

The COBRA computer code was used successfully to predict the velocity and temperature distributions corresponding to the three experimental heated cases. The subchannel average velocities calculated by COBRA compared favorably in magnitude and trends to the LDA point measurements. However, the computed temperatures generally did not agree well with the measured data except in the shape and trends of the temperature profile. The discrepancy between the analytical and experimental temperature data is probably a result of the steep thermal gradients observed visually in the flow.

Specific conclusions resulting from the COBRA analysis of the experimental data are listed below.

- COBRA can accurately predict the velocity distributions in mixed convection rod bundle flows even in regions with steep velocity gradients. No additional or special correlations or modifications were necessary to provide good agreement with the experimental measurements.

- The code predicted reverse flow for experimental case 2 in the exit plane of the rod bundle. The flow reversal was verified by experimental measurements.
- Because COBRA correctly computed the velocity distribution, it probably did a reasonable job of calculating the temperature profile. However, there are insufficient experimental data for a complete evaluation.

2.2 RECOMMENDATIONS

Based on evaluation of the results of this study, it is recommended that the following investigations be undertaken:

- The temperature gradients in mixed free and forced convection flows suggested by the thermal plumes observed in the present experiment should be quantified. Sufficient temperature measurements should be made in each subchannel to accurately characterize the temperature distribution and give a reasonable average value to compare with the COBRA predictions.
- Although the present study illustrates COBRA's ability to predict the average velocity compared to point velocity measurements, an attempt should be made to measure the local velocity at enough points in the subchannel to provide a statistical average for direct comparison with COBRA. This may require the development of a nondisturbing velocity probe or measurement technique less sensitive to thermal gradients than the LDA described in this work.

3.0 EQUIPMENT AND EXPERIMENTAL PROCEDURE

This experiment was conducted in the flow facility shown in Figure 3-1. A detailed description of this facility, instrumentation, and experimental procedure is presented in the following paragraphs.

3.1 FLOW FACILITY

The basic equipment consisted of a 2 x 6 electrically heated rod bundle enclosed in a rectangular flow housing connected to an open water flow loop.

3.1.1 Flow Loop

A schematic of the once-through flow loop is Figure 3-1. During operation, deaerated water was drawn from a 50-gallon head tank and pumped through approximately 100 ft of coiled rubber hose into the flow housing inlet piping. The flexible hose helped damp out vibration and pump-induced flow oscillations. Valving at the test section inlet and outlet provided a constant flow rate and system pressures to 60 psia.

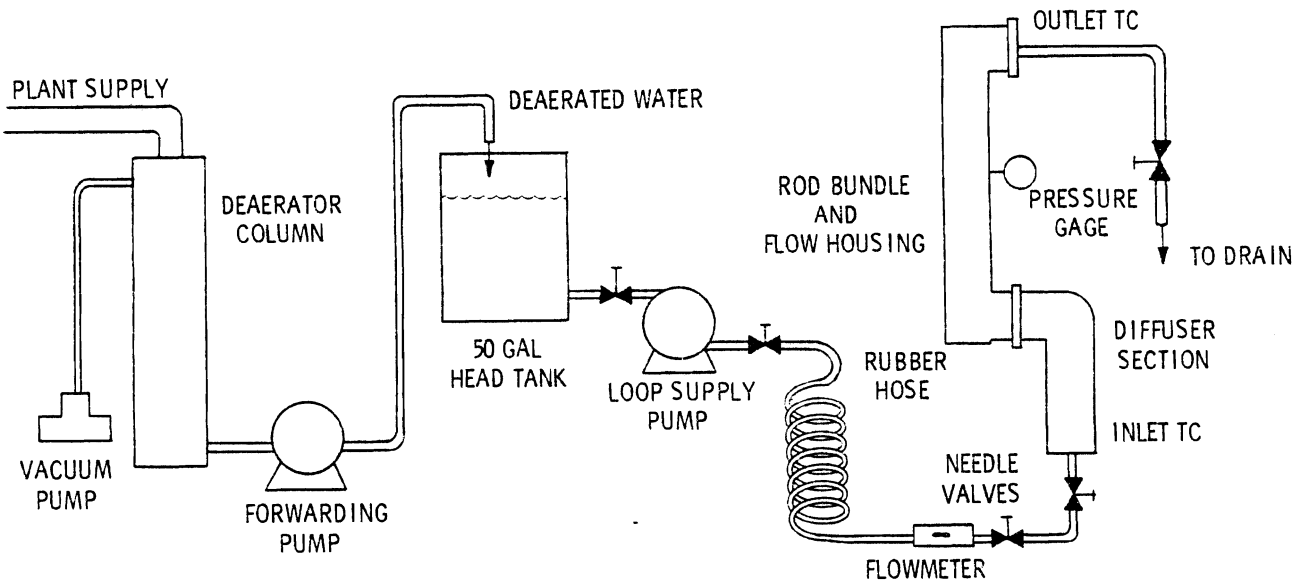

FIGURE 3-1. Flow Loop

3.1.2 Rod Bundle

Figure 3-2 shows a cross section of the 2 x 6 rod bundle used in this experiment. Three subchannel types are defined: central, side, and corner. As shown, these subchannels are interconnecting regions whose borders are defined by the heater rod periphery and/or the flow housing walls.

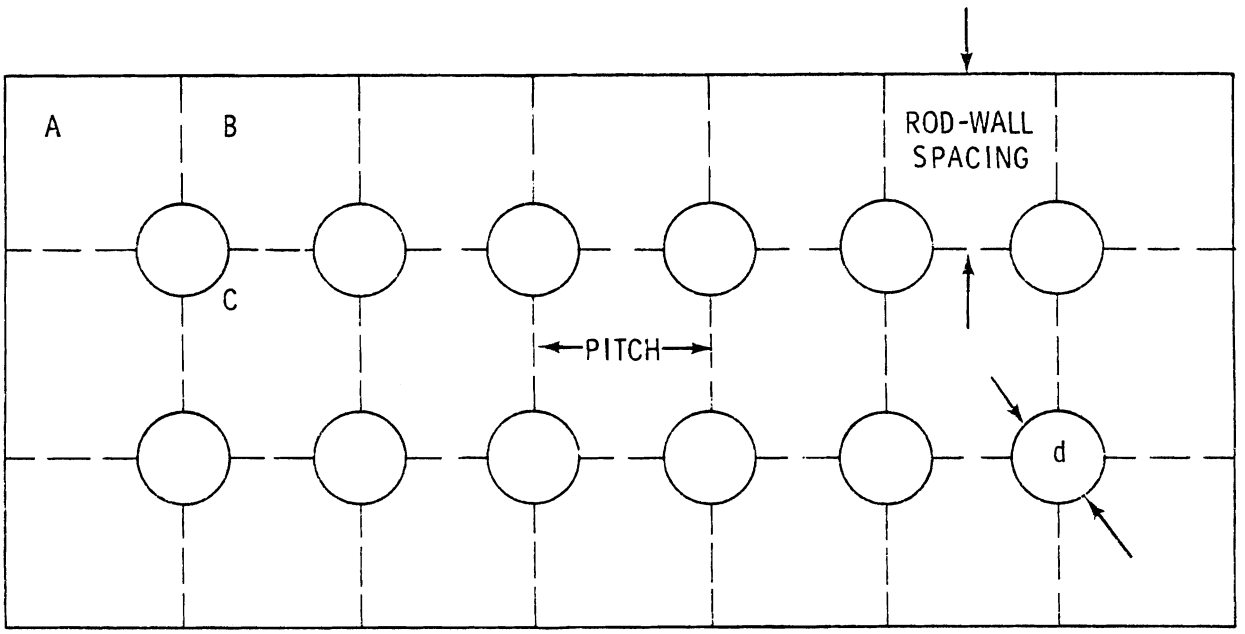

REGION	SUBCHANNEL DESCRIPTION
A	CORNER
B	SIDE
C	CENTRAL

FIGURE 3-2. Subchannel and Distance Definitions

Subchannels were sized such that an equal enthalpy rise would be obtained in the side and adjacent central subchannels. In this manner, major gradients remained in the long dimensions of the rod bundle, minimizing flow housing effects. Pretest computations using the COBRA code confirmed that the 2 x 6 rod bundle would be sufficiently large for this study. The rod bundle dimensions and orientation with respect to the

reference coordinate system are illustrated in Figure 3-3. The nomenclature used for this and all subsequent figures is presented in Appendix A. In the radial direction, x = 0 corresponds to the window on the side of the bundle where the LDA traverses began. In Figure 3-3, this is the left side of the figure; the laser beams enter the bundle from the right. The x-axis, y = 0, was oriented along the centerline between the two rows of heater rods and y = $\pm$0.586 were the centerlines of the side subchannels.

3.1.3 Flow Housing

Figure 3-4 illustrates the flow housing used for the experiment. The 2 x 6 rod bundle was contained within a rectangular stainless steel flow housing constructed of face plates, sides, and a top and bottom. Nine windows located in the face plates at 6-in. intervals over the 4-ft test section permitted visual access for the LDA measurements in addition to access for the thermocouple rake. The top and bottom plates of the flow housing contained twelve 0.25-in. diameter holes to allow for the passage of heater rod extensions. All joining surfaces were sealed with O-rings to accommodate internal pressures to 60 psia.

3.1.4 Heater Rods

One of the internal resistance type heater rods used in the experiment is shown in Figure 3-5.

The 0.475-in. diameter rods, manufactured by Rama Corporation, had a uniformly heated 4-ft length rated at 1.0 kW/ft and a total length of 5 ft. They were held in position at five places along their length. Spacers were provided at the beginning, midpoint, and end of the heated section, and the heaters were fixed at one end of the housing and held in tension at the other to allow for thermal expansion. Extensions, as shown, allowed electrical connections to pass through the flow housing.

Two 25-kVA three-phase variacs provided power for the heater rods.

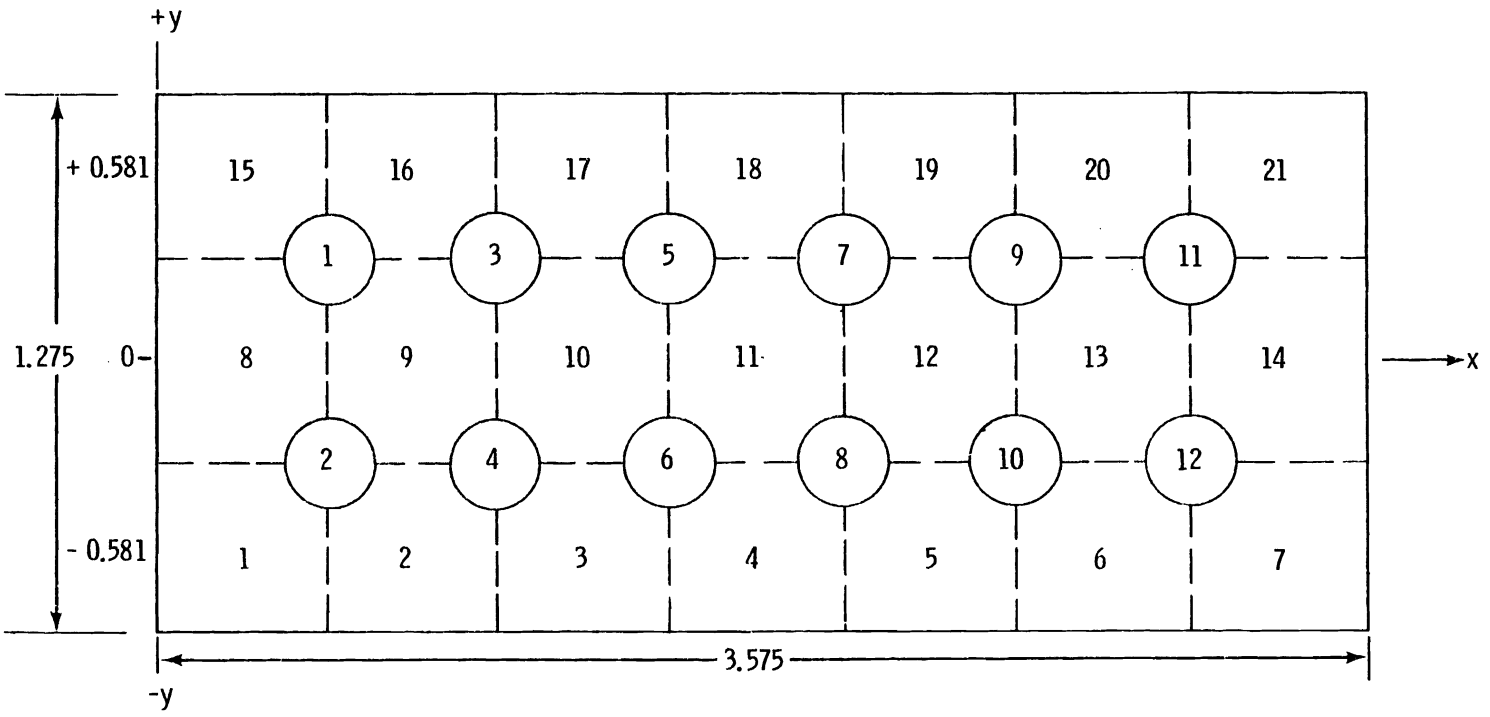

ROD DIAMETER, d = 0.475
PITCH, p = 0.575

ROD-WALL SPACING = 0.350

SUBCHANNEL DIMENSIONS

TYPE	AREA ($in.^2$)	WETTED PERIMETER (in.)	HEATED PERIMETER (in.)
CORNER	0.0782	1.073	0.3731
SIDE	0.1127	1.321	0.7461
CENTRAL	0.1534	1.492	1.492

FIGURE 3-3. Subchannel Number and Dimensions

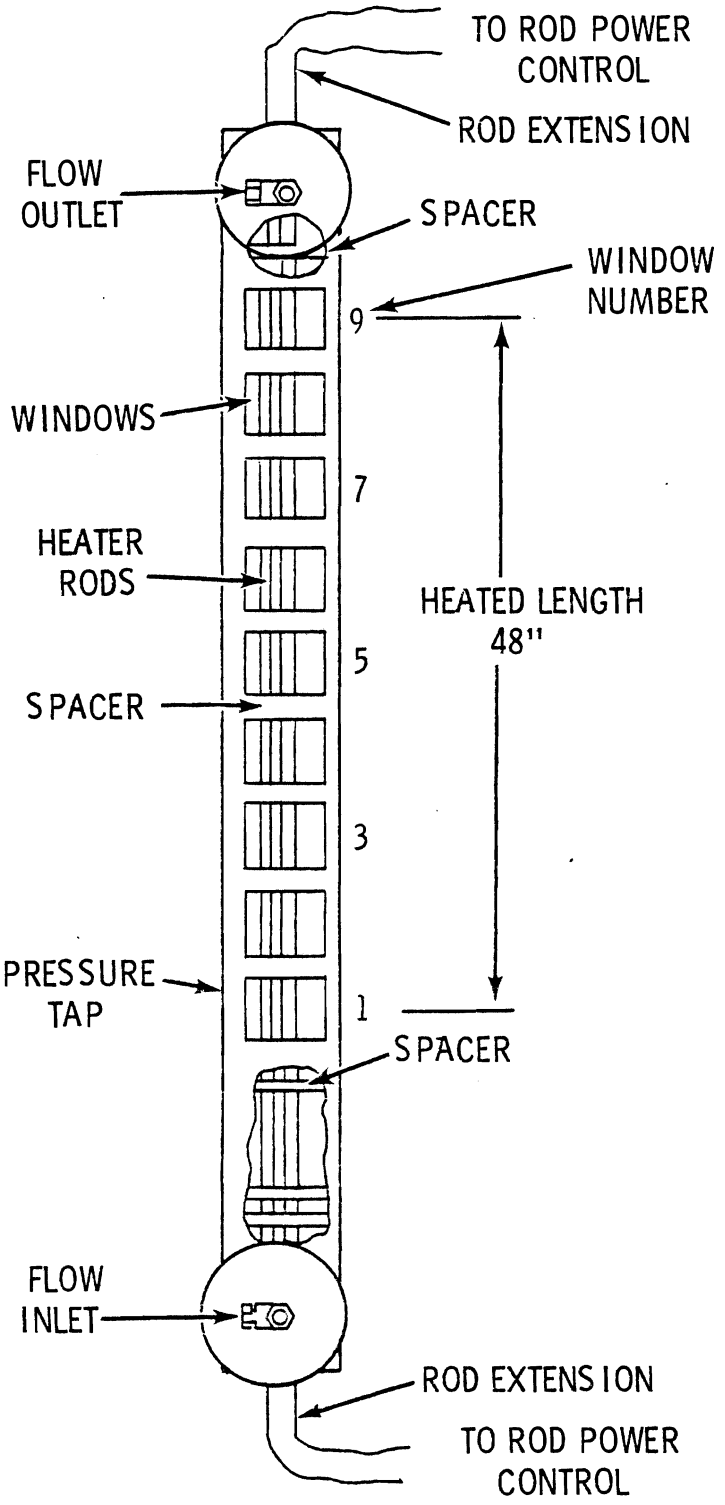

FIGURE 3-4. Flow Housing

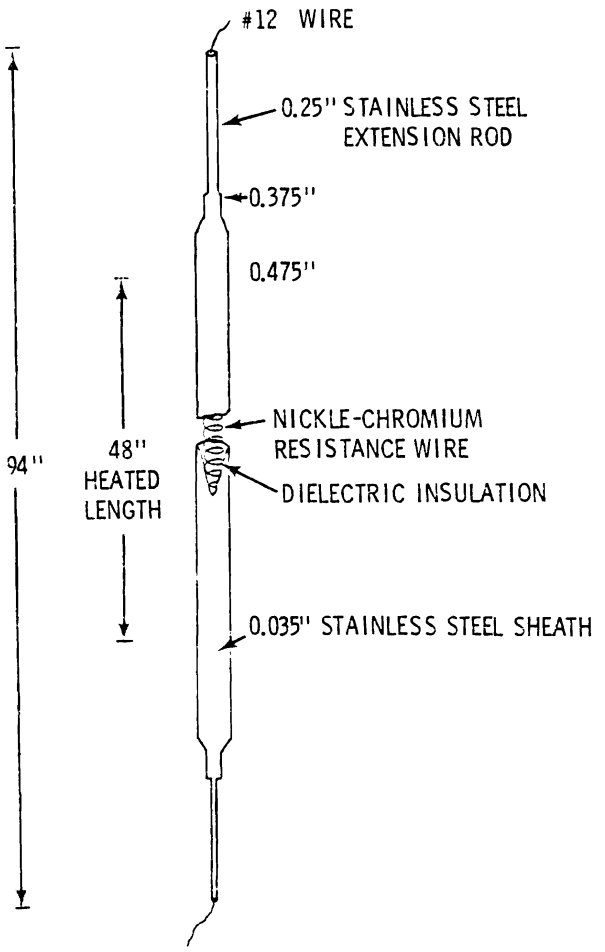

FIGURE 3-5. Heater Rod

3.2 INSTRUMENTATION

For each test condition, fluid velocity and temperature were measured both axially and laterally within the heated length of the rod bundle. Rod power was determined by measuring the voltage and current for each of the twelve heater rods, and the bundle flow rate and inlet and outlet temperatures were continuously monitored.

3.2.1 Velocity Measurements

A laser Doppler anemometer (LDA) was used to measure local velocities. For this experiment, the two most important advantages of the LDA approach were that the probe volume did not disturb the flow field and the instrument was easy to calibrate.

Figure 3-6 is a schematic of the LDA apparatus. A 15-mW Spectra-Physics HE-NE laser Model 124 was the laser beam source. A beam splitter split the incoming beam into two beams which were unequally frequency-shifted by the Bragg cells and focused to a probe volume approximately 0.009 in. in diameter and 0.115 in. long. This Bragg cell frequency shift provided a reference frequency offset to the LDA signal so that it was possible to measure zero or negative velocity without ambiguity. Light-scattering particles moving within the water encountered the interference fringe pattern within the intersection probe volume and the resulting scattered light was Doppler-frequency shifted with respect to the incident laser light frequency. The collecting optics gathered and focused this scattered light onto the photomultiplier tube, and the Doppler signal was processed by a DISA 55L20 Doppler Signal Processor and recorded on magnetic tape recorder. A complete description of the LDA measurement technique and the approach used in previous experiments at this loop is provided by Creer et al.[4]

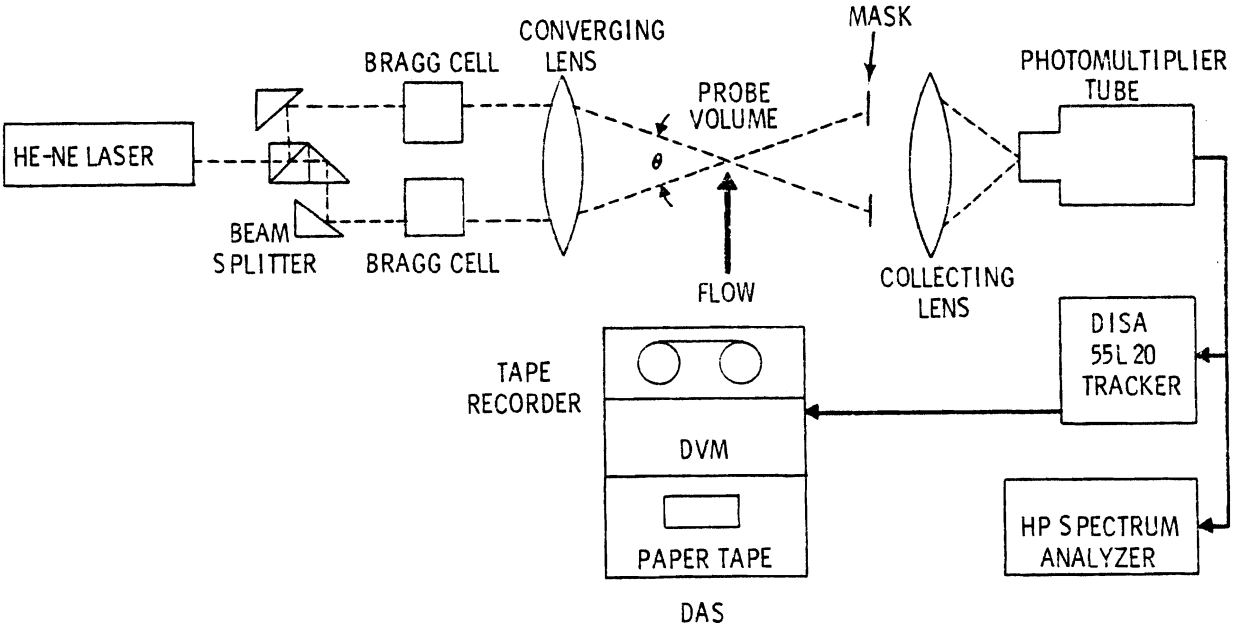

FIGURE 3-6. LDA System

The LDA optics were mounted on a traversing table that allowed positioning of the measurement volume in three dimensions within ±0.001 in. Horizontal positioning was achieved with variable speed servomotors, and a hydraulic lift system was used to position the table vertically.

3.2.2 Temperature Measurements

Temperature measurements were made with iron-constantan thermocouples. A rake of seven thermocouples, shown in Figure 3-7, was mounted on an aluminum plate. Measurements were made by replacing one of the nine flow housing windows with the thermocouple rake. During a data run the rake was installed in the second window above the elevation at which LDA velocity measurements were being made. Velocity measurements with and without the rake showed that it did not influence the velocity data for this spacing. The seven thermocouples located along y = 0.0 (see Figure 3-3) measured the temperature at the centers of Subchannels 8 to 14. Two additional thermocouples monitored the test section inlet and exit temperatures. Commercial reference junctions were used.

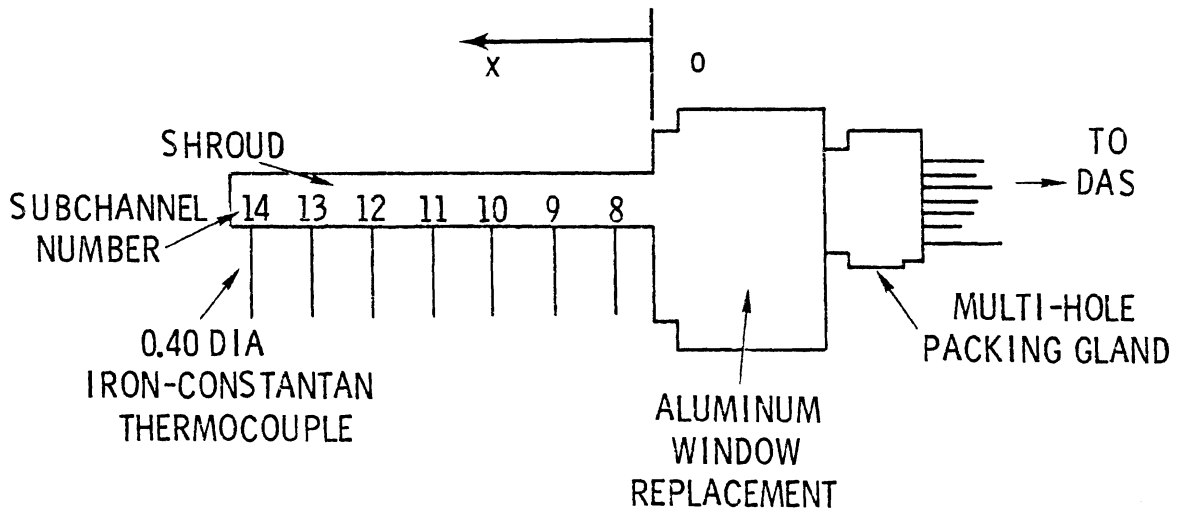

FIGURE 3-7. Thermocouple Rake

3.2.3 Electrical Power

Power generation within the heater rods was determined by voltage and current measurements for each of the 12 rods. Voltage measurements within ±0.01 volts were made with a Fluke Model 803D ac-dc voltmeter. The heater rod current was monitored with a Weston Industrial Analyzer to ±0.25 amperes.

The power gradient was established in the x direction by combining the heater rods in parallel and series arrangements with the two variacs. Rods 1 through 6, the high power set, were connected to one variac and Rods 7 through 12, the low power set, were connected to the other. Figure 3-8 shows the heater arrangement for a variac to produce the two-step gradient. In this combination, the power supply ran balanced and each phase contained two heater elements in parallel. The maximum voltage possible for this arrangement was approximately 260 volts/rod, corresponding to a maximum individual rod power of nearly 3.6 kW. Different voltage settings on each variac produced the desired gradient.

3.3 EXPERIMENTAL PROCEDURE

The LDA and data acquisition system were checked out and adjusted in isothermal flow prior to each data run. The optical table was first moved to the desired vertical position and then the laser beams were aligned parallel to the rod rows. If necessary, the optics were adjusted to optimize the signal. The centerline of each subchannel row, $y = 0.0 \pm 0.581$ in., was located by traversing the LDA probe volume in the y direction until the Doppler signal first disappeared. The loss of signal indicated the position of the flow housing wall or the row of heater rods and was repeatable to ±0.002 in., approximately 2 percent of the rod gap.

The traverse limits in the x direction (the windows) were determined by traversing the probe volume in the x direction until the frequency tracker displayed zero velocity (the 51.1 kHz Bragg cell frequency). However, determining the window position was not as reliable as finding the heater rods because the surface condition (cleanliness) of the windows

strongly affected the DISA tracker performance. Locating the x-traverse limits was repeatable to approximately ±0.020 in.

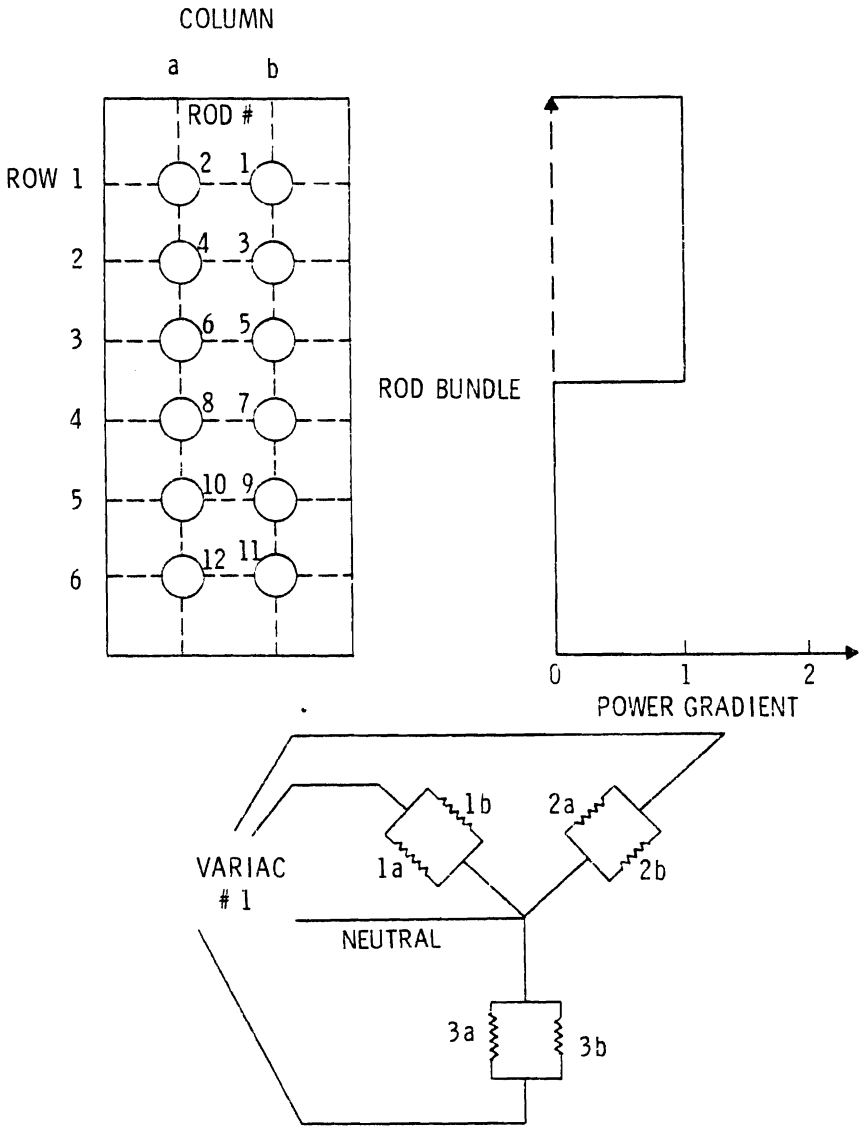

FIGURE 3-8. Heater Arrangement for a Two-Step Gradient

When the optical system was positioned, the inlet flow and heater rod power were adjusted to the desired levels and after the steady state condition was reached data acquisition began. All velocity, x-position, and temperature measurements were recorded simultaneously on seven-track magnetic tape and on paper tape. Heater rod voltage and current were

recorded manually several times for each data run and averaged to provide the power readings presented in Appendix B. Data reduction was handled by a computer program.

4.0 OPERATING CONDITIONS

The operating conditions for this experiment were largely dictated by the ability to make meaningful LDA measurements under the influence of complex and interacting thermal gradients (plumes) in the flow. Measurements reported here were made only when the effect of thermal plumes was minimal. However, because this study represents one of the first applications of the LDA velocity measurement technique to flows of this type it seems valuable to report circumstances which made measurement impossible. The following section discusses some of the observations made during preliminary experiments.

4.1 LDA MEASUREMENT CAPABILITY

The index of refraction for water varies only about 0.5 percent from 75 to 160°F, the approximate temperature difference between the rod surface and the center of a subchannel at the bundle midpoint. For an optical measurement, however, this change of index is extremely large. A typical laser interferometer, for example, may be capable of sensing changes of refractive index on the order of 0.0001 to 0.001 percent. Moreover, in this experiment the change varied in time and was nonuniform throughout the heated region. The LDA laser beams always passed through this zone of interference so the influence of the thermal plumes was sufficient to be the criterion for making successful velocity measurements.

One effect of these density gradients on the laser beams was a steady deflection of the probe volume away from its normal cold position. For this study, the higher values of heat flux in the range $GR > 7.5 \times 10^4$ caused the laser beams to deflect as much as 50 percent of the 0.100-in. rod separation. The static beam deflection was apparently caused by either small irregularities in rod alignment, $\pm$0.004 in. about the mean centerline of the rod row, or variations in the individual rod powers of approximately 1 percent. Laser beam deflection occurred on a small scale at the interface between relatively cold water and the thermal plume rising from the rod. Static displacement of several plumes relative to each other on a larger

scale caused a cumulative shift in the laser beam path. Likewise, each of the two laser beams was affected differently because each entered the same thermal plume at different angles.

In addition to the static deflection, the probe volume was observed to dynamically occupy a spherical space as large as 0.080 in. in diameter. This effect was caused by the time-varying plume position. The primary effect of the spatial wandering was to provide an average flow velocity for the effective volume occupied. Because the severity of the static and dynamic beam deflection was proportional to the heat input to the water, meaningful velocity measurements were not possible at heat flux values much higher than those used in this study. Table 4-1 shows the seven test conditions originally planned for this study, two of which had to be aborted due to difficulties in making meaningful velocity measurements.

It is important to note in the data cases reported the static laser beam deflection was negligible and the dynamic beam movement covered a sphere no more than 0.020-inch in diameter, approximately twice the size of the probe volume in the isothermal flow case.

4.2 EXPERIMENTAL CONDITIONS

For the cases studied, velocity measurements were made along $y = 0.0$, $y = +0.581$, and $y = -0.581$-in. traverses, the centerlines of the three subchannel rows, and any off-centerline measurements that were possible. In most cases velocities were measured every 0.100 in. in the x direction and a few were taken every 0.050 in. If the Doppler signal changed significantly between readings several values were recorded to establish a range.

Table 4-1 shows the three different successful heated cases as well as two cold cases at corresponding flow rates. Also included are two attempts to obtain information at higher GR* that were aborted due to poor signal quality and/or excessive probe volume movement. Case 1 and Case 3 consist of at least one centerline traverse in each of the three

TABLE 4-1. Average Run Conditions

Case Number	Power Gradient	Re[(a)]	GR*[(a)]	GR*/Re^2	ΔT_B (°F)	$\bar{T}$ (°F)	$\dot{W}$ gpm	Q_H (kW/rod)	Q_L (kW/rod)
1	2:1	960	1.23×10^4	0.013	30	75	2.47	1.140	0.570
2	1:0	480	4.05×10^4	0.176	33	75	1.25	0.910	0.0
3	1:0	960	3.80×10^4	0.041	31	75	2.47	1.810	0.0
3a[(b)]	1:0	1200	14.96×10^4	0.104	65	90	2.47	3.590	0.0
4 [(b)]	1:0	1460	7.67×10^4	0.036	46	82	3.40	3.740	0.0
Isothermal 1	0:0	840	0.0	0.0	0	60	2.47	0.0	0.0
Isothermal 2	0:0	420	0.0	0.0	0	60	1.25	0.0	0.0

(a) Based on bundle average D_H = 0.0294 ft and average flow conditions

(b) Unsuccessful

subchannel rows for Windows 1, 3, 5, 7, and 9. Case 2 was terminated after Window 7 due to deterioration in signal quality. The run matrix, Table 4-2, shows the actual run conditions at each window including the average heater rod powers. The power skew placed the higher powered rods in the region $x < 1.8$ inches. The table also labels the locations of any other traverses. Individual current and voltage measurements for each rod are shown in Appendix B, Tables B-7, B-8, and B-9 for Cases 1, 2, and 3.

TABLE 4-2. Experimental Run Matrix

Case No.	Power Skew	$\dot{W}$ (gpm)	UB (ft/sec)	Window Number	y location (in.) 0.0	+0.581	-0.581	Other Traverse	Average Rod Power (kW/rod)	T_{in} (°F)	ΔT_B (°F)
1	2:1	2.47	0.327	1	X	X	X	y = +0.030	1.133/.568	56.2	31.8
				3	X	X	X		1.154/.568	61.7	33.9
				5	X	X	X	y = -0.030	1.145/.564	59.1	28.0
				7	X	X	X		1.154/.573	60.1	28.5
				9	X	X	X		1.134/.567	61.2	29.0
2	1:0	1.25	0.164	1	X	X	X		0.904	60.6	32.5
				3	X	X	X		0.906	59.3	33.1
				5	X	X	X		0.906	59.5	33.1
				7	X				0.912	62.6	33.5
				9							
3	1:0	2.47	0.327	1	X	X	X		1.807	61.1	32.2
				3	X	X	X	y = +0.020	1.816	61.9	35.6
				5	X	X	X	y = +0.030	1.815	61.2	30.6
				7	X	X	X	y = +0.040	1.825	59.7	29.0
				9	X	X			1.819	60.2	28.8
Isothermal 1		2.47	0.327	1	X	X	X		0.0	61.6	0.0
				3	X	X	X		↓	62.0	↓
				5							
				7	X	X	X			60.8	
				9	X	X	X			60.1	
Isothermal 2		1.25	0.164	1	X	X	X			59.8	
				3							
				5	X	X	X			59.2	
				7							
				9					0.0		0.0

5.0 DATA ACCURACY

An error anlysis using the error and uncertainty methods of Schenck[5] was performed to estimate data accuracy. The methods and analysis are presented and described in detail in Appendix C. Table 5-1 is a summary of the results of the uncertainty analysis that was based on the nominal flow values of the three heated cases.

Axial velocity measurements were found to have a theoretical uncertainty ranging from ±1.3 to ±0.8 percent corresponding to velocities between 0.065 and 0.650 ft/sec, respectively. These values do not reflect the additional uncertainty sometimes caused by high local velocity fluctuations that affected the frequency tracker lock on the Doppler signal. The magnitude of the fluctuation was determined by taking several velocity realizations at the x location of interest. Only a small percentage of the velocity data presented in this study is affected by uncertainty due to locally high signal fluctuation. Those points affected are generally within ±3 percent of the mean value.

Using the technique described in the experimental procedure, y = 0.0 was repeatedly located to within ±0.002 in. All subsequent y locations were specified relative to this origin with accuracy of ±0.001 in. The position of the window, x = 0.0, was located to within ±0.020 in. and all other x positions relative to the window were know within ±0.001 in. The axial data planes for the LDA traverses were positioned within ±0.100 in. relative to the beginning of the heated length.

The accuracy of the average heater rod power measurement was principally a function of the uncertainty of measuring the current. The rod voltage was determined within ±0.01 V, or less than ±0.01 percent. Power is the product of voltage and current, P = VI, so the rod power accuracy was approximately the current accuracy, ±4.0 percent. These values are presented in Table 5-1 for the average rod power in each test condition.

Measurement of the subchannel temperatures was a function of the thermocouple position relative to the thermal plumes surrounding the heater rods and the calibration accuracy of the thermocouple. Thermocouple

TABLE 5-1. Uncertainty Values

Parameter	Nominal Value	Uncertainty Value	Uncertainty Percent
Volumetric Flow Rate, $\dot{W}$	2.47 gpm	±0.018 gpm	±0.8
	1.25 gpm	±0.019 gpm	±1.5
Mean Velocity, U (Theoretical)	0.065 ft/sec	±0.0008 ft/sec	±1.3
	0.650 ft/sec	±0.0052 ft/sec	±0.8
Experimental Fluctuation Bounds			±3.0
X Data Point Location, x		±0.001 in.	
Y Data Point Location, y (with respect to y = 0.0)		±0.001 in.	
Axial Data Plane Location, z		±0.100 in.	
Heater Rod Voltage, V		±0.01 V	±0.01
Heater Rod Current, I		±0.25 A	
Case 1 High	7.8 A		±3.2
Case 1 Low	5.5 A		±4.5
Case 2	7.0 A		±3.6
Case 3	10.0 A		±2.5
Heater Rod Power, P = VI			
Case 1 High	1.141 kW	±0.037 kW	±3.2
Case 1 Low	0.571 kW	±0.26 kW	±4.5
Case 2	0.907 kW	±0.033 kW	±3.6
Case 3	1.815 kW	±0.045 kW	±2.5
Temperature, T		±1.0°F	
Nondimensional Temperature $\overline{T} = \frac{T - T_{in}}{T_{out} - T_{in}}$	0.5	±0.053	±10.5
	1.0	±0.067	±6.7
	1.5	±0.085	±5.7

position was important relative to the unmeasured temperature gradient between the heater rod surface and the center of the subchannel approximately 0.169 in. away. Each thermocouple was positioned within ±0.040 in. in the x and y directions in the cold bundle. On several occasions after the fluid began heating, the thermocouple rake was observed to twist about its horizontal axis (x-axis) so that the thermocouples were no longer parallel with the vertical axis of the rod bundle. The thermocouples were therefore at some unknown location within the subchannel. The exact uncertainty in the temperature measurements caused by this problem is unknown as there was no method of measuring thermocouple location during the heated tests. However, a reasonable estimate might be ±15 percent of the given value.

The overall accuracy of each thermocouple and DAS combination was certified to be ±1.0°F by calibration before and after the experimental data run series. For a nominal 30°F temperature difference across the inlet and outlet of the bundle, the uncertainty of the nondimensional temperature

$$\bar{T} = \frac{T - T_{in}}{T_{out} - T_{in}} = \frac{\Delta T}{\Delta T_B}$$

for several values is presented in Table 5-1. The time response of the temperature measurement system tended to time average the small scale fluctuations of the temperature profile surrounding the rods. The temperatures reported represent an average of these fluctuations illustrated by Figure 5-1. This figure is thought to qualitatively demonstrate the amount of thermal plume movement and hence the dynamics of the temperature gradients surrounding the heater rods. The uncertainty caused by these temperature fluctuations, approximately ±1.5°F, is included in nondimensional form on Figures 6-20 to 6-22 as a vertical bar for comparison with the nondimensional profiles.

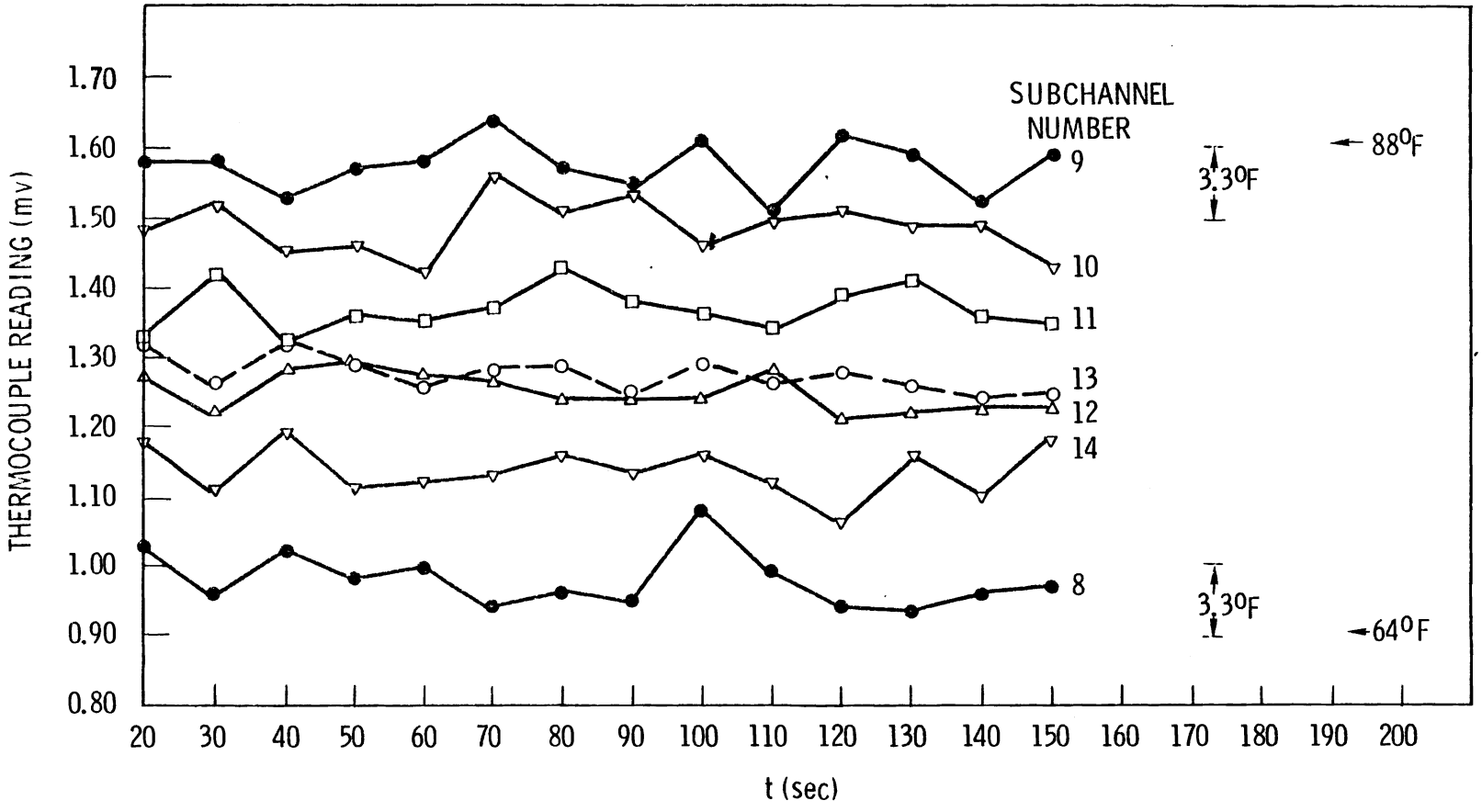

FIGURE 5-1. Time Variation of Thermocouple Rake Output for a Typical Heated Flow Case

6.0 EXPERIMENTAL RESULTS AND DISCUSSION

The experimental results for two isothermal cases and three heated cases with the flow conditions shown in Tables 4-1 and 4-2 are presented in the following sections.

6.1 ISOTHERMAL VELOCITY PROFILES

Prior to the heated bundle data runs, velocity measurements were made in a cold bundle to establish a reference for the heated cases. The results of these isothermal runs are the profiles of the nondimensional axial velocity along the x coordinate, U/UB versus x, shown in Figures 6-1 through 6-6. The data for some of the axial locations are not available. The thermocouple rake was not used during the isothermal tests. In each figure the axial location and y-position for each LDA traverse are shown to the right of the velocity profiles.

The local velocity, U, was nondimensionalized with respect to the bundle average velocity, UB = $\dot{W}/a$, where $\dot{W}$ is the inlet flow rate and a is the total flow area of the bundle. For isothermal flows the velocity maxima occur in the subchannel centers and the minima are in the rod gaps. The ratio of the maximum to minimum average velocity encountered during the traverse, U_{max}/U_{min}, provides a qualitative indication of the relative flow resistance of the subchannel centers compared to the rod gaps. In all cases the ratio of the peak to average velocity decreased from Window 1 to Window 3 because the laminar flow was still developing. The flow housing was designed for turbulent flow studies and its entrance length is inadequate to establish fully developed laminar flow at Window 1 for most inlet conditions.

Figures 6-1 through 6-3 are the isothermal velocity profiles measured for a 2.47-gpm inlet flow. This flow corresponds to the heated cases 1 and 3. The spacing of the velocity peaks in all the profiles is regular and orderly, indicating that the rod spacing in the x direction was reasonably uniform for each rod row. However, the relative maximum and minimum velocities changed with elevation and also with y-position at a given window. Such variation demonstrates that the rod rows were not exactly parallel and/or that the whole rod bundle was skewed or twisted in relation to the flow housing. The apparent effects of geometry on laminar flow are very significant according to these profiles as might be expected. Even so, the changes observed in the velocity profiles appear

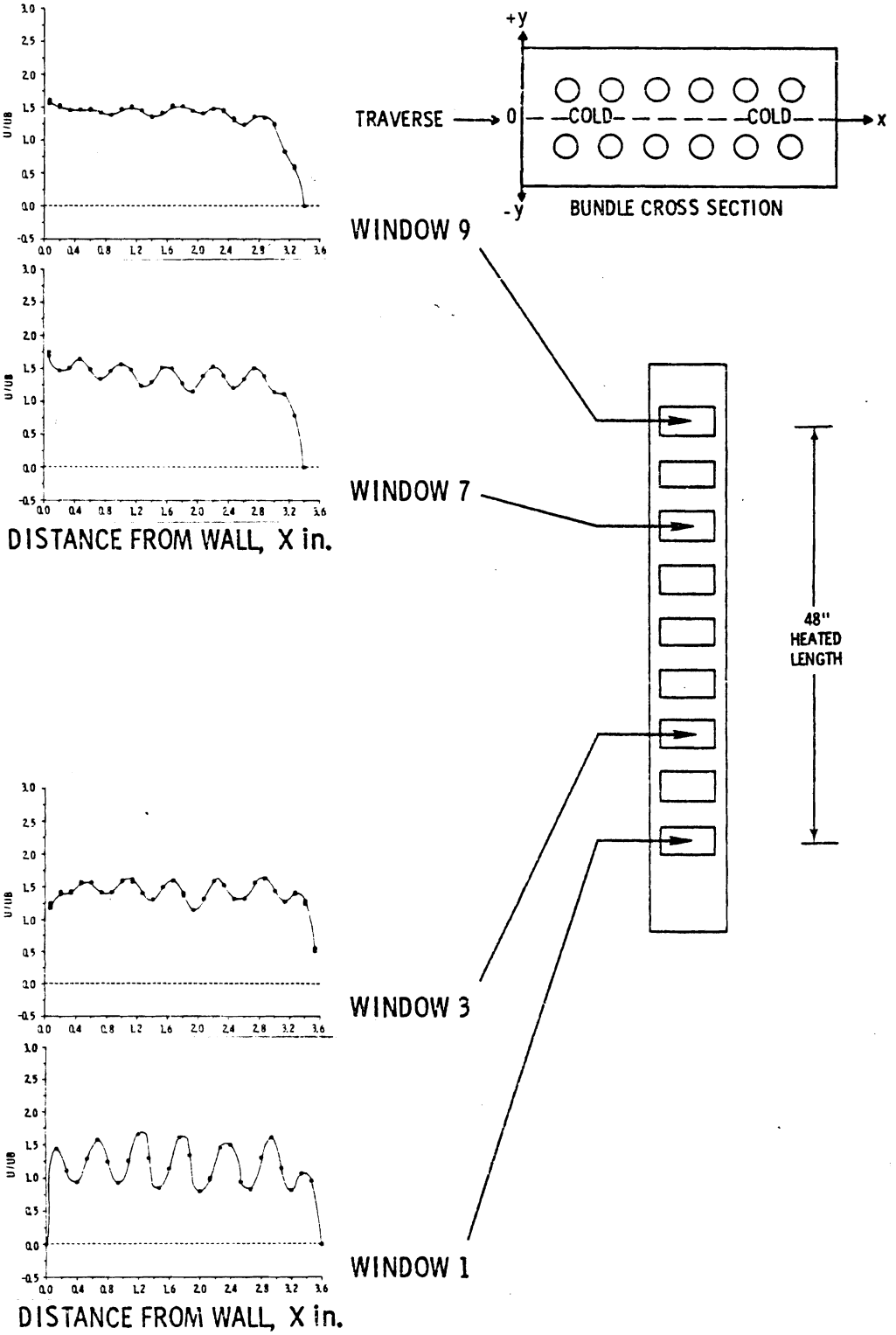

FIGURE 6-1. Isothermal Velocity Profiles, UB = 0.327 ft/sec, y = 0.0 in.

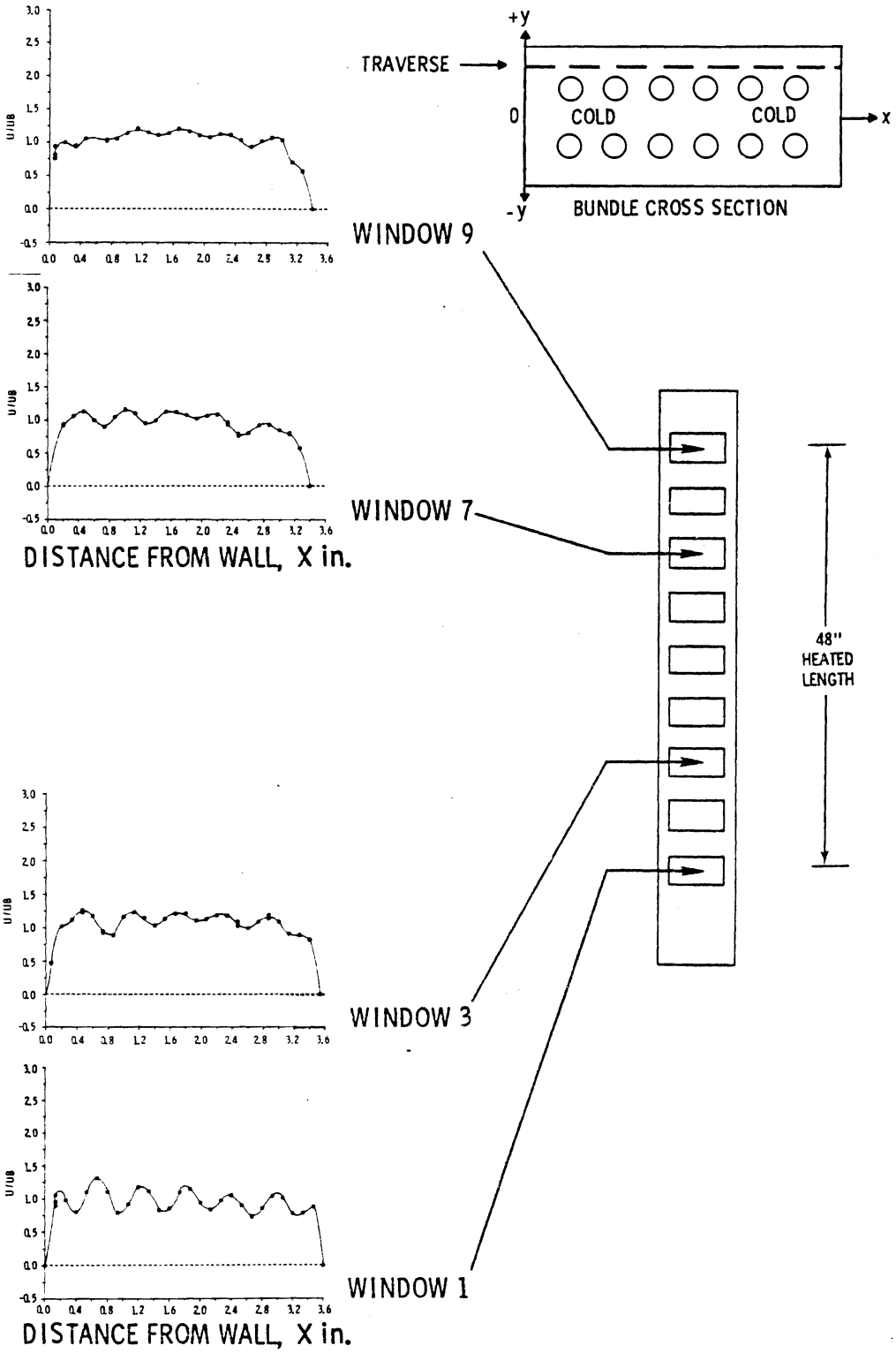

FIGURE 6-2. Isothermal Velocity Profiles, UB = 0.327 ft/sec, y = +0.581 in.

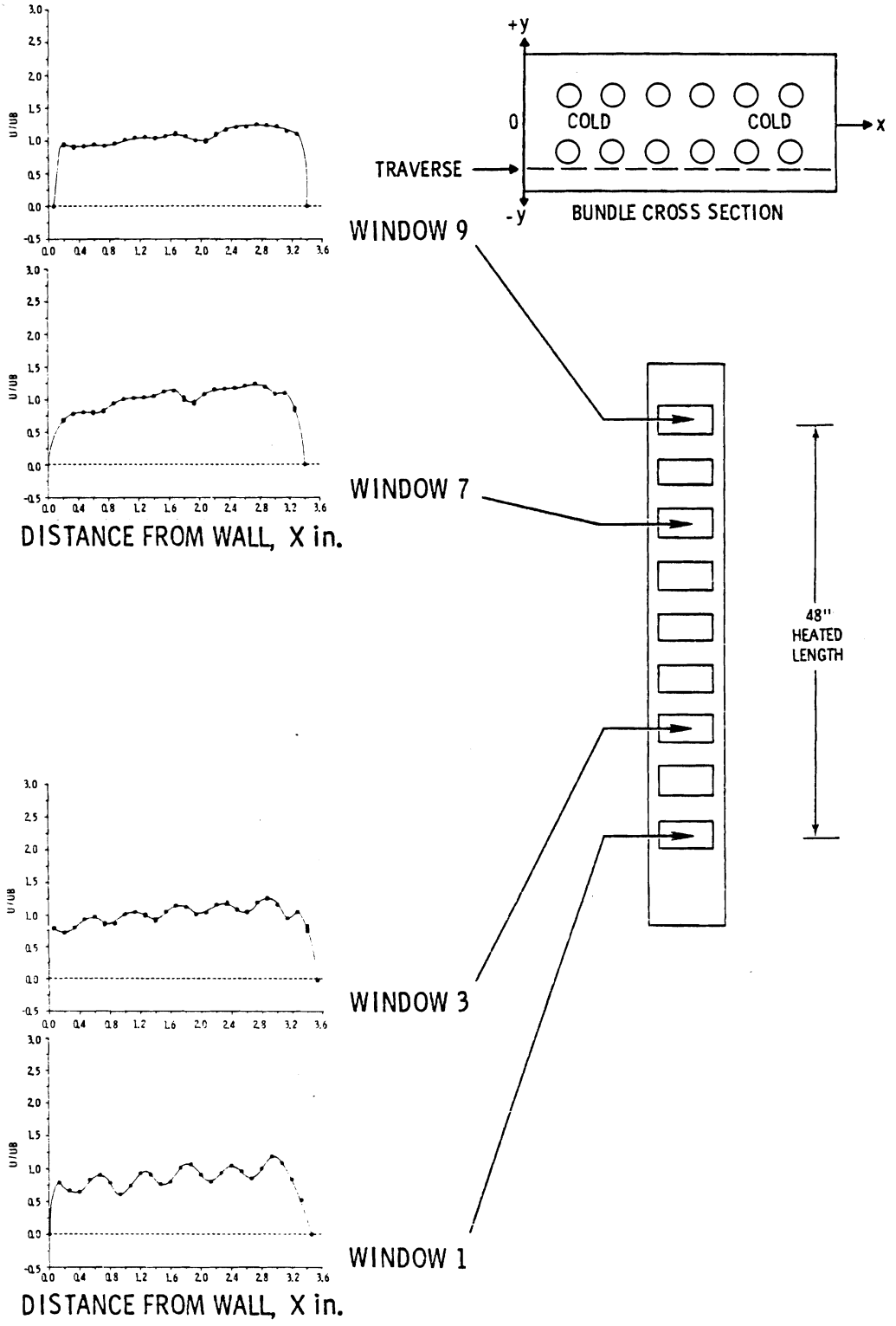

FIGURE 6-3. Isothermal Velocity Profiles, UB = 0.327 ft/sec, y = -0.581 in.

reasonable considering the flow is laminar and the ±0.004-in. variation in rod spacing was about as good as could be obtained without adding a large number of flow-disturbing rod spacers. Because the area of primary interest was the central subchannels where the small bundle asymmetries had little effect on the velocity distribution, the spacing influence was not considered a serious problem.

The other isothermal flow rate investigated was $\dot{W}$ = 1.25 gpm, corresponding to heated Case 2. The results are presented in Figures 6-4 through 6-6. The profiles display the same general trends in peak spacing and velocity magnitude as the higher flow rate but have much larger peak to average velocity ratio. This flow rate dependence is further illustrated by Figure 6-7, the velocity distribution at the bundle midplane (Window 5) for three different flow rates. Figure 6-7a is for a flow rate of 1.25 gpm, Figure 6-7b corresponds to 2.0 gpm, and the last figure is for a flow rate of 3.0 gpm. These flow rates were all within the laminar flow regime and the bundle average Re in each case was 420, 672, and 1008, respectively.

6.2 HEATED VELOCITY PROFILES

The average run conditions for the isothermal and heated cases are described in Table 4-1. Both the Reynolds number and modified Grashof number are based on the bundle average hydraulic diameter and properties evaluated at the mean bundle temperature. The ratio GR^*/Re^2 indicates the relative importance of the buoyant and frictional forces. Note that Case 1 and Case 3 are identical except for the steepness of the power skew so that GR^*/Re^2 for Case 1 is much smaller than for Case 3. Consequently, less significant buoyancy effects create more uniform velocity and temperature profiles for Case 1 compared to Case 3. Likewise, GR^*/Re^2 for Case 2 is relatively large compared to the other cases, and, as will be shown, the buoyancy forces were quite significant.

The run matrix presented in Table 4-2 shows the velocity traverses made, the average rod powers, and inlet and outlet temperatures for each axial location. Note that several traverses were not completed due to adverse thermal effects described earlier. While attempting some velocity

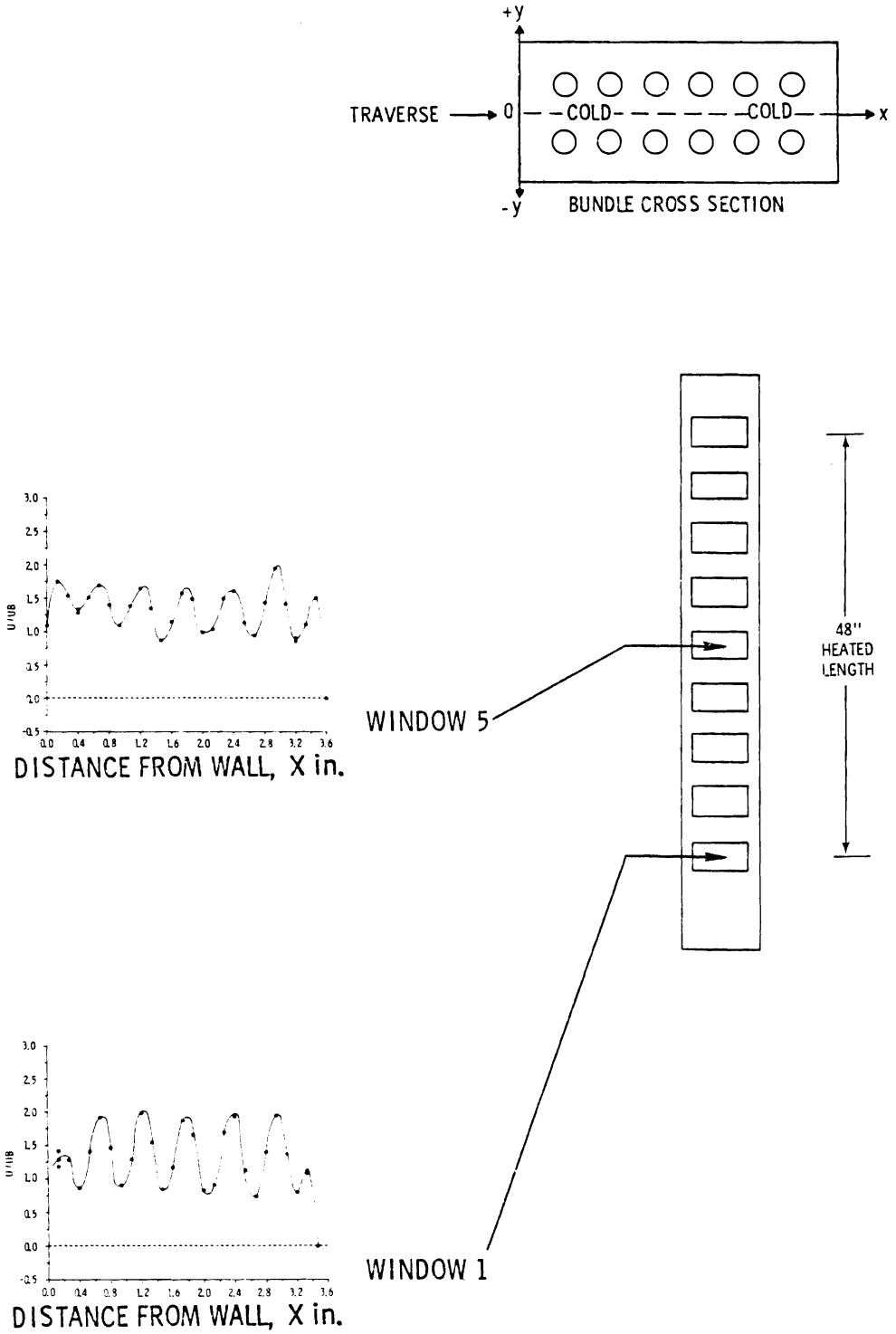

FIGURE 6-4. Isothermal Velocity Profiles, UB = 0.164 ft/sec, y = 0.0 in.

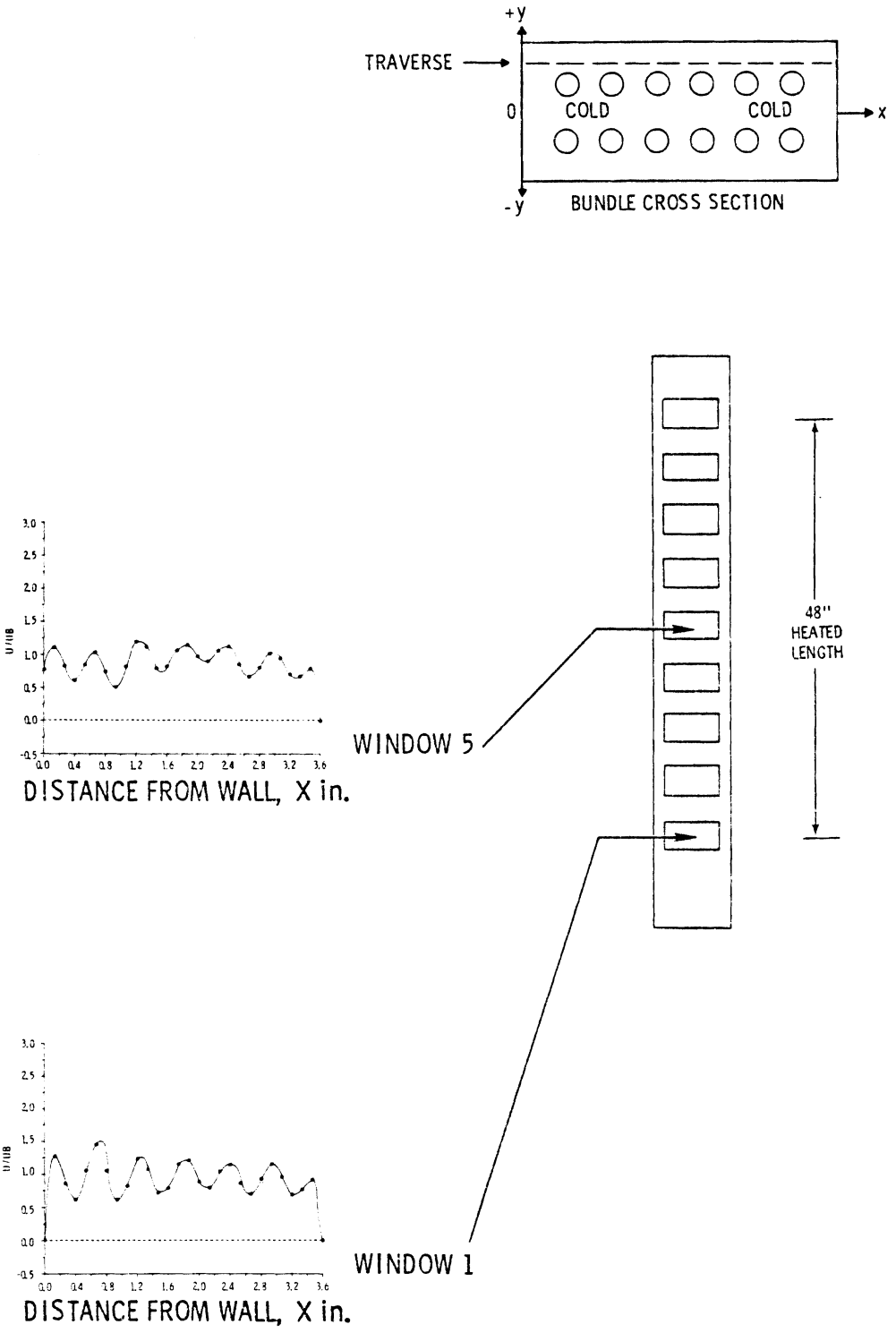

FIGURE 6-5. Isothermal Velocity Profiles, UB = 0.164 ft/sec, y = +0.581 in.

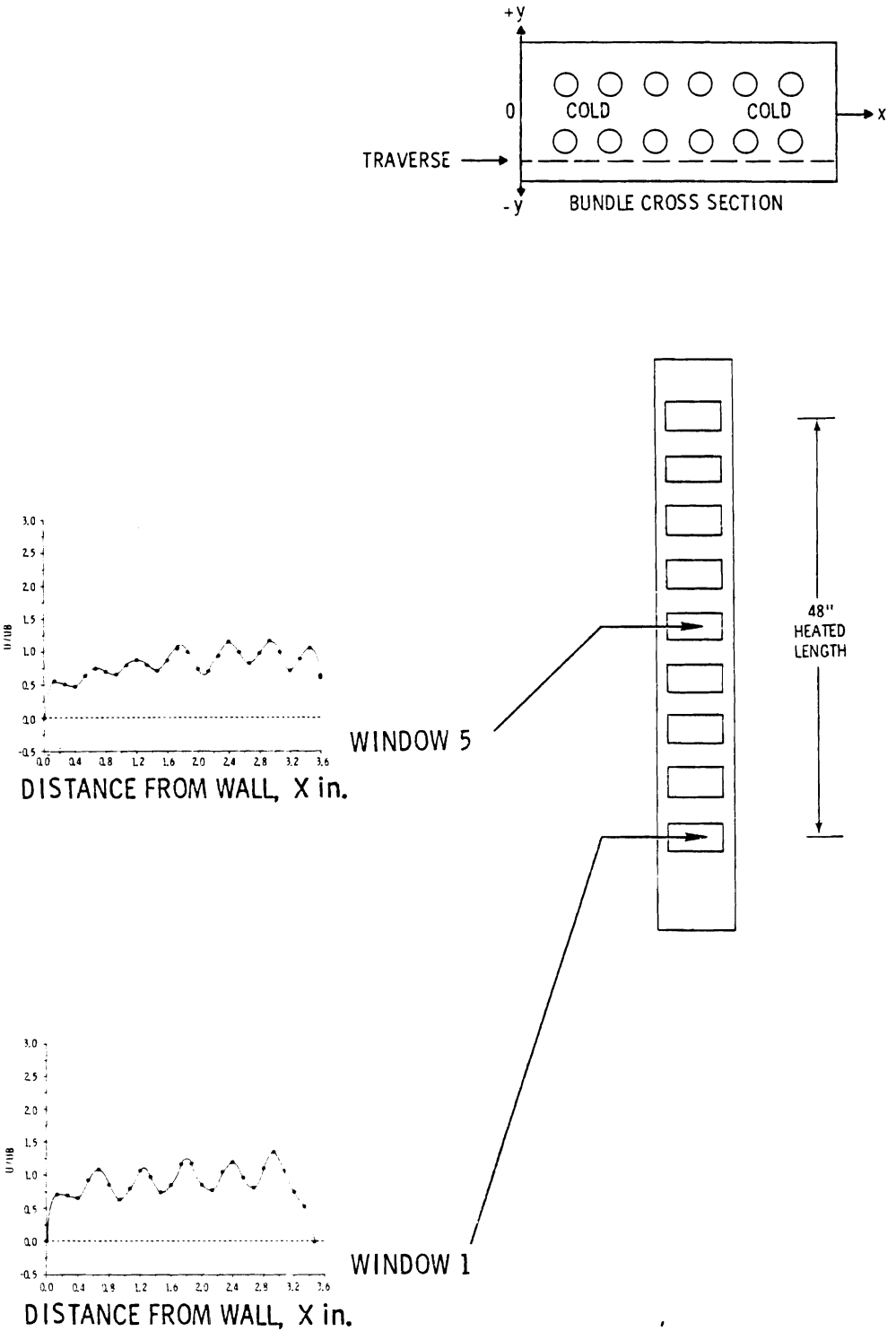

FIGURE 6-6. Isothermal Velocity Profiles, UB = 0.164 ft/sec, y = -0.581 in.

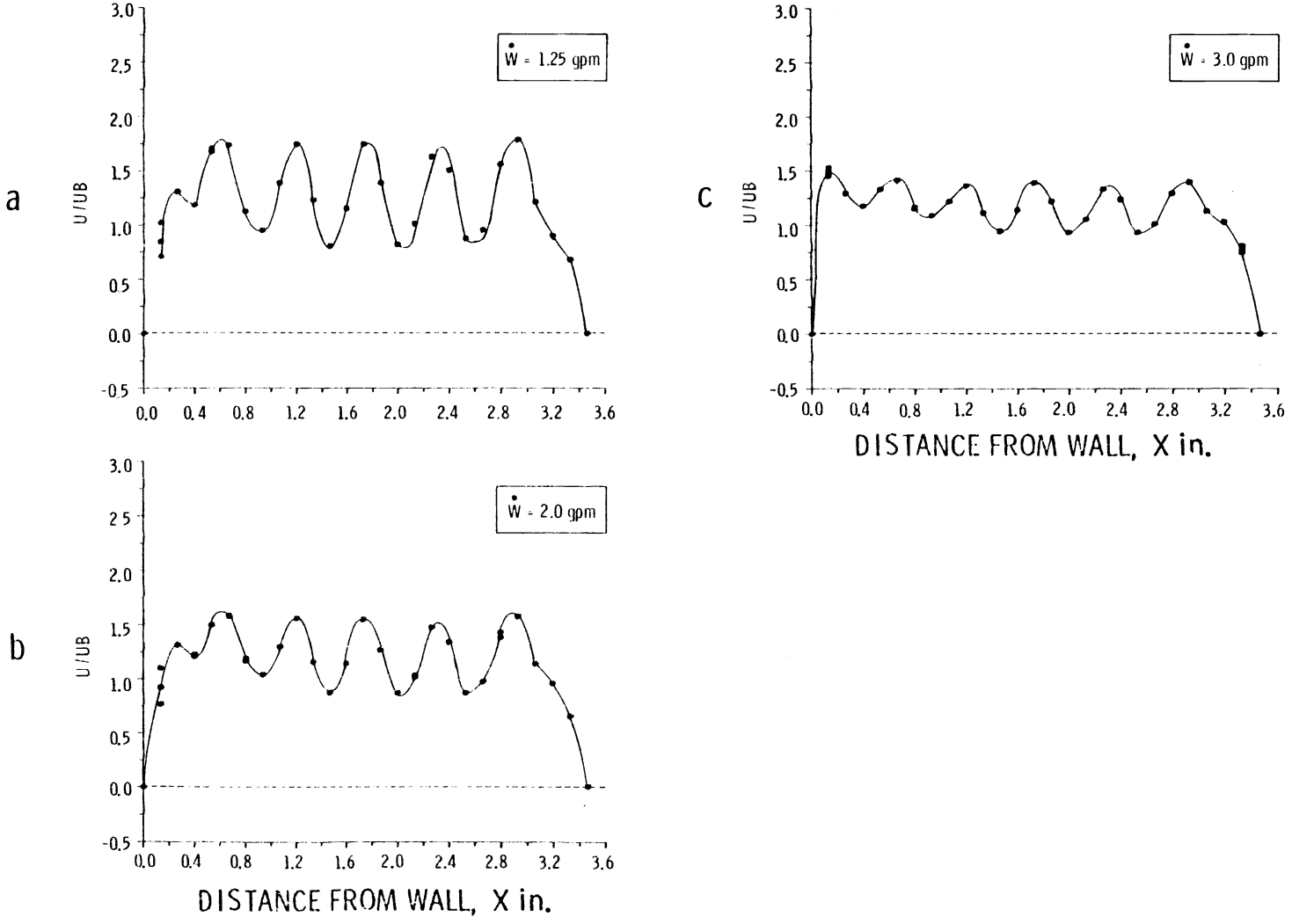

FIGURE 6-7. Isothermal Velocity Profiles, Flow Rate Dependence at Window 5

measurements, the tracker failed to provide a stable reading. In those instances several velocity realizations were taken to mark the bounds of the time fluctuation in the average velocity. This is why some of the velocity profiles exhibit multiple points for a given x-location (for example, see Figure 6-13 or 6-14).

Several velocity traverses were made near the rods at selected elevations. In most cases, the laser beam deflections became more severe as the heater rods were approached. The probe volume movement consistently became radical enough to produce velocity measurements from a spherical volume as large as 0.080 in. in diameter, slightly less than the 0.100-in. rod separation. Resultant velocity profiles were nearly identical to profiles along the subchannel centerlines. The remaining discussion of the heated velocity profiles will be limited to centerline traverses only.

6.2.1 Effects of Heating on the Velocity Distribution

Before presenting results for the three heated cases, a brief discussion is provided to describe qualitatively how heating affects the local velocity. Figure 6-8 is the velocity distribution for the central subchannels of Window 5 superimposed on appropriately scaled heater rods. The experimental conditions for each quadrant of the figure were:

a - Isothermal, $\dot{W}$ = 1.25 gpm

b - Case 1, 2:1 power skew, $\dot{W}$ = 2.47 gpm

c - Case 2, 1:0 power skew, $\dot{W}$ = 1.25 gpm

d - Case 3, 1:0 power skew, $\dot{W}$ = 2.47 gpm

The relative effects of heating at the bundle midplane are evidenced by the redistribution of the uniform inlet flow. From these figures, the flow through the cooler regions was reduced while the flow through the hotter regions increased proportionately. Note that as the parameter GR^*/Re^2 increased from zero (the condition for Figure 6-8a), the distortion in the velocity profile increased. These effects are described in detail in the sections that follow.

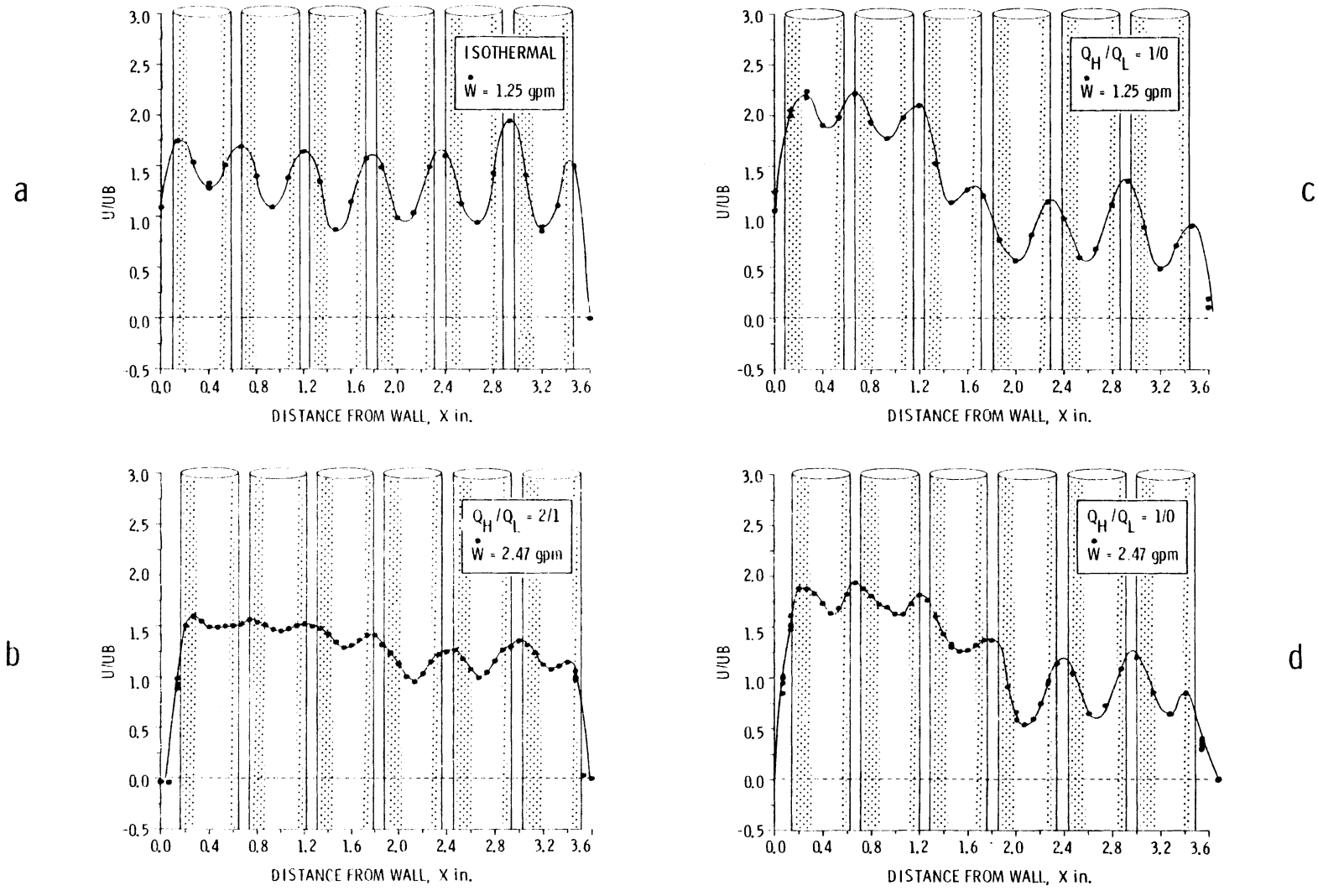

FIGURE 6-8. Effects of Heating on the Velocity Distribution at Window 5

6.2.2 Case 1

Case 1 was a 2:1 power skew with hot and cold rod powers of 1.140 kW/rod and 0.570 kW/rod, respectively. For a flow rate of $\dot{W}$ = 2.47 gpm, these power levels gave a 30°F temperature rise across the bundle. Based on the average flow conditions, Re = 960 and $GR^* = 1.23 \times 10^4$, yielding $GR^*/Re^2 = 0.013$. This value indicates a relatively minor buoyancy importance when compared to Case 2 and Case 3.

Figures 6-9 through 6-12 contain the velocity profiles obtained for Case 1. These profiles may be compared directly to the isothermal profiles of Figures 6-1 through 6-3 to determine the effect of the 2:1 power skew upon the flow. At the beginning of the heated length very little difference from the isothermal case is noted. Data obtained at Window 3 in the hotter side of the bundle, $x < 1.8$ in., indicates that the buoyancy forces have begun to act on the flow field. Individual peaks are less pronounced. Moreover, the average velocity on the hot side is higher than the isothermal case for Windows 3 through 9. In contrast, the average velocity for $x > 1.8$ in. is less than the isothermal case, indicating that flow diverted from the cold regions of the bundle to the hotter regions. The ratio of the average maximum velocity to the average minimum velocity increased for each axial location.

The changes noted in the velocity profiles at Window 3 are more pronounced at each higher axial location, corresponding to a continuous buoyancy-dominated development of the velocity profile. This development of the velocity field is plainly evident in Figure 6-9. The uniformity in the subchannel centerline local velocities increased as the visual extent of the plume interaction increased. (The same is also true of the temperature profiles discussed later.) Figure 6-9 shows that, as the buoyancy forces increased, the velocity profiles became much smoother so that local peaks are no longer evident. This result is similar to the transition from a parabolic laminar velocity profile to a more nearly uniform turbulent velocity profile in isothermal flows.

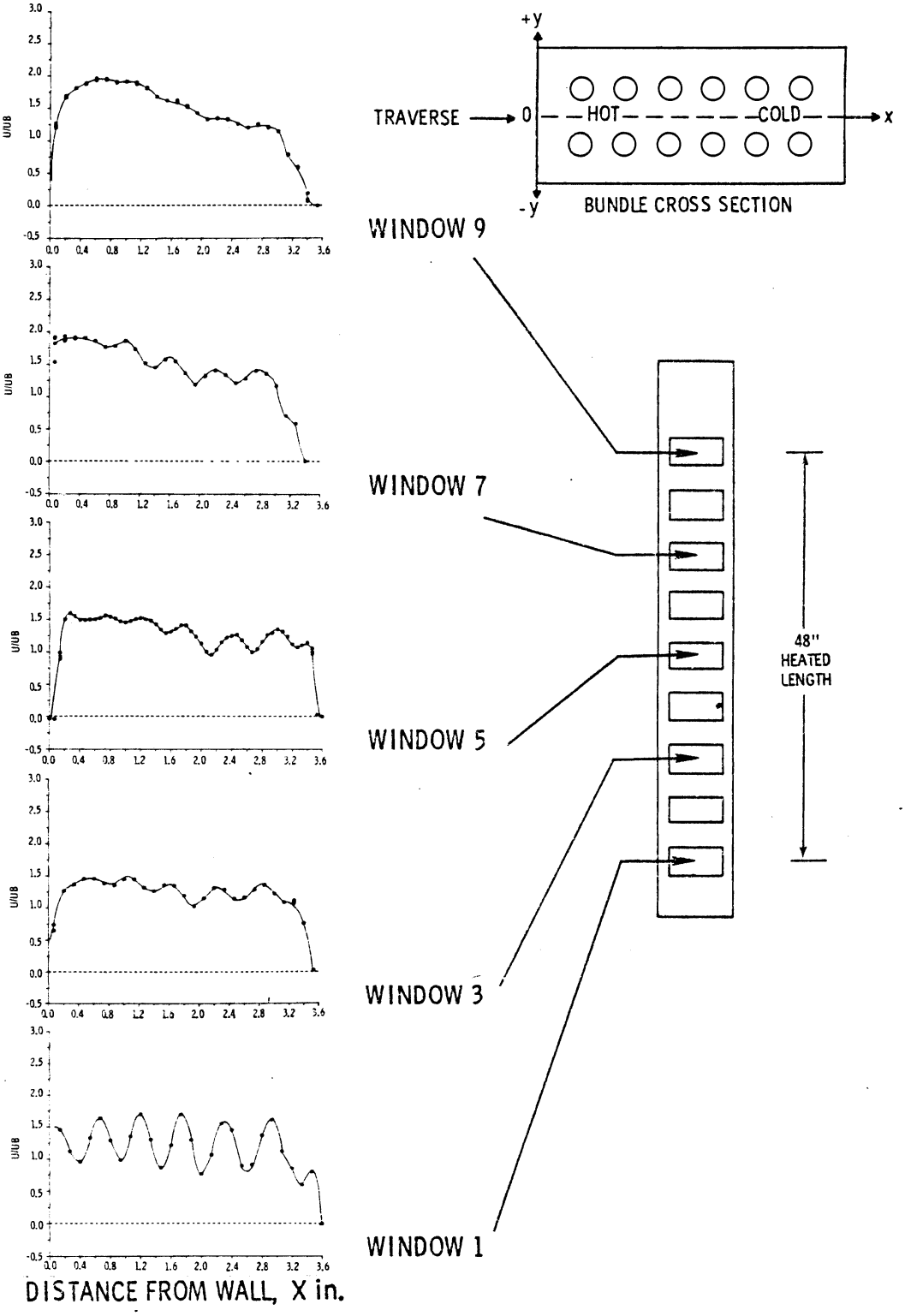

FIGURE 6-9. Case 1 Experimental Velocity Profiles, UB = 0.327 ft/sec, y = 0.0 in., Q_H/Q_L = 2:1

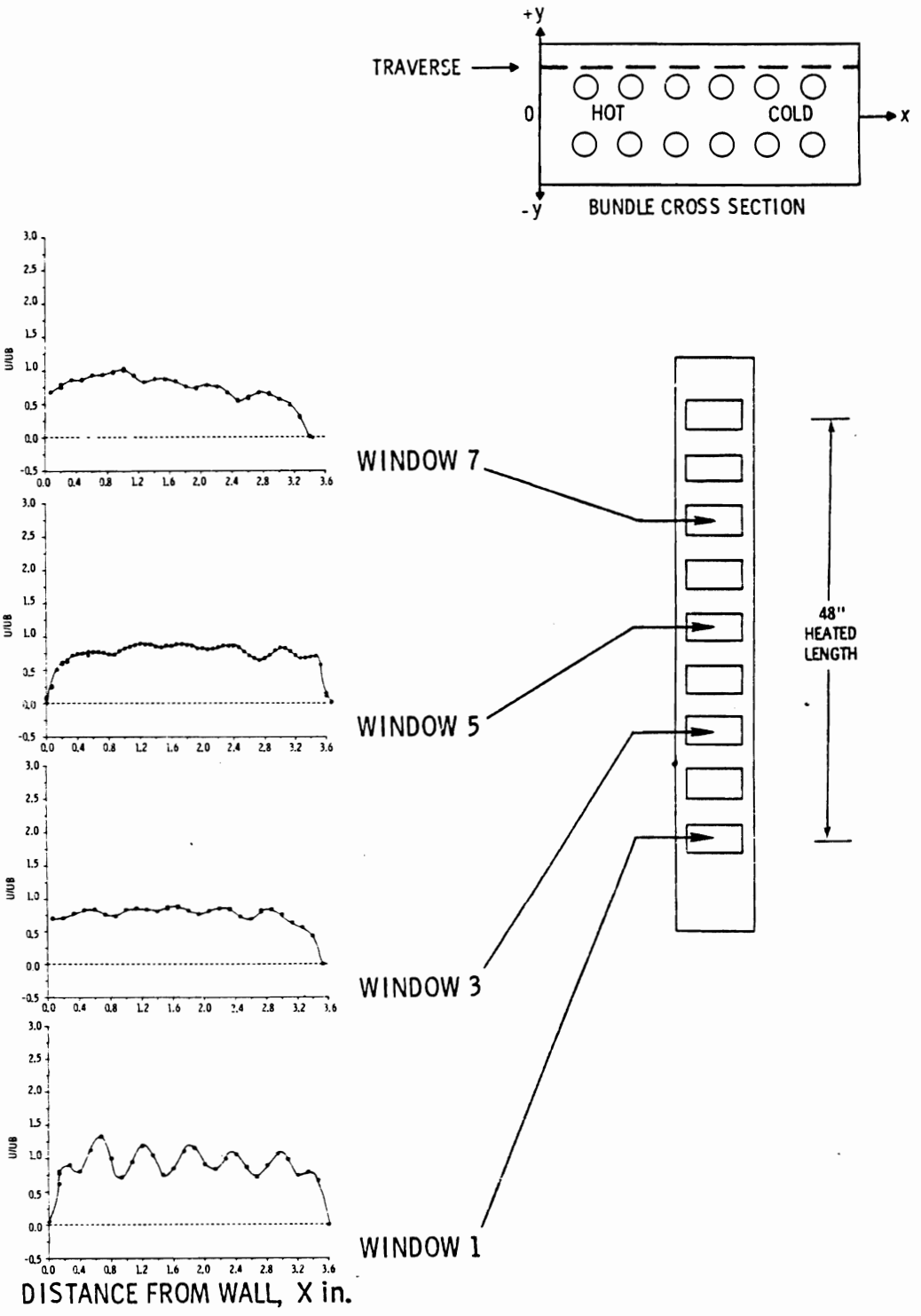

FIGURE 6-10. Case 1 Experimental Velocity Profiles, UB = 0.327 ft/sec, y = +0.581 in., Q_H/Q_L = 2:1

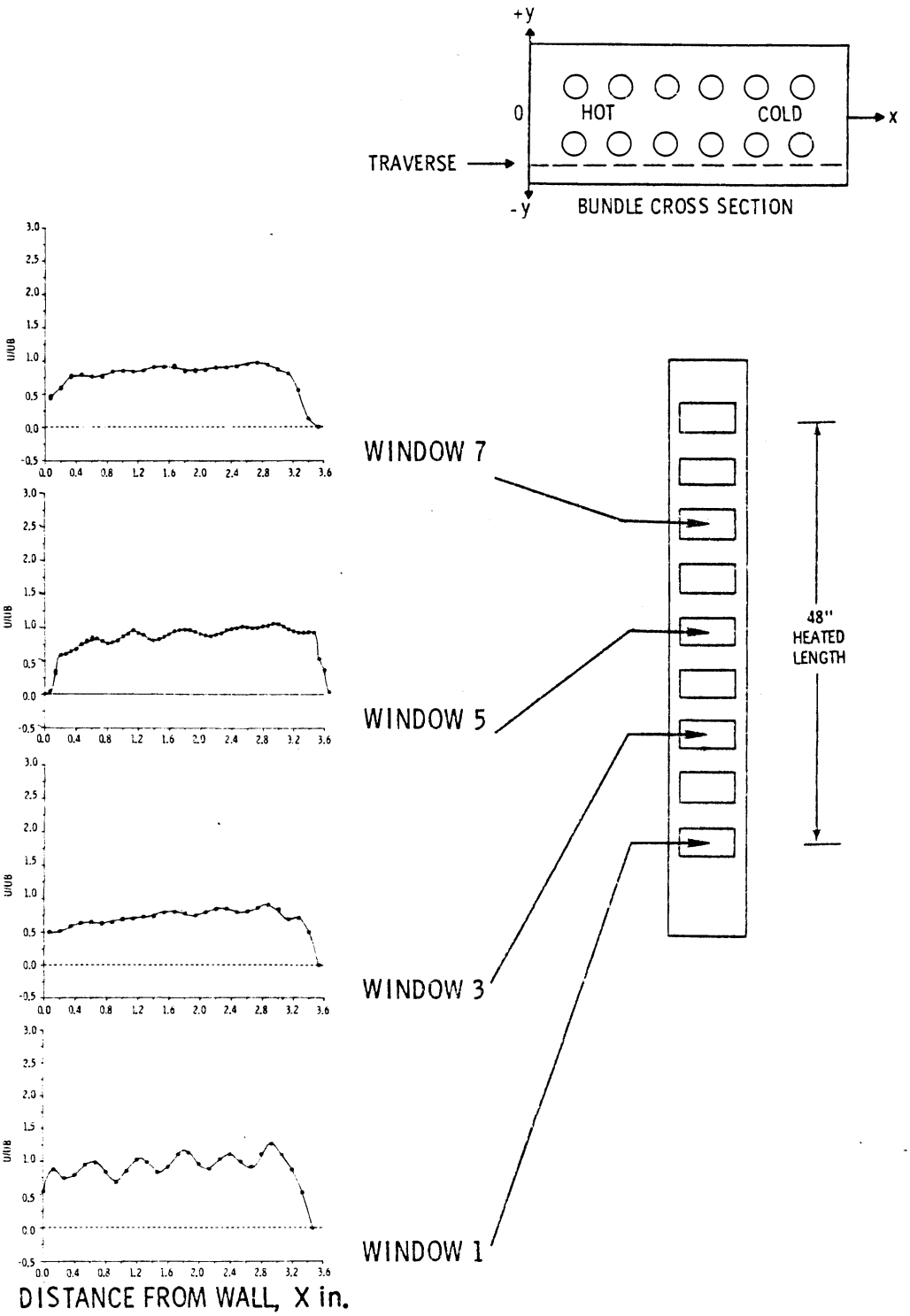

FIGURE 6-11. Case 1 Experimental Velocity Profiles, UB = 0.327 ft/sec, y = -0.581 in., Q_H/Q_L = 2:1

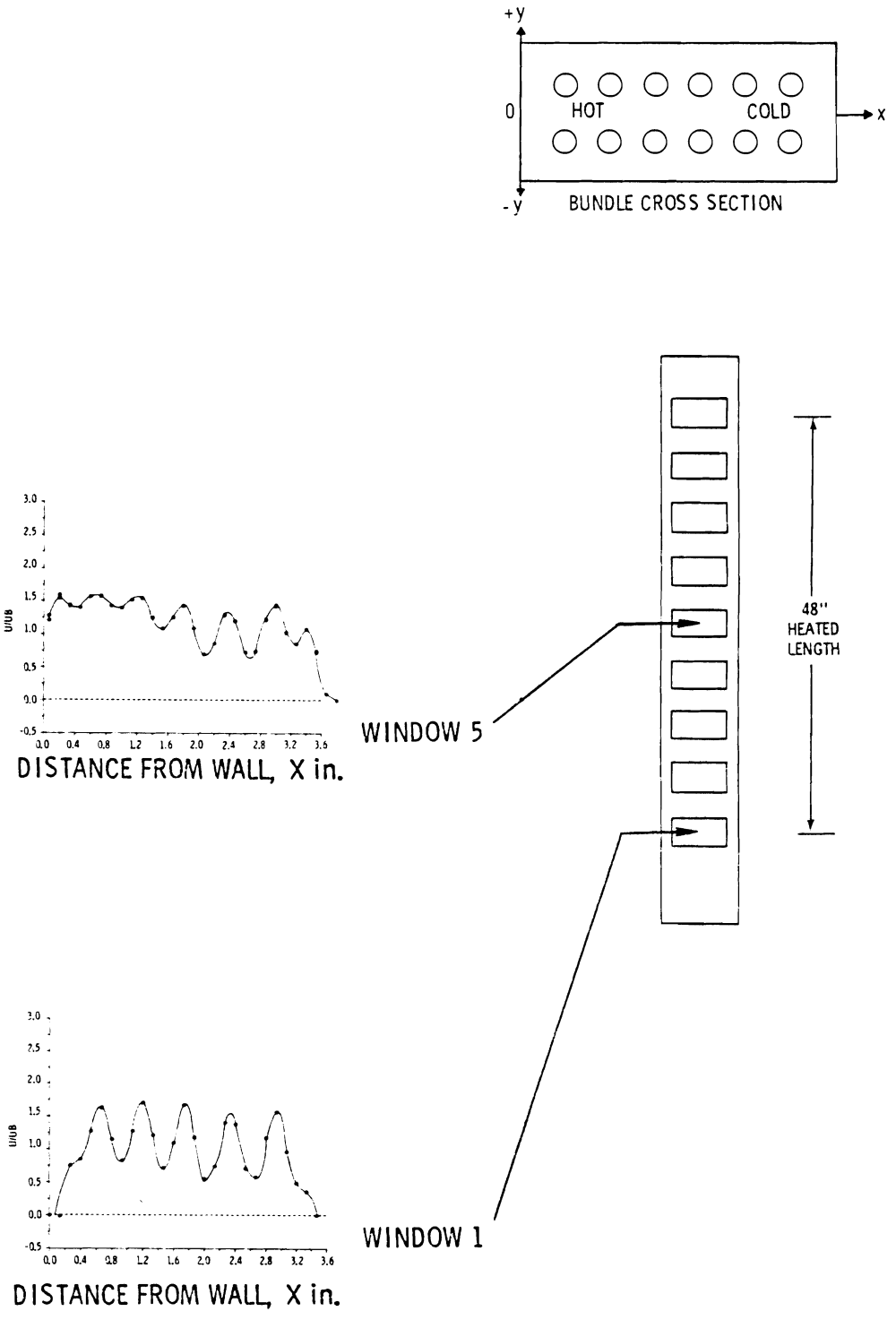

FIGURE 6-12. Case 1 Experimental Velocity Profiles, UB = 0.327 ft/sec, Window 1 y = +0.030 in., Window 5 y = -0.030 in., Q_H/Q_L = 2:1

6.2.3 Case 2

Case 2 was a 1:0 power gradient with 0.910 kW/rod on the hot side and no heating on the other and a flow rate of $\dot{W}$ = 1.25 gpm. This combination yielded approximately the same temperature rise across the bundle as Case 1, ΔT_B = 33°F, but because of the 1:0 power skew and the low flow, the buoyant effects were much more predominant. The value GR^*/Re^2 = 0.176 is indicative of the increased importance of the buoyancy forces over Case 1 (GR^*/Re^2 = 0.013). The two parameters forming this ratio are Re = 480 and $GR^* = 4.05 \times 10^4$.

The velocity profiles shown in Figure 6-13 through 6-15 correspond to the run conditions of Case 2. These profiles reflect the same general trends as the profiles for the first case but with more dramatic evidence of buoyancy-induced flow changes. These buoyancy effects are easily observed in the velocity profiles in Figure 6-13. Pronounced differences in the average velocity between the hot side, $x < 1.8$ in., and the cold side, $x > 1.8$ in., are seen in Figure 6-13 at Window 7. For $x < 1.8$ in. the maximum average nondimensional velocity is greater than 3.0 while the average velocity of the cold portion of the bundle is approximately 0.4. (The central subchannel nondimensional velocities need not average to 1.0 due to the wall channel flows contribution.)

The velocity data at Window 7 seem to indicate that the cold side of the flow was tending toward zero flow although it was not possible to get meaningful velocity measurements at Window 9 due to wide scatter in the velocity realizations. However, distinct observations of both zero flow and negative flow in the region near x = 3.6 in. were made with the LDA and visually on a different occasion at Window 5 under more severe flow conditions. This flow redistribution exhibited by Case 2 is further evidence of the importance of buoyant forces in these flow conditions.

6.2.4 Case 3

Case 3 had the same flow rate, $\dot{W}$ = 2.47 gpm, and total power as Case 1 except the power gradient was 1:0 with 1.810 kW/rod and 0.0 kW/rod versus 2:1 with 1.140 kW/rod and 0.570 kW/rod for Case 1. The bundle temperature

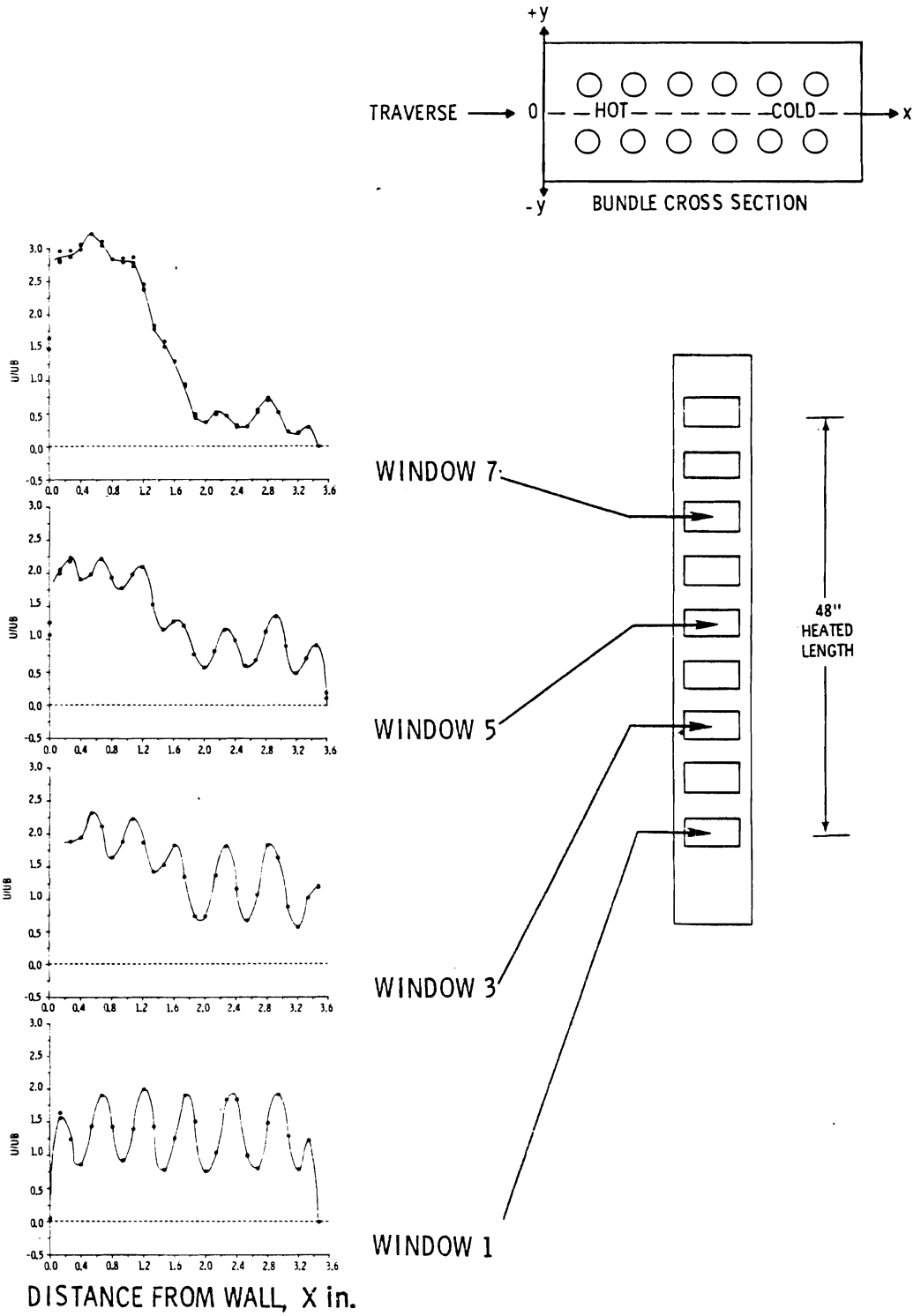

FIGURE 6-13. Case 2 Experimental Velocity Profiles, UB = 0.164 ft/sec, y = 0.0 in., Q_H/Q_L = 1:0

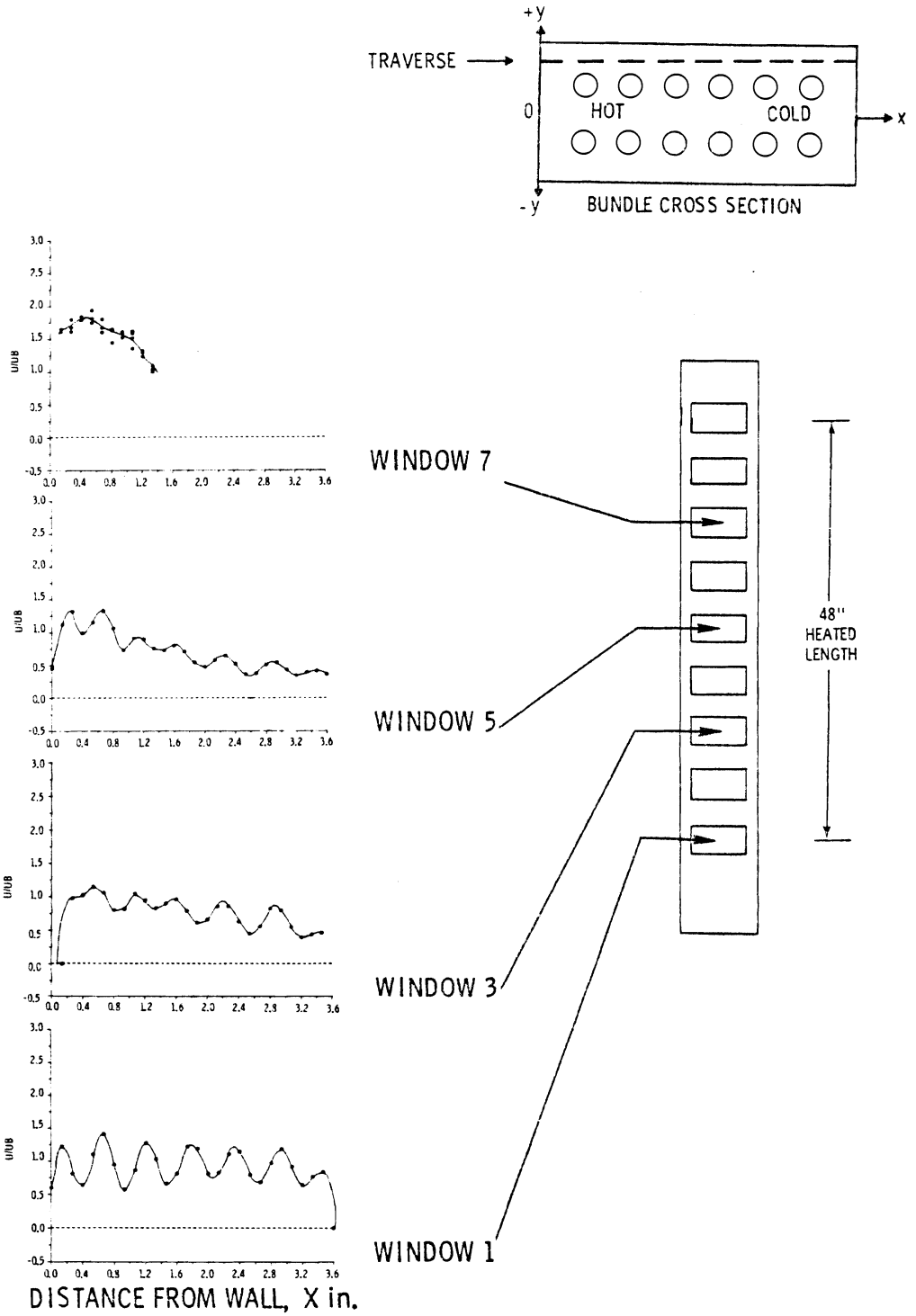

FIGURE 6-14. Case 2 Experimental Velocity Profiles, UB = 0.164 ft/sec, y = +0.581 in., Q_H/Q_L = 1:0

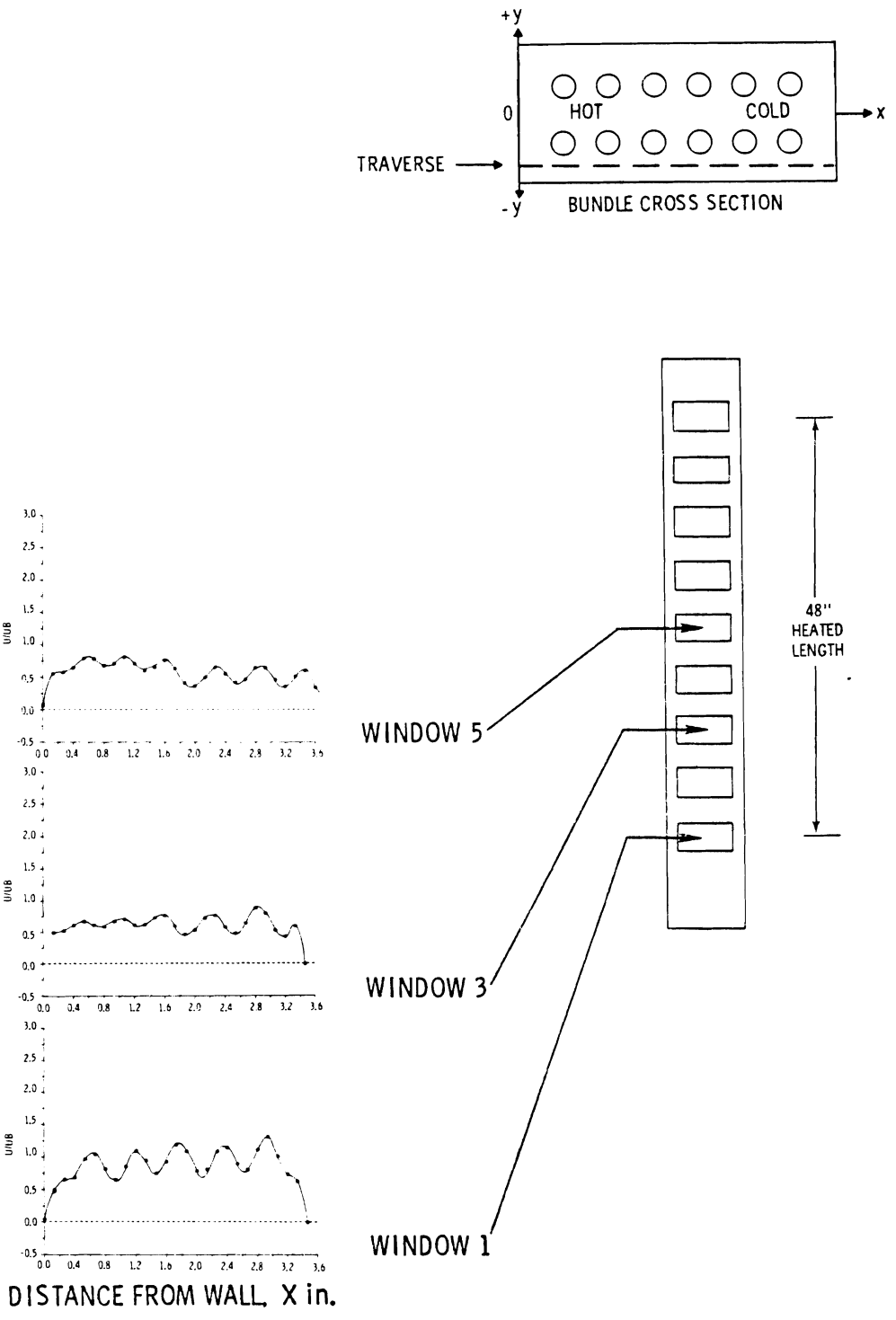

FIGURE 6-15. Case 2 Experimental Velocity Profiles, UB = 0.164 ft/sec, y = -0.581 in., Q_H/Q_L = 1:0

difference was 31°F, but because the power gradient was more severe than the 2:1 skew of the first case, the buoyancy effects were more evident. This is pointed out by the difference in the value of GR^*/Re^2 for the two cases. For Case 3, $GR^*/Re^2 = 0.041$, $GR^* = 3.80 \times 10^4$ and the Reynolds number was 960. Compared to Case 2 the buoyancy effects were not manifested as strongly.

Figures 6-16 through 6-18 contain the results of Case 3. As before, the velocity profiles at Window 1 appear little different than the cold case. Also, the off-centerline LDA traverses are largely indistinguishable from the centerline runs and are not shown except in Figure 6-19. Compare, for example, the three profiles shown in Figure 6-19 to the velocity profile at Window 5 in Figure 6-16. The profiles in Figure 6-19 are off-centerline traverses ranging from 0.020 in. to 0.040 in. from the bundle centerline, $y = 0.0$ in. There are few differences between these profiles and the $y = 0.0$ in. traverse at Window 5, Figure 6-16. At Window 3 the mass flow rates started to become unbalanced with more flow going to the hot side. Figure 6-16 shows that this unbalancing of the flow continued to increase with elevation until the top of the heated length. At Window 9 the flow through the regions $x < 1.8$ in. was approximately 50 percent greater than the isothermal flow. This reiterates the findings of Cases 1 and 2. Buoyancy forces induced by heating caused the flow to become unbalanced and redistributed across the bundle with more fluid flowing up the heated side.

6.3 TEMPERATURE

Temperature was measured by thermocouples in the center of the seven central subchannels and at the inlet and outlet of the test section. A common signal triggered the recording of all pertinent flow and temperature data so that a temperature measurement and a velocity realization were simultaneously recorded on the data acquisition system (DAS). The subchannel temperature measurements were taken at an axial location 12.0 in. (2 windows) above the elevation of the LDA traverse. Previous tests verified that the thermocouple rake did not interfere with the velocity measurement at this separation. In all cases, the temperatures shown are the average of approximately 35 to 40 temperatures recorded over the

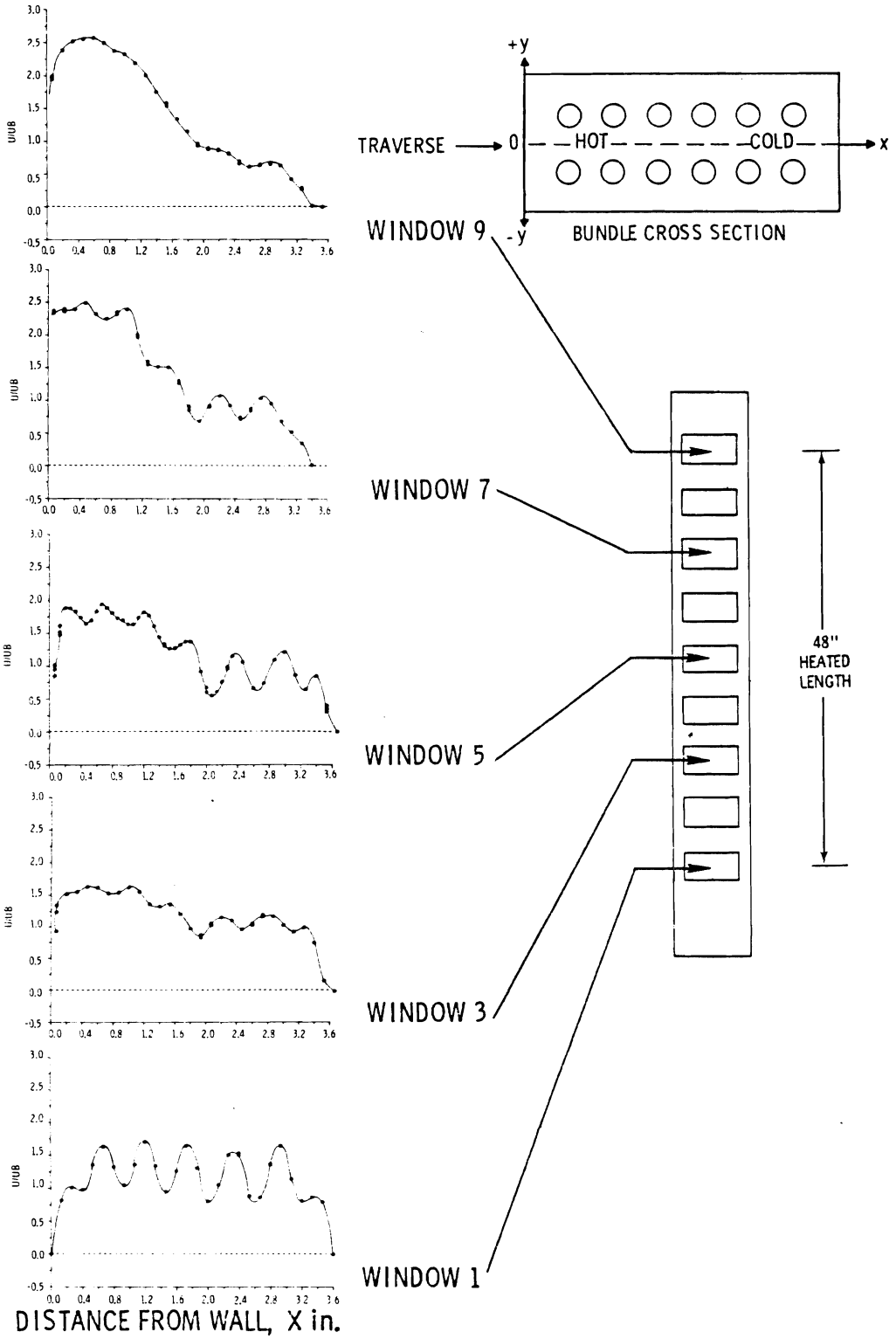

FIGURE 6-16. Case 3 Experimental Velocity Profiles, UB = 0.327 ft/sec, y = 0.0 in., Q_H/Q_L = 1:0

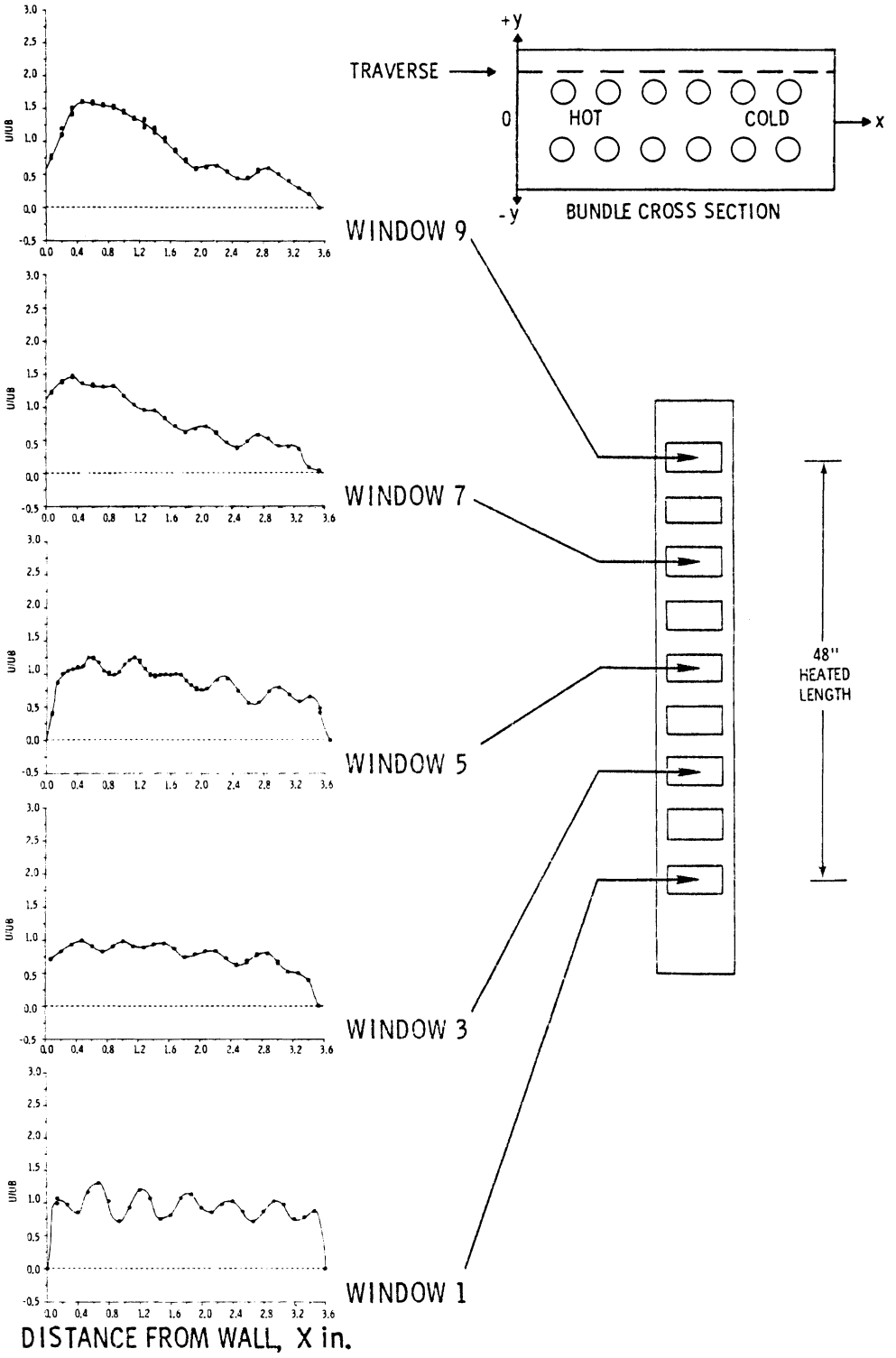

FIGURE 6-17. Case 3 Experimental Velocity Profiles, UB = 0.327 ft/sec, y = +0.581 in., Q_H/Q_L = 1:0

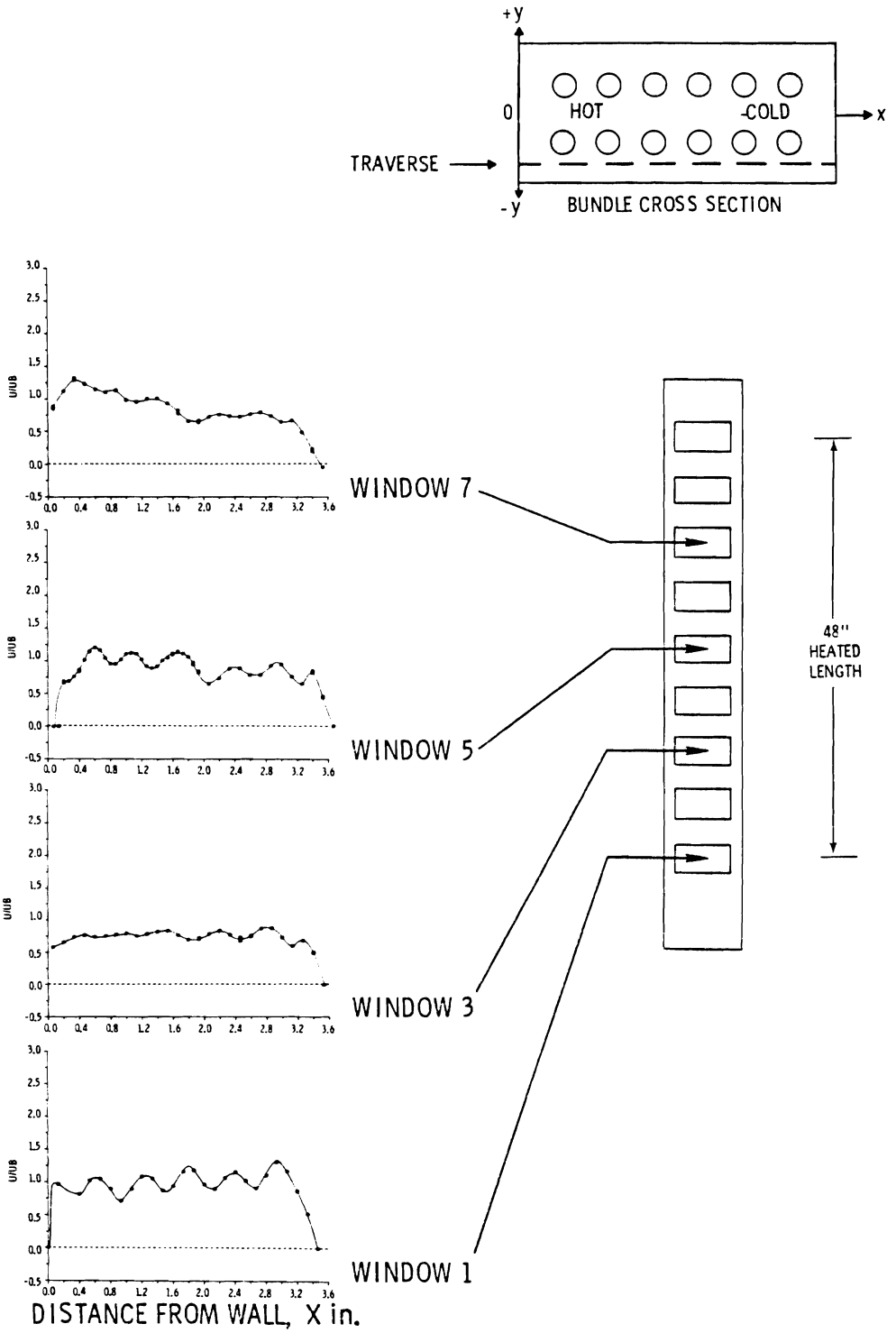

FIGURE 6-18. Case 3 Experimental Velocity Profiles, UB = 0.327 ft/sec, y = -0.581 in., Q_H/Q_L = 1:0

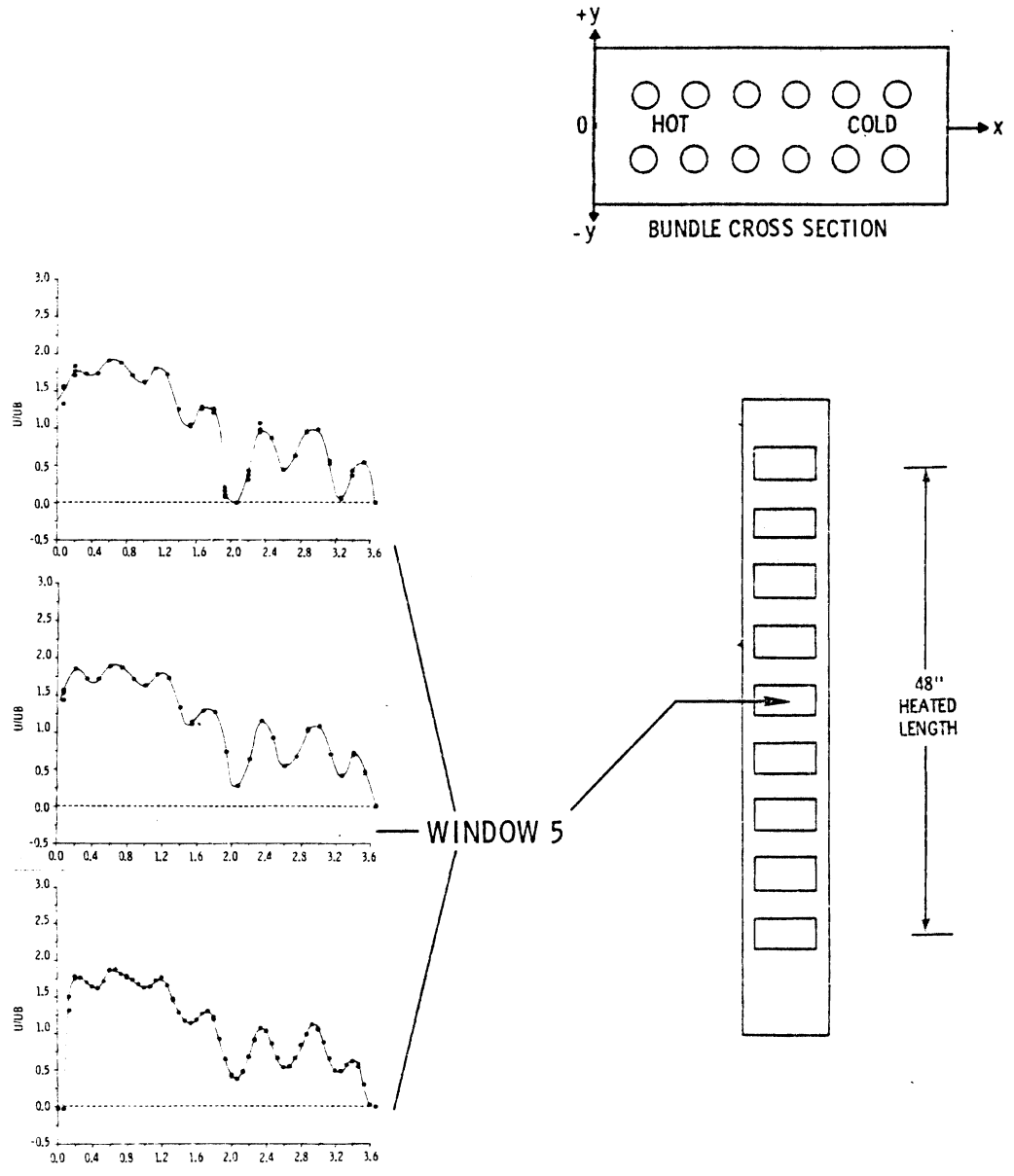

FIGURE 6-19. Case 3 Experimental Velocity Profiles, UB = 0.327 ft/sec, Window 5, y = +0.020 in., y = +0.030 in., y = +0.040 in., Q_H/Q_L = 1:0

approximately 30 to 45 minutes necessary to complete a velocity traverse.

The nondimensional temperature profiles for Cases 1 through 3 are shown in Figures 6-20 through 6-22. The actual temperature of each subchannel is recorded in Tables B-1 through B-3 in Appendix B. The uncertainty due to the time fluctuation of the temperature and thermocouple calibration is shown to the right of each plot as vertical bars. The time fluctuation uncertainty was included on those figures because the time fluctuation of the local temperature shown by Figure 5-1 was not necessarily averaged out by the small number of measurements.

The general behavior in temperature development was as one would expect, increasing in proportion to the local power rate. However, in all three cases, the temperatures measured in Subchannel 8 were unusually low. This subchannel was on the hot side of the bundle but its temperature in Case 1 (Figure 6-20) was lower than Subchannel 14 in the cooler region of the flow. The authors have no explanation for this anomaly because the thermocouple calibration was checked before and after the heated data runs and its proper location on the thermocouple rake was periodically verified.

Figure 6-20, Case 1, shows the ratio of the average hot side temperature to the average cool side temperature decreases with elevation. This effect is not readily apparent for Cases 2 and 3, as the 1:0 power gradient created a much larger temperature differential across the width of the bundle than the 2:1 power skew of Case 1. The value of GR^*/Re^2 for those cases was much larger than for Case 1. However, Figure 6-21, Case 2, shows the temperatures of both Subchannels 13 and 14 at Window 9 were substantially elevated above the inlet temperature in Case 2. This must have been the result of recirculation.

The temperature data presented here helps to explain the flow redistributions observed in the velocity profiles and the link between the parameters GR^*/Re^2 and the effect of the buoyancy forces. As the fluid temperature increased in response to heating, the density decreased, causing the flow to accelerate. This relationship is clearly demonstrated by comparing the velocity and temperature profiles presented above. The ratio of the buoyancy forces caused by the heating to the frictional forces caused by the fluid flowing through the bundle is represented by the parameter GR^*/Re^2. At $GR^*/Re^2 = 0$, profiles of temperature and velocity were

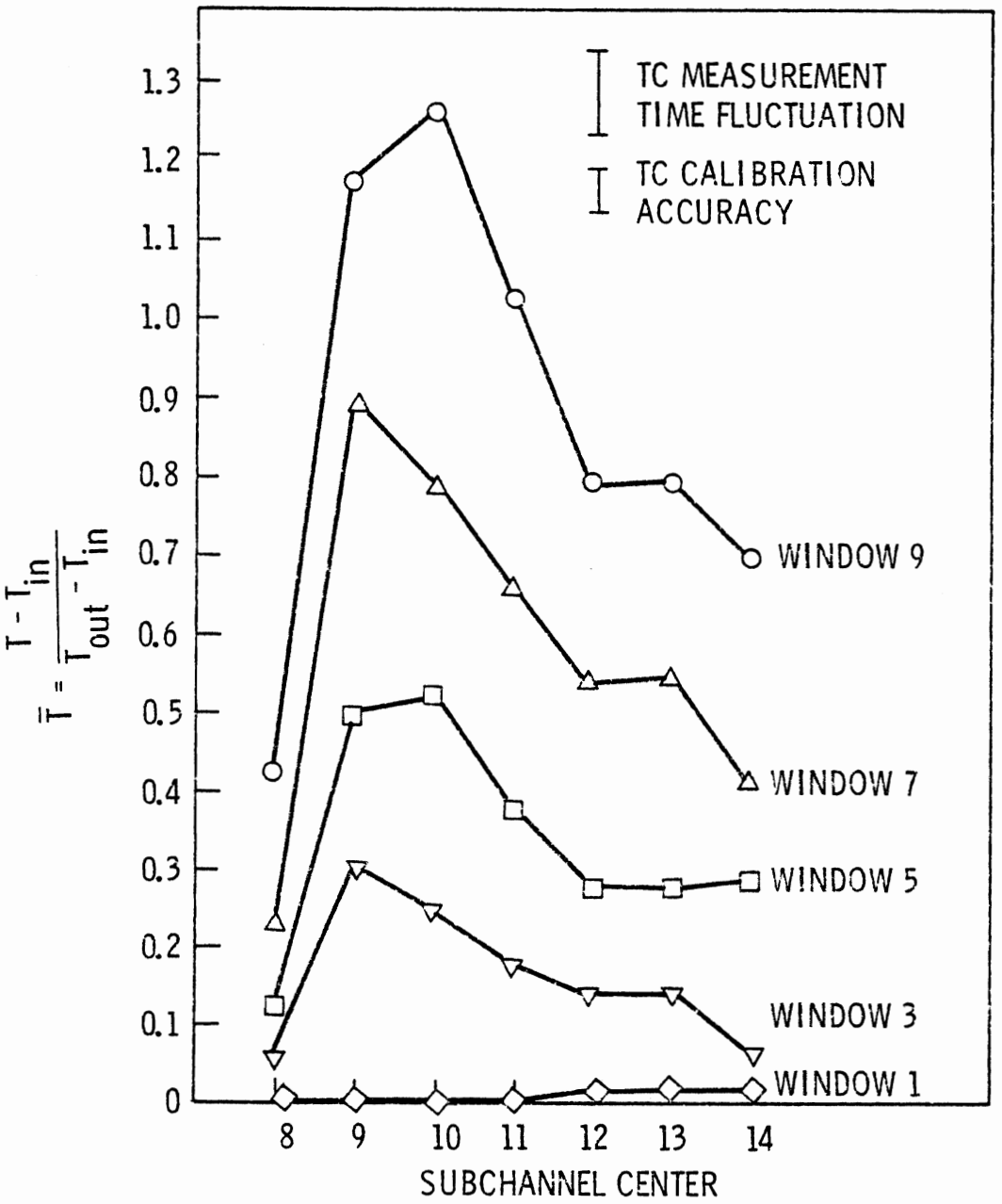

FIGURE 6-20. Case 1 Experimental Temperature Profiles, $\dot{W}$ = 2.47 gpm, $T_{out} - T_{in}$ = 30°F, Q_H/Q_L = 2:1

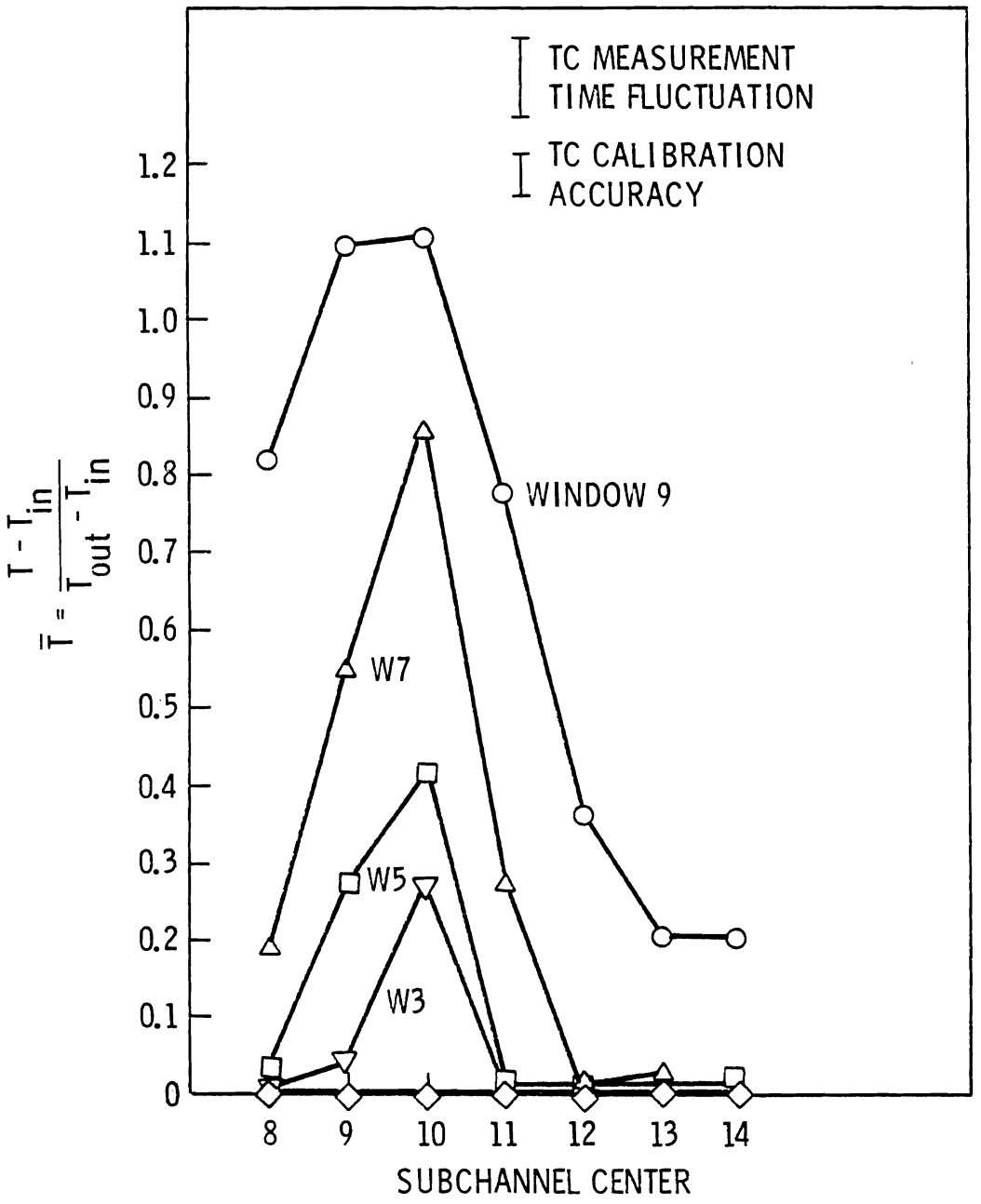

FIGURE 6-21. Case 2 Experimental Temperature Profiles, $\dot{W}$ = 1.25 gpm, $T_{out} - T_{in}$ = 33°F, Q_H/Q_L = 1:0

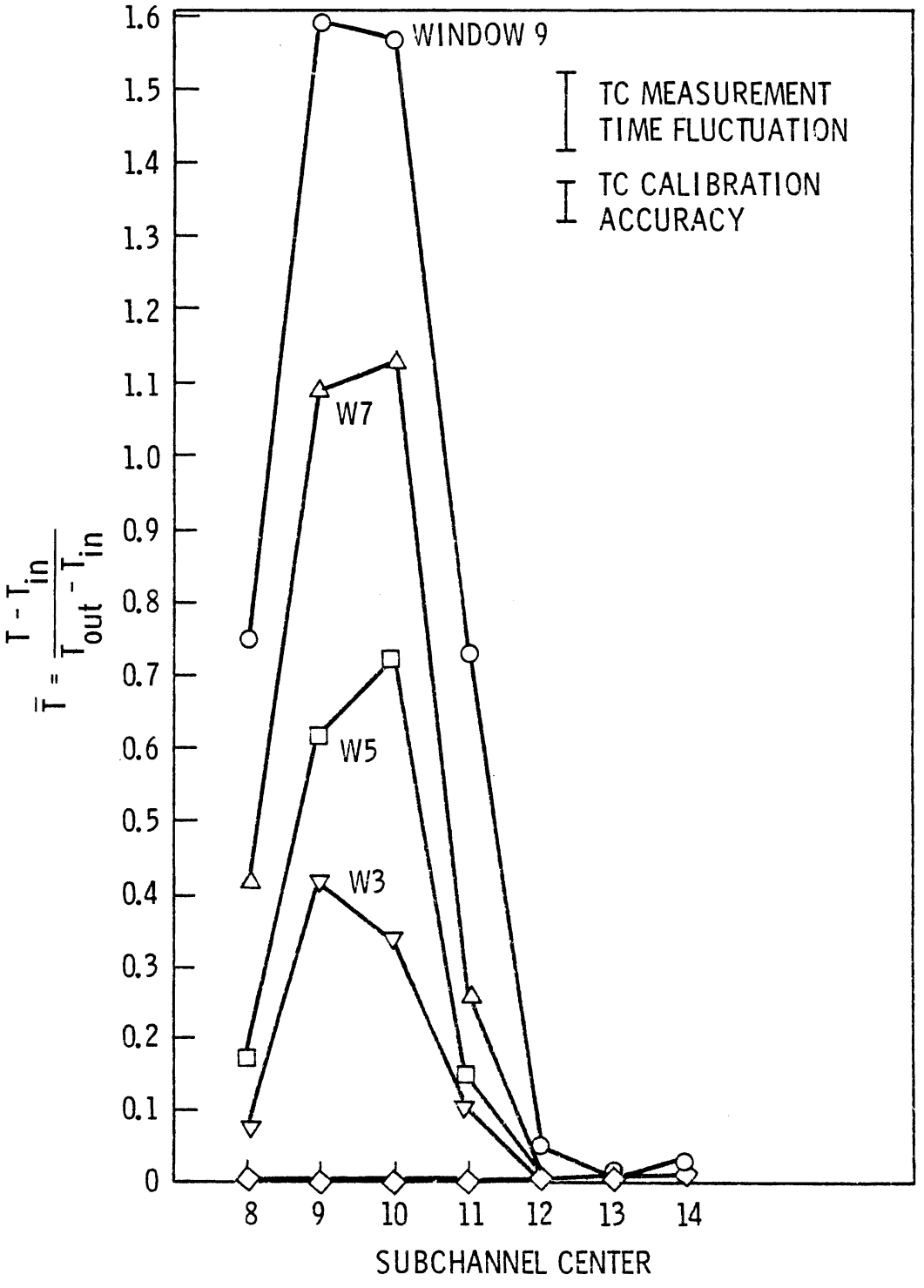

FIGURE 6-22. Case 3 Experimental Temperature Profiles, $\dot{W}$ = 2.47 gpm, $T_{out} - T_{in}$ = 31°F, Q_H/Q_L = 1:0

uniform and, as GR^*/Re^2 increased, the nondimensional velocity profiles became more skewed. A general trend is not evident for the temperature profile variation with GR^*/Re^2.

7.0 DATA COMPARISONS WITH THE COBRA-IV COMPUTER PROGRAM

The primary objective of this experimental program was to provide data to quantify the ability of the COBRA-IV computer program to predict velocity and temperature distributions in a rod bundle geometry with flows in the mixed free and forced convection regime. This section documents these data comparisons.

A brief discussion of the COBRA code is provided first to introduce the analysis method and highlight code input requirements. Next, results of parametric studies are presented to demonstrate the effect of friction factor and heat transfer modeling. These studies, conducted for Case 3, led to the selection of the analysis model subsequently used for the simulation of all three experiments. Results of the final comparisons are presented in Section 7.3 where it is shown that COBRA-IV velocity predictions agree quite well with the experimental data, and computed temperatures compare favorably with the measured values.

7.1 THE COBRA-IV COMPUTER PROGRAM

COBRA-IV is a computer program designed to predict the flow and enthalpy distribution in fuel rod bundles and reactor cores.[1] Geometric modeling considers a rod bundle to be divided into subchannels whose boundaries are defined by adjacent walls and/or rod surfaces. These flow channels are then divided axially to form discrete control volumes for which the conservation equations of mass, momentum and energy are solved numerically. The solution of these equations provides the enthalpy and axial and lateral flow rates for the computational cell.

In addition to geometric input requirements, boundary conditions for rod power and inlet flow rate and temperature, and input correlations for friction factor and turbulent mixing are required to numerically simulate these experiments.

7.2 COBRA MODEL AND PARAMETRIC STUDIES

The experimental geometry was modeled in COBRA with 21 subchannels and 12 rods as shown in Figure 3-3. Experimentally determined values of rod power and inlet temperature and flow were used for computational boundary conditions. The selection of other code input was based on the results of simulations for Case 3. Experimental Case 3 was arbitrarily selected as a reference to aid in determining an appropriate friction factor and to assess the effect of modeling heat loss from the bundle to the atmosphere.

Several friction factors, including a correlation for mixed free and forced convection flows,[6] were introduced into COBRA. It was determined that allowing the code to calculate and use the maximum of the smooth tube laminar and turbulent friction factors produced the best agreement between Case 3 and COBRA predictions. Therefore, that friction factor selection scheme was chosen as the standard for all computations. To investigate the significance of heat losses from the warm experimental bundle to the cooler atmosphere, calculations were performed both with and without the inclusion of this heat transfer mechanism. It was determined that the inclusion of heat transfer to the atmosphere was small and all reported computations neglect heat losses from the bundle.

Parametric studies were also performed to investigate the effect of heat transport by turbulent mixing between flow channels. Results of these calculations showed an uncertainty as to the benefit of including this transport mechanism in the analytical model. Turbulent exchange improved comparisons in some regions and provided worse comparisons in other areas. However, changes were generally small and turbulent mixing was not used for the results presented.

Table 7-1 summarizes what will be referred to as the reference COBRA model selected on the basis of these parametric studies for data Case 3. It is important to recognize that this modeling represents standard input correlations generally used for a majority of computations performed with the COBRA code.

7.3 COBRA PREDICTIONS

The results of computations performed with COBRA are documented and compared to experimental results in this section. All calculations were made using the reference model described above with inlet flow rates and rod powers determined from the average of measured quantities for a given test series. Experimental values of rod power and inlet flow were not exactly the same for every data plane within a given test series (see Tables B-7 through B-9). However, differences were slight, and calculations using the precise values of inlet flow and power measured for a given data plane showed minor differences between simulations using average power and flow conditions. Therefore, results presented in this section are based on the average test condition for each test series.

Cases 1 and 3 were simulated with the implicit solution algorithm in COBRA. Numerical difficulties precluded the use of this algorithm for Case 2 computations; COBRA's explicit algorithm was employed here instead.

TABLE 7-1. Standard COBRA-IV-I Input

INPUT PARAMETER	VALUE
Geometry	21 subchannels, 12 rods Bundle length - 72.0 inches Axial node size - 3.0 inches
Power Distribution	Average values measured for each test series
Inlet Flow and Temperature	Average value measured for each test series
Input Correlations	Friction factor - maximum of (64/Re, 0.184 $Re^{-.2}$)

7.3.1 COBRA Velocity Predictions

Computed velocities are presented in Tables B-4, B-5, and B-6 for Cases 1 through 3, respectively, and graphically compared to the experimental data in Figures 7-1 through 7-9. Horizontal bars represent calculated subchannel average velocities and discrete points are measured data.

Detailed velocity distributions were obtained along subchannel centerlines. However, as previously stated, thermal gradients precluded the

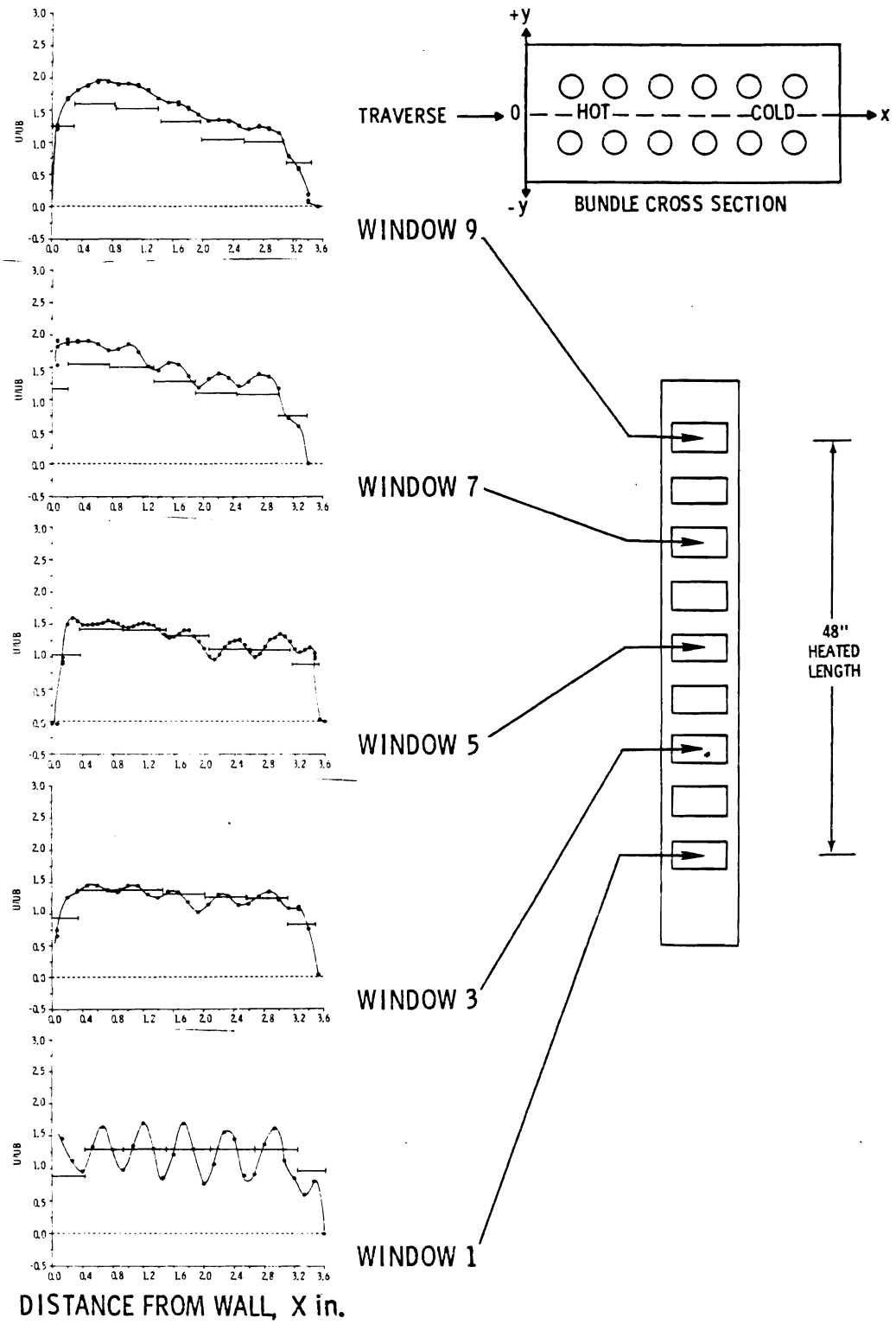

FIGURE 7-1. Case 1 Velocity Profiles Comparison, UB = 0.327 ft/sec, COBRA and Experimental Data, y = 0.0 in.

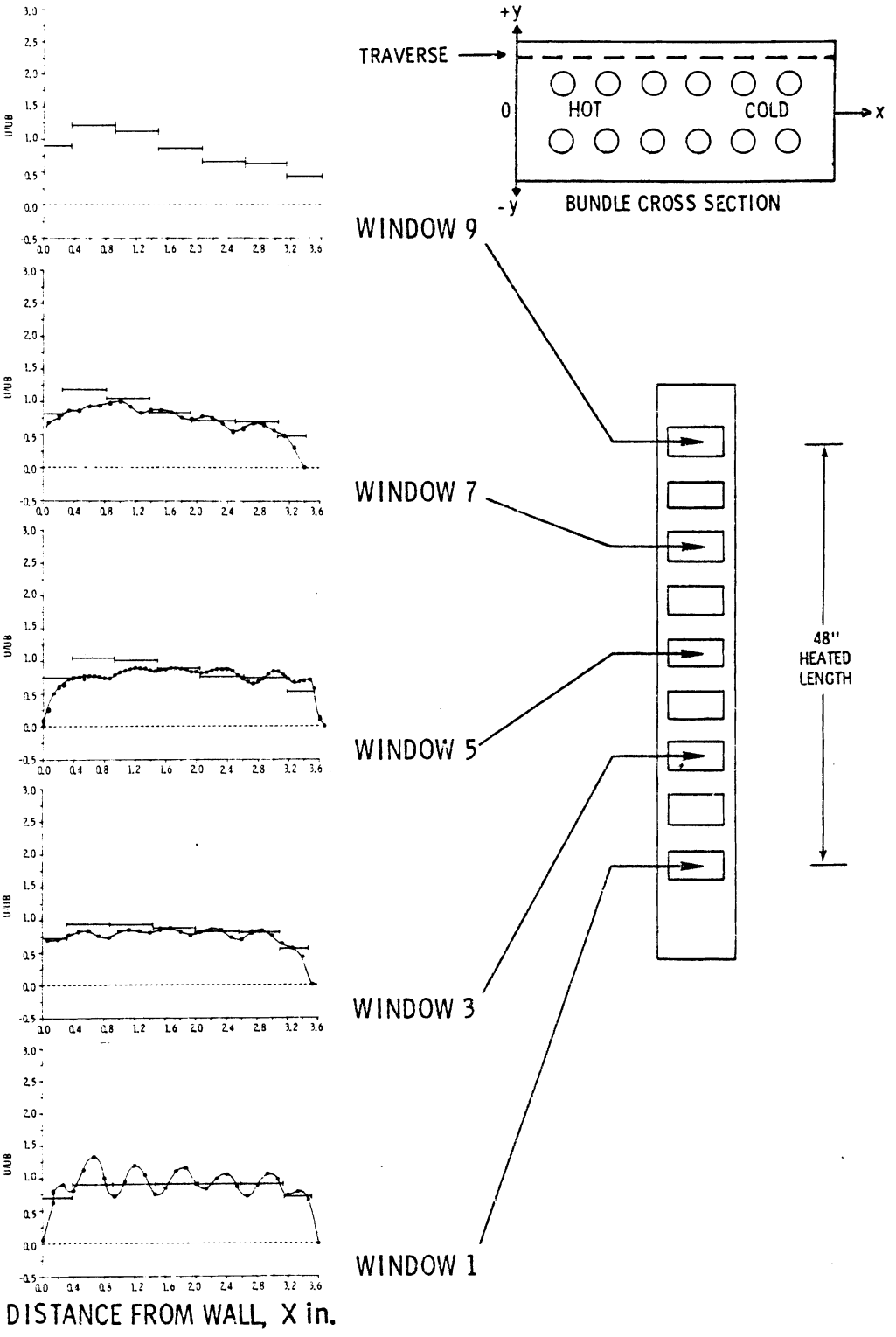

FIGURE 7-2. Case 1 Velocity Profiles Comparison, UB = 0.327 ft/sec, COBRA and Experimental Data, y = +0.581 in.

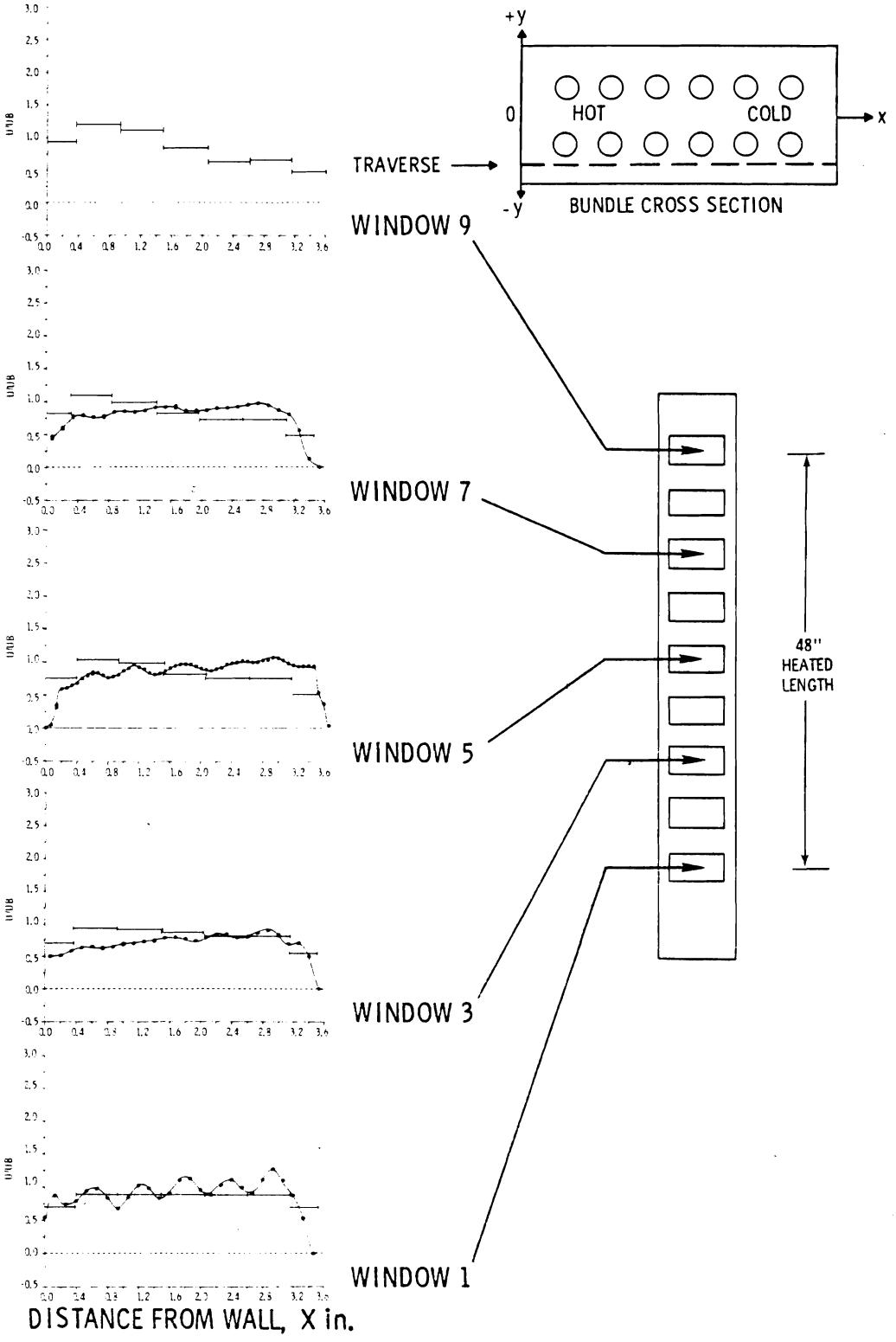

FIGURE 7-3. Case 1 Velocity Profiles Comparison, UB = 0.327 ft/sec, COBRA and Experimental Data, y = -0.581 in.

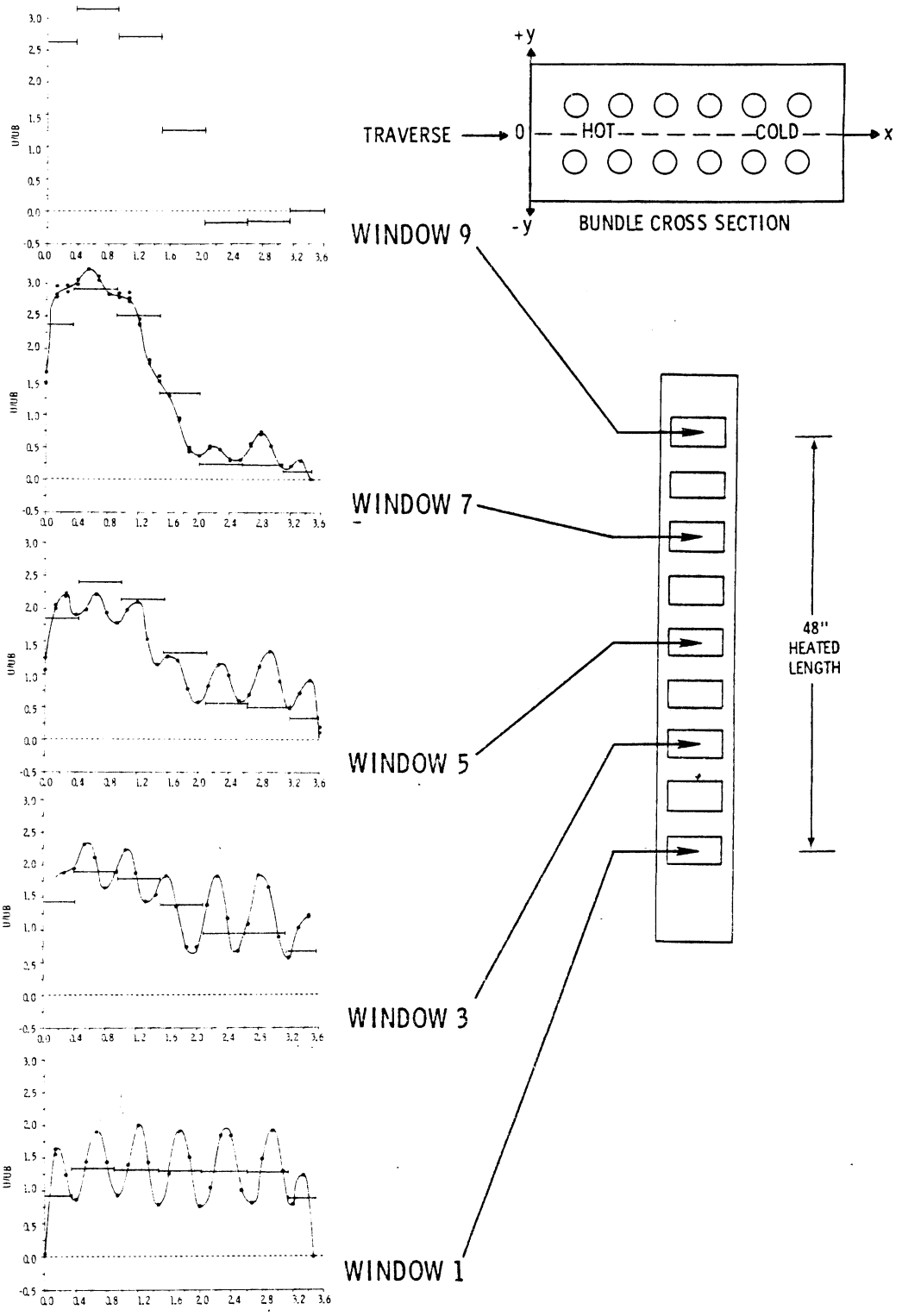

FIGURE 7-4. Case 2 Velocity Profiles Comparison, UB = 0.164 ft/sec, COBRA and Experimental Data, y = 0.0 in.

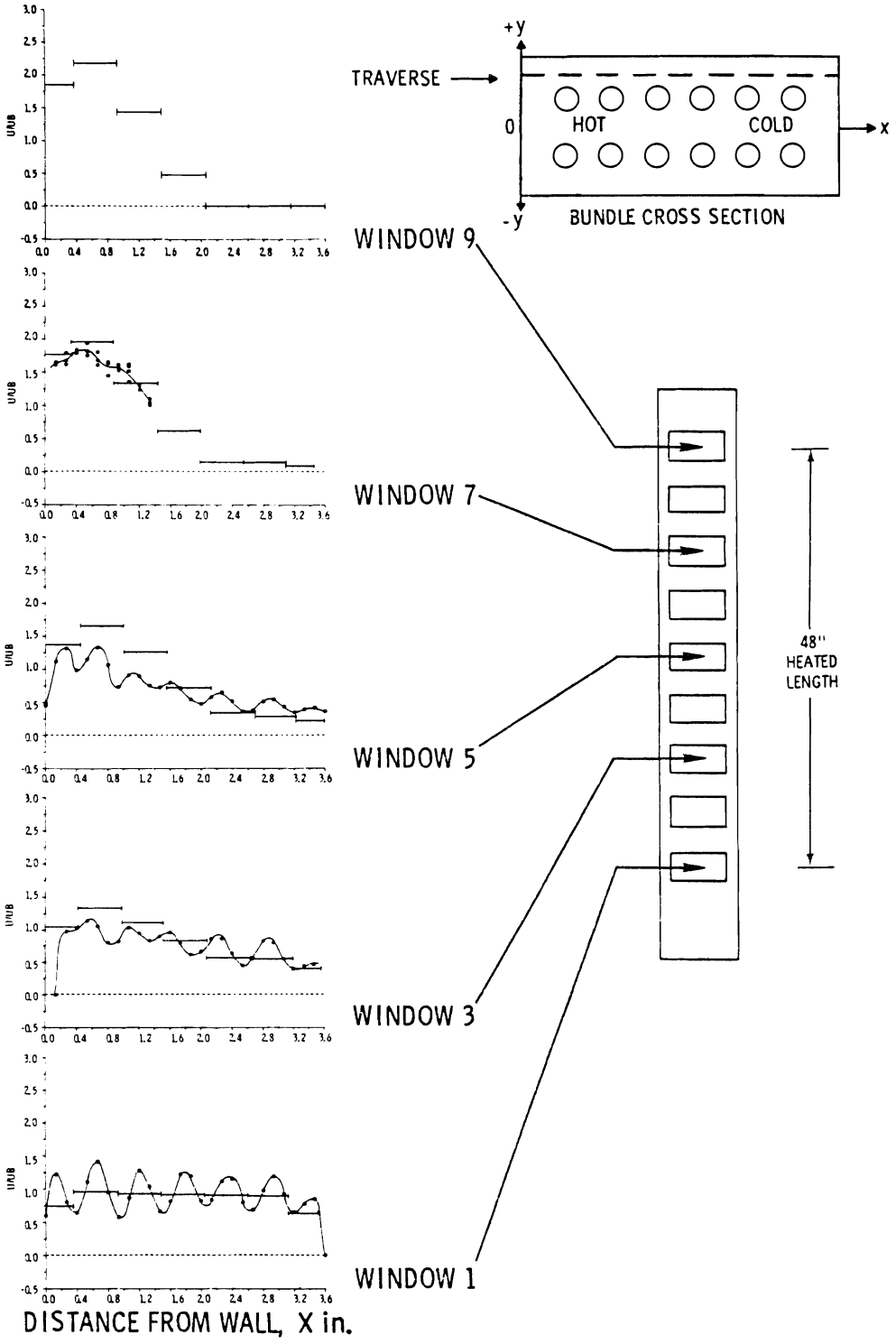

FIGURE 7-5. Case 2 Velocity Profiles Comparison, UB = 0.164 ft/sec, COBRA and Experimental Data, y = +0.581 in.

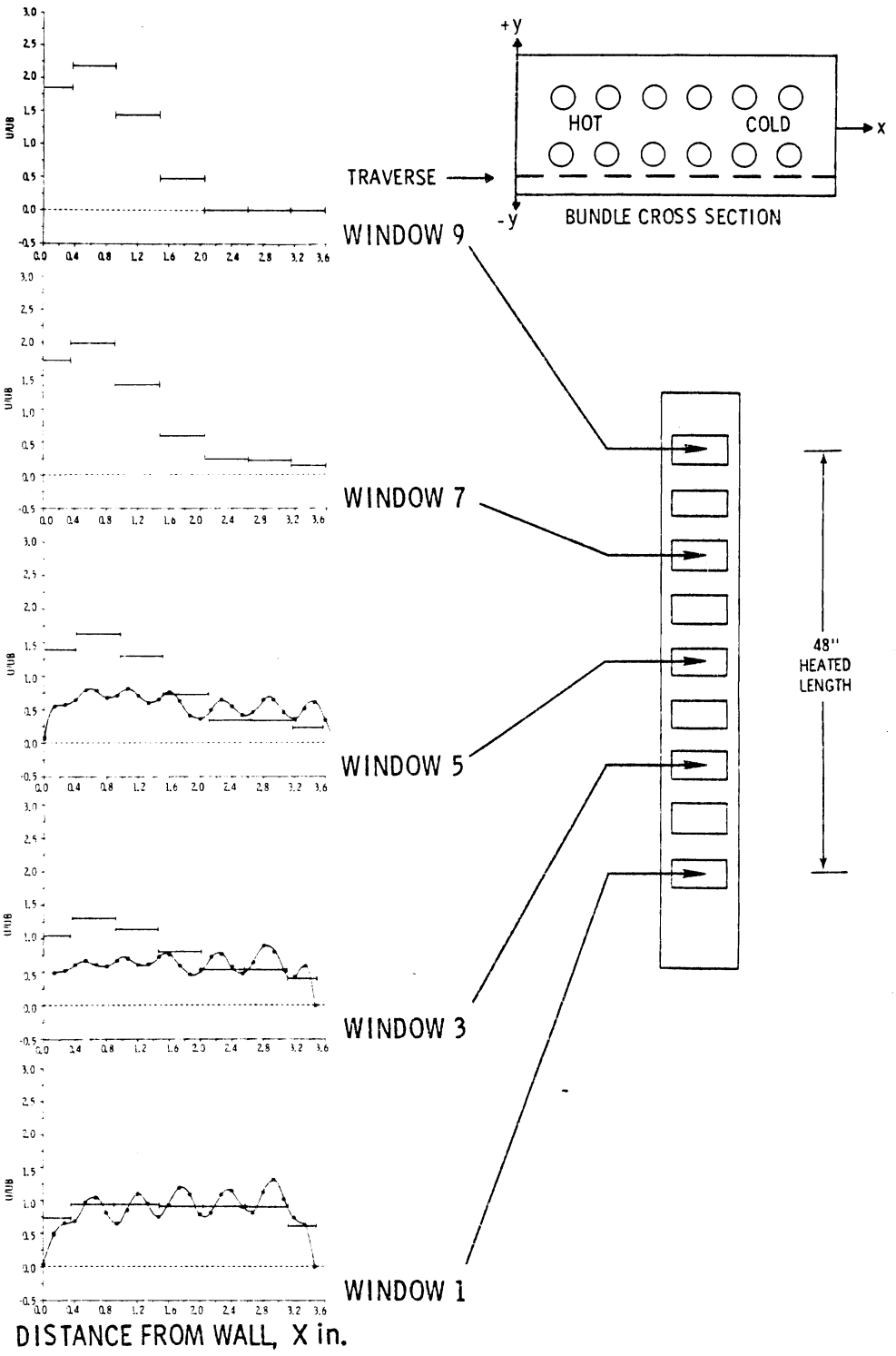

FIGURE 7-6. Case 2 Velocity Profiles Comparison, UB = 0.164 ft/sec, COBRA and Experimental Data, y = -0.581 in.

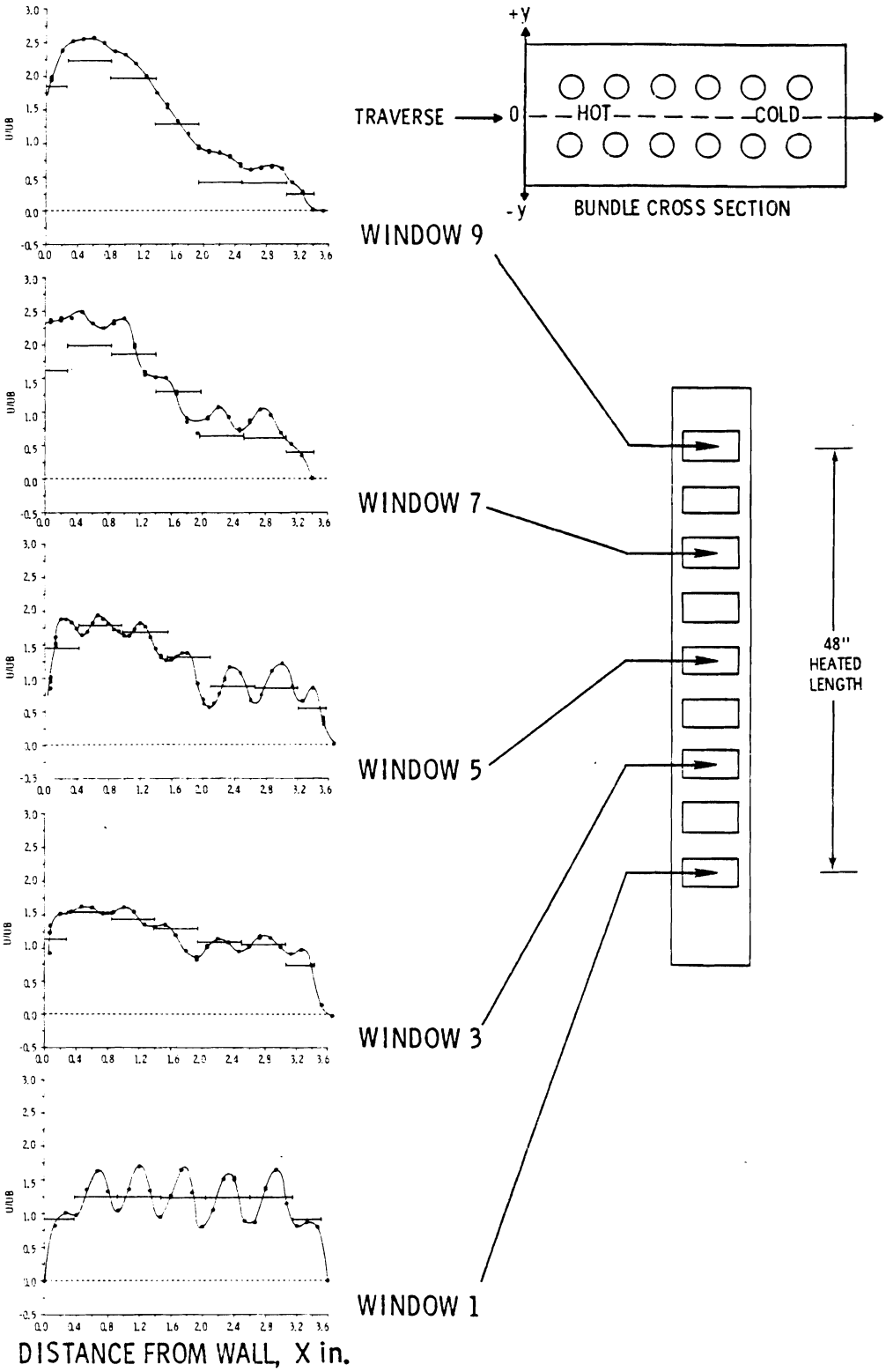

FIGURE 7-7. Case 3 Velocity Profiles Comparison, UB = 0.327 ft/sec, COBRA and Experimental Data, y = 0.0 in.

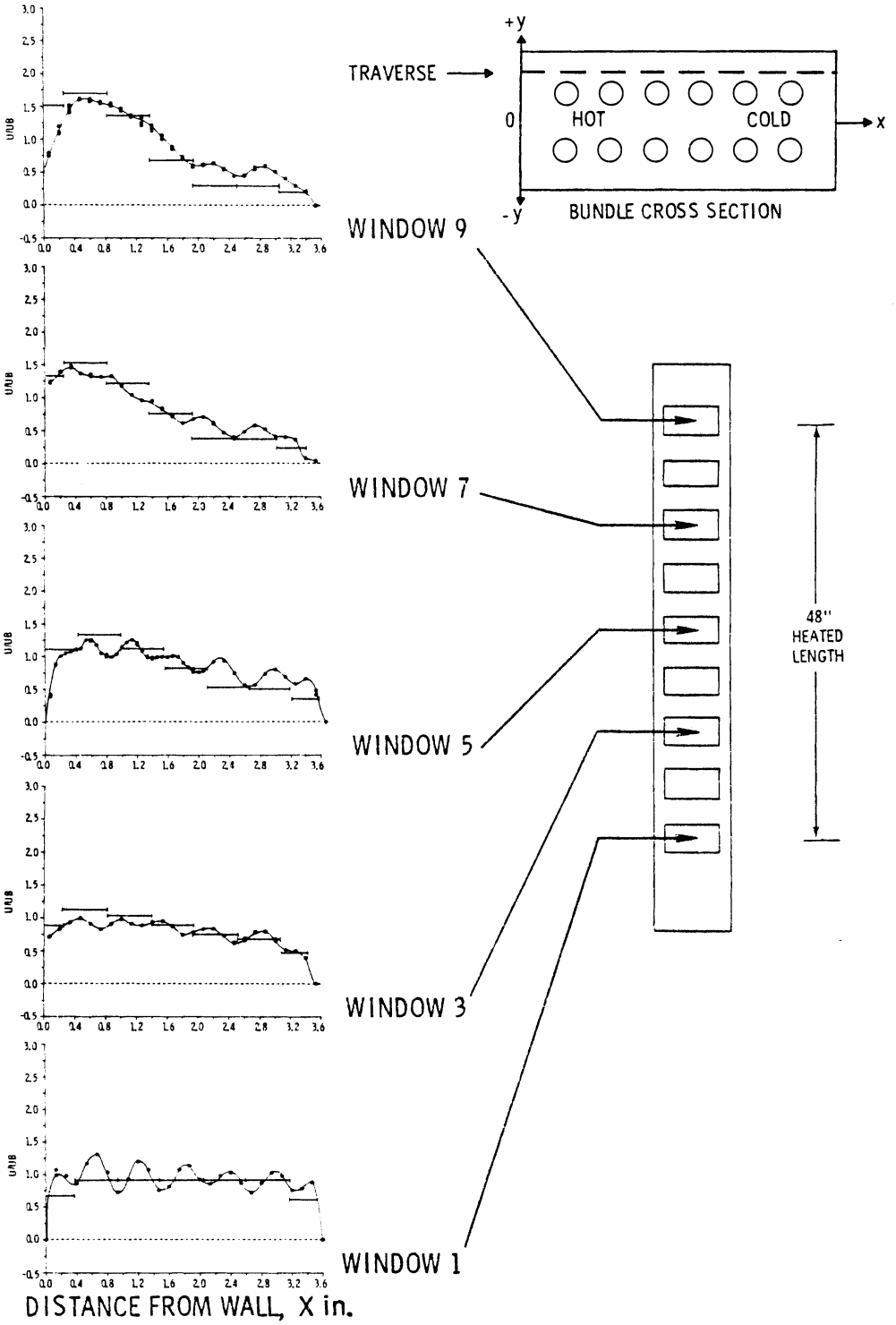

FIGURE 7-8. Case 3 Velocity Profiles Comparison, UB = 0.327 ft/sec, COBRA and Experimental Data, y = +0.581 in.

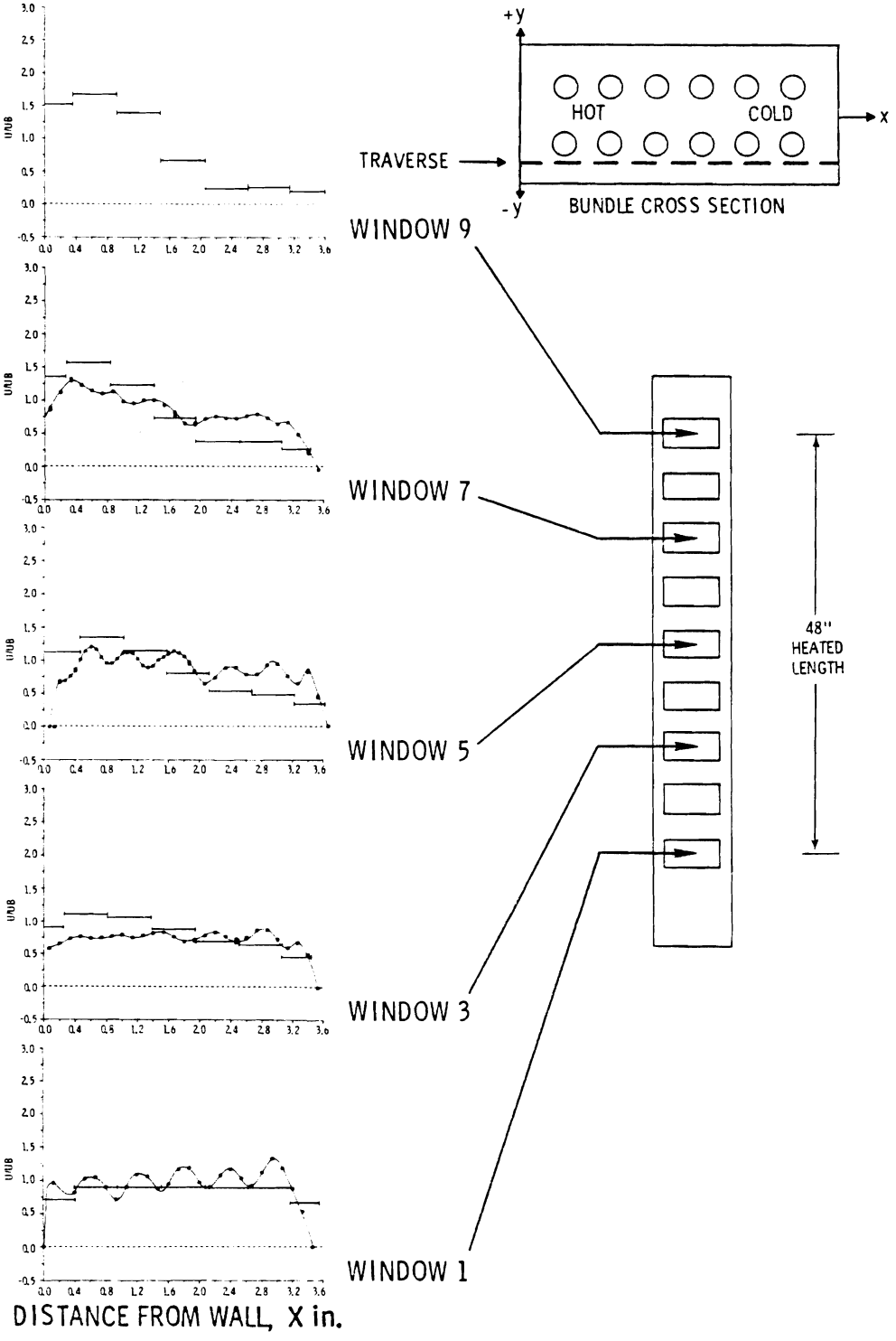

FIGURE 7-9. Case 3 Velocity Profiles Comparison, UB = 0.327 ft/sec, COBRA and Experimental Data, y = -0.581 in.

measurement of off-centerline velocities in many instances. Thus, it is not possible to calculate an exact subchannel average velocity from the experimental data. A simple numerical average of the centerline velocity distribution does, however, provide a reasonable velocity to which comparisons can be made.

In general, COBRA-calculated velocity profiles correspond quite well to the measured profiles. Exceptions are at y = -0.581 in. where the computed velocities are greater than the measured values for x < 1.8 in. and less than the measured values for x > 1.8 in. This difference is attributed to slight asymmetries in the bundle alignment which were not included in the numerical simulation.

The overall comparison seems to be excellent, particularly in the regions where steep velocity gradients exist. It was in these regions that COBRA's application was uncertain because it does not simulate the intrasubchannel flow structure. However, the comparison at Window 7, Case 2 (Figure 7-4) exemplifies COBRA's ability to do a good job even when velocity has changed by a factor of approximately 6 through one subchannel.

7.3.2 COBRA Temperature Predictions

Fluid temperatures computed by COBRA are tabulated in Tables B-1, B-2, and B-3 for Cases 1 through 3, respectively, and compared to the data graphically in Figures 7-10, 7-11, and 7-12.

In general, temperatures predicted by COBRA show the same trends as the measured profiles; however, computed temperatures are approximately 25 to 40 percent higher than the measured values. It is important to recognize that COBRA computes an average subchannel temperature whereas the measurements represent point values within a subchannel. For the flow and power conditions imposed in this experiment, it is quite possible that a significant temperature gradient existed within a subchannel. Thus, it may be difficult, if not impossible, to directly compare the measured and computed temperatures. For example, the temperature profile in a vertical tube under conditions similar to those of this experiment has been shown by numerous analyses and experiments to be parabolic.[7,8] If a parabolic temperature profile and a 40 to 70°F temperature difference between the

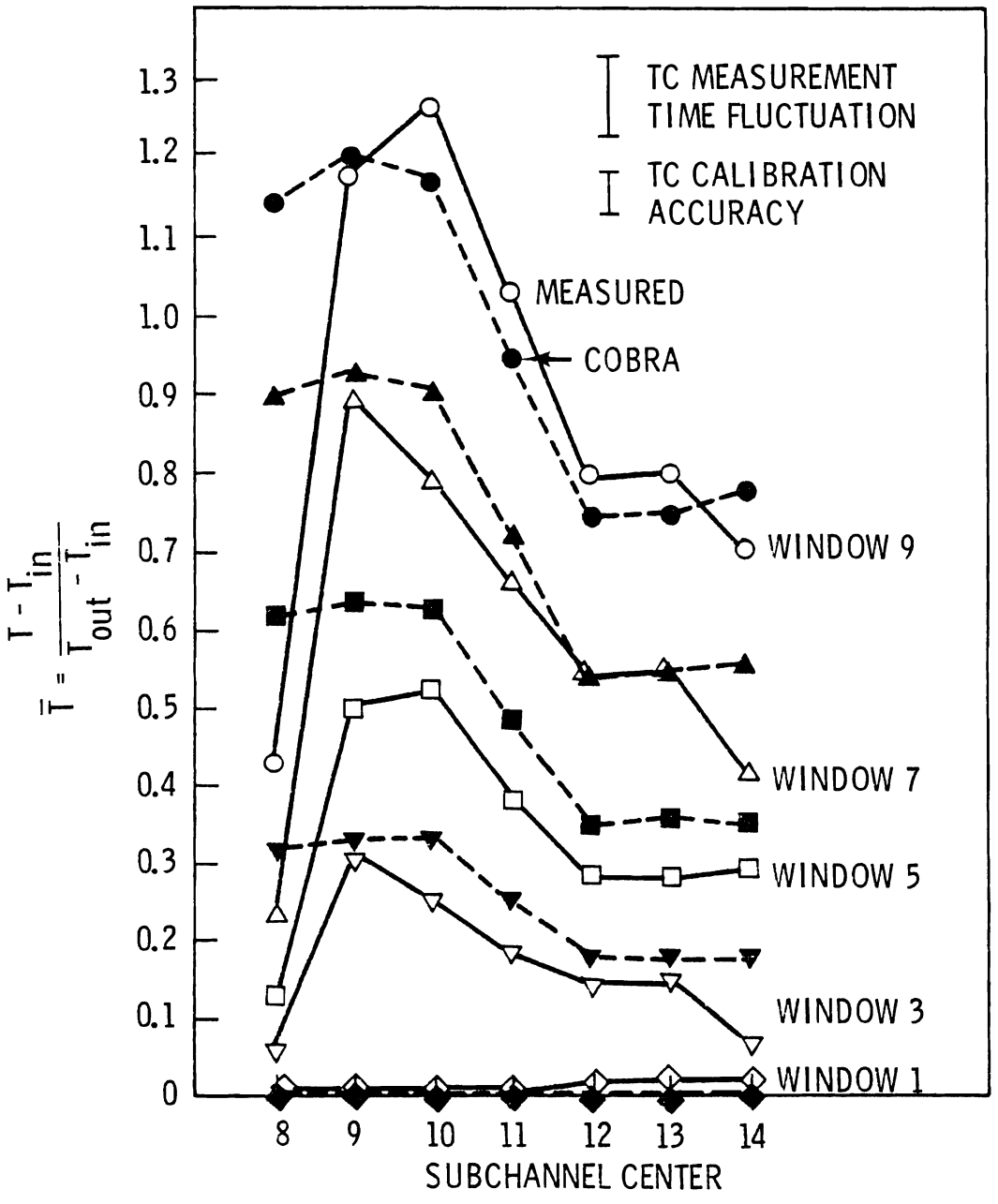

FIGURE 7-10. Case 1 Temperature Profiles Comparison, $\dot{W}$ = 2.47 gpm, COBRA and Experimental Data, $T_{out} - T_{in}$ = 30°F

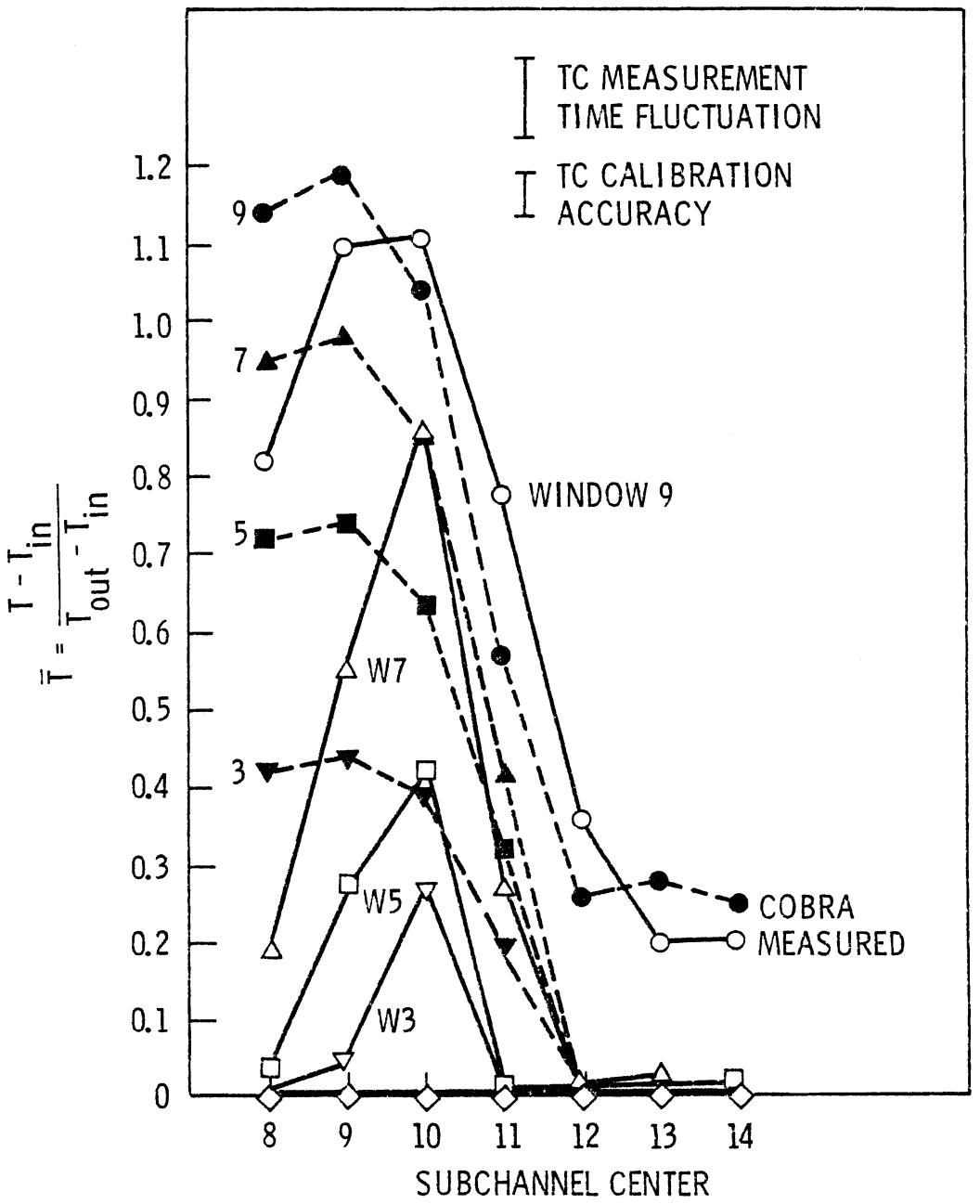

FIGURE 7-11. Case 2 Temperature Profiles Comparison, $\dot{W}$ = 1.25 gpm, COBRA and Experimental Data, $T_{out} - T_{in}$ = 33°F

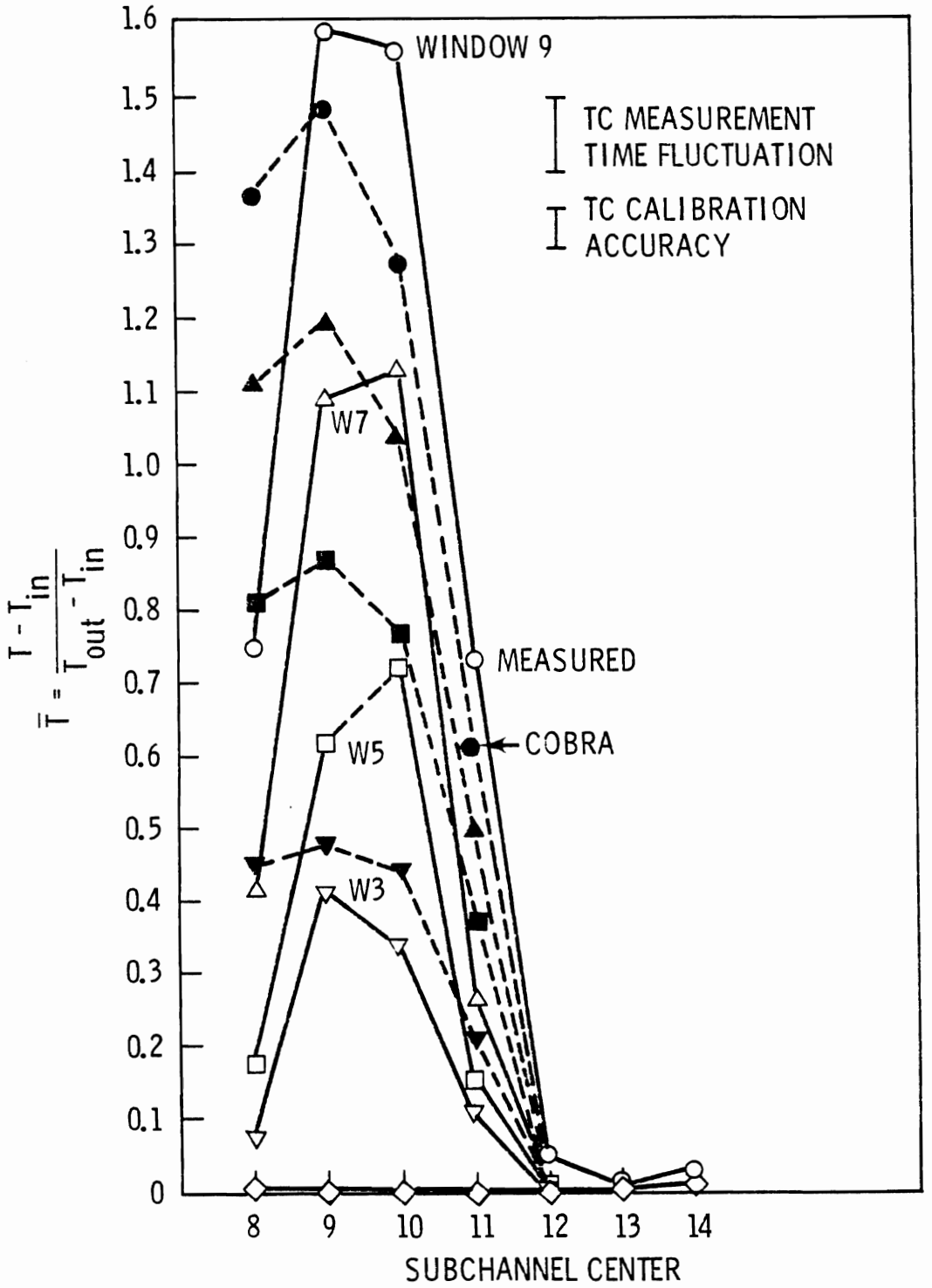

FIGURE 7-12. Case 3 Temperature Profiles Comparison, $\dot{W}$ = 2.47 gpm, COBRA and Experimental Data, $T_{out} - T_{in}$ = 31°F

heater rod wall and subchannel center were assumed, the average subchannel temperature would be 20 to 60 percent higher than the center temperature. Thus, point measurements may not provide sufficient information to quantify COBRA's ability to predict fluid temperatures under these flow conditions.

It is important to note the large difference between the measured and predicted temperature for Subchannel 8, a wall subchannel. A possible explanation for the difference could be a steep temperature gradient in that region. As mentioned in Section 5.0, there was some uncertainty in the thermocouple position, and position may have been particularly important near the wall.

The computed and experimental temperature profile at Window 9 for Case 2 shows that a flow reversal existed in the upper regions of the cold side of the bundle. Both the velocity measurements and COBRA calculations indicated that flow moved laterally from the cold side of the bundle to the hot. Thus, because there was no heating on the cold side of the bundle in Case 2, flows must have reversed with warm liquid entering from above. The elevated temperatures in this region were computed by assuming that, when the flow reversed, liquid entered the bundle at the mixed temperature measured at the bundle exit. As previously stated, velocity measurements could not be obtained at this position; however, the measured temperatures indicate that the COBRA-predicted flow reversal did occur.

Considering possible temperature distribution effects and the fact that computed velocities were in good agreement with experimental values, it seems that COBRA provides a reasonable estimate for the subchannel average fluid temperature. However, to fully quantify COBRA's capacity, a detailed measurement of the subchannel temperature profile is required.

REFERENCES

1. C. L. Wheeler, C. W. Stewart, R. J. Cena, D. S. Rowe and A. M. Sutey, COBRA-IV-I: An Interim Version of COBRA for Thermal Hydraulic Analysis of Rod Bundle Nuclear Fuel Elements and Cores. BNWL-1962, Battelle, Pacific Northwest Laboratories, Richland, WA 99352, March 1976.

2. C. Tsai, A. A. Bishop and R. A. Markley, Effects of Buoyancy Force on the Velocity and Temperature Distributions in an LMFBR Radial Blanket Fuel Rod Assembly. Paper No. 73-HT-58, American Society of Mechanical Engineers, New York, NY, August 1973.

3. E. U. Khan, W. M. Rohsenow, A. A. Souin, and N. E. Todreas, "A Porous Body Model for Predicting Temperature Distribution in Wire-Wrapped Rod Assemblies Operating in Combined Forced and Free Convection." Nuclear Engineering and Design, No. 35, pp. 199-211, 1975.

4. J. M. Creer, D. S. Rowe, J. M. Bates and A. M. Sutey, Effects of Sleeve Blockages on Axial Velocity and Intensity of Turbulence in an Unheated 7x7 Rod Bundle. BNWL-1965, Battelle, Pacific Northwest Laboratories, Richland, WA 99352, January 1976.

5. H. Schenck, Jr., Theories of Engineering Experimentation. McGraw-Hill Book Company, New York, NY, p. 40, 1961.

6. G. A. Kemeny and E. V. Somers, "Combined Free and Forced-Convective Flow in Vertical Circular Tubes -- Experiments with Water and Oil." Journal of Heat Transfer. 84(4):339-46, November 1962.

7. T. M. Hallman, Combined Forced and Free-Laminar Heat Transfer in Vertical Tubes with Uniform Internal Heat Generation. Paper No. 55-A-73, American Society of Mechanical Engineers, New York, NY, November 1956.

8. W. T. Lawrence and J. C. Chato, "Heat Transfer Effects on the Developing Laminar Flow inside Vertical Tubes." Journal of Heat Transfer. 88(2):214-222, May 1966.

ACKNOWLEDGMENTS

Appreciation is extended to R. G. Neuhold of the Energy Research and Development Administration, Division of Reactor Research and Development for supporting the combined convection study. The project was successfully completed due to the outstanding efforts of several Energy Systems Engineering Section staff members. The authors wish to acknowledge the contributions of: K. D. Hinkle for fabrication, assembly, and installation of equipment; R. R. Dohaniuk for instrumentation setup and trouble-shooting; J. M. Creer for technical assistance; A. M. Sutey for management; and D. J. Ward for typing the final draft. The authors also appreciate the assistance of Fluid and Thermal Engineering Section members: T. L. George for COBRA updates and programming; D. R. Roberts for plotting COBRA data; and C. L. Wheeler for project leadership. Recognition and thanks go to A. J. Currie for editing and organizing the final draft and to the graphics and technical publications section of PNL for preparation of illustrations and the final report.

APPENDIX A

NOMENCLATURE

APPENDIX A

NOMENCLATURE

A = Amps

C_p = Specific heat

D_H = Hydraulic diameter

F_D = Doppler frequency

F = Function

GR = Grashof number, $(g\beta\Delta T_B D_H^3)/\nu^2$

GR^* = Modified Grashof number, $GR(\overline{Q} - 1)$

GR^*/Re^2 = $[(g\beta D_H \Delta T_B)/U^2](\overline{Q} - 1)$

I = Rod current

L = Rod bundle length

P = Heater rod power, VI

Pr = Prandtl number

Q_H = Hot side heat flux

Q_L = Cool side heat flux

$\overline{Q}$ = $Q_H/[(Q_H + Q_L)/2]$

R = General result

Re = Reynolds number, $(UD_H)/\nu$

T = Temperature

$\overline{T}$ = Nondimensional temperature, $(T - T_{in})/(T_{out} - T_{in})$

T_{in} = Inlet temperature

T_{out} = Outlet temperature

ΔT_B = Temperature difference across the bundle, $T_{out} - T_{in}$

U = Axial velocity

UB = Bundle average velocity, $\dot{W}/a$

U_{max} = Maximum velocity

U_{min} = Minimum velocity

V = Rod voltage

W = Uncertainty

$\dot{W}$ = Volumetric flow rate

X_m = Measured X value

Y_m = Measured Y value

a = Rod bundle flow area

d = Rod diameter

g = Gravitational constant

p = Rod pitch

x = x coordinate

y = y coordinate

z = z coordinate

β = Thermal expansion coefficient, 1/°F

$\Theta/2$ = Laser beam intersection half angle

λ = Laser light wavelength

ν = Kinematic viscosity

ρ = Density

APPENDIX B

TABLES

TABLE B-1. Subchannel Temperatures

Case No.: 1
Power Skew: 2:1
$\dot{W}$: 2.47 gpm

Window Number	Data Type	T_{in} (°F)	T_{out} (°F)	ΔT_B (°F)	Subchannel Temperature (°F)						
					8	9	10	11	12	13	14
1	Measured	55.6	87.2	21.6	55.5	55.6	55.7	55.9	56.1	56.1	56.3
	COBRA	59.62	88.04	28.42	59.62	59.62	59.62	59.62	59.62	59.62	59.62
3	Measured	56.2	88.0	31.8	58.0	66.0	64.1	61.9	60.7	60.7	58.2
	COBRA	59.62	88.04	28.42	68.65	69.13	68.95	66.72	64.56	64.59	64.38
5	Measured	61.7	95.6	33.9	66.0	78.8	79.5	74.5	71.3	71.3	71.5
	COBRA	59.62	88.04	28.42	77.19	77.84	77.44	73.46	69.66	69.73	69.65
7	Measured	61.8	92.1	30.3	68.9	89.1	85.6	81.9	78.2	78.4	74.2
	COBRA	59.62	88.04	28.42	85.14	86.15	85.43	80.04	75.03	75.14	75.40
9	Measured	60.1	88.6	28.5	72.3	94.0	96.2	89.4	82.7	82.8	80.0
	COBRA	59.62	88.04	28.42	92.41	94.08	93.00	86.55	80.84	80.99	81.71

TABLE B-2. Subchannel Temperatures

Case No.: 2
Power Skew: 1:0
$\dot{W}$: 1.25 gpm

Window Number	Data Type	T_{in} (°F)	T_{out} (°F)	ΔT_B (°F)	Subchannel Temperature (°F)						
					8	9	10	11	12	13	14
1	Measured	60.2	93.1	32.9	59.1	59.1	59.1	59.3	59.4	59.4	59.6
	COBRA	60.4	89.5	29.1	60.40	60.40	60.40	60.40	60.40	60.40	60.40
3	Measured	60.6	93.1	32.5	60.8	61.77	69.2	60.8	60.9	60.9	61.1
	COBRA	60.4	89.5	29.1	72.65	73.17	71.67	65.79	60.40	60.40	60.40
5	Measured	59.3	92.4	33.1	60.5	68.2	73.3	59.7	59.4	59.4	59.9
	COBRA	60.4	89.5	29.1	81.45	81.95	78.99	69.58	60.40	60.40	60.40
7	Measured	59.5	92.6	33.1	65.6	77.6	88.2	68.3	59.8	60.0	60.6
	COBRA	60.4	89.5	29.1	88.06	88.85	85.39	72.67	60.40	60.40	60.40
9	Measured	62.6	96.1	33.5	89.9	99.5	99.7	88.5	74.7	69.2	69.3
	COBRA	60.4	89.5	29.1	93.50	94.93	90.79	76.88	67.98	68.56	67.54

TABLE B-3. Subchannel Temperatures

Case No.: 3
Power Skew: 1:0
$\dot{W}$: 2.47 gpm

Window Number	Data Type	T_{in} (°F)	T_{out} (°F)	ΔT_B (°F)	Subchannel Temperature (°F)						
					8	9	10	11	12	13	14
1	Measured										
	COBRA	60.9	91.01	30.11	60.90	60.90	60.90	60.90	60.90	60.90	60.90
3	Measured	61.1	93.3	32.2	63.5	74.4	72.1	64.5	61.3	61.4	61.6
	COBRA	60.9	91.01	30.11	74.44	75.32	74.14	67.27	60.90	60.90	60.90
5	Measured	61.9	97.5	35.6	68.1	84.1	87.6	67.1	62.1	62.1	62.3
	COBRA	60.9	91.01	30.11	85.31	87.04	84.11	72.04	60.90	60.90	60.90
7	Measured	61.8	92.3	30.5	74.5	95.1	96.4	69.6	61.9	62.0	62.3
	COBRA	60.9	91.01	30.11	94.32	96.97	92.23	75.98	60.90	60.90	60.90
9	Measured	59.7	88.7	29.1	81.5	106.1	105.3	81.0	61.0	59.9	60.6
	COBRA	60.9	91.01	30.11	102.29	105.69	99.35	79.56	60.90	60.90	60.90

TABLE B-4. Case 1 COBRA Subchannel Average Velocities

UB = 0.327 ft/sec

Subchannel Number	Window 1 U (ft/sec)	Window 1 U/UB	Window 3 U (ft/sec)	Window 3 U/UB	Window 5 U (ft/sec)	Window 5 U/UB	Window 7 U (ft/sec)	Window 7 U/UB	Window 9 U (ft/sec)	Window 9 U/UB
1	0.2219	0.6786	0.2285	0.6988	0.2479	0.7581	0.2741	0.8382	0.3019	0.9232
2	0.3013	0.9214	0.3186	0.9743	0.3393	1.0376	0.3655	1.1177	0.3975	1.2156
3	0.3032	0.9272	0.3156	0.9651	0.3294	1.0073	0.3446	1.0538	0.3637	1.1122
4	0.3030	0.9266	0.2937	0.8982	0.2873	0.8786	0.2807	0.8584	0.2768	0.8465
5	0.3027	0.9257	0.2728	0.8343	0.2495	0.7630	0.2313	0.7073	0.2113	0.6462
6	0.3001	0.9177	0.2693	0.8235	0.2486	0.7602	0.2320	0.7095	0.2129	0.6511
7	0.2210	0.6758	0.1882	0.5755	0.1729	0.5287	0.1611	0.4927	0.1496	0.4575
8	0.3017	0.9226	0.3175	0.9709	0.3415	1.0443	0.3734	1.1419	0.4104	1.2550
9	0.4087	1.2498	0.4550	1.3914	0.4828	1.4765	0.5032	1.5388	0.5241	1.6028
10	0.4110	1.2569	0.4545	1.3899	0.4791	1.4651	0.4945	1.5122	0.5095	1.5581
11	0.4106	1.2557	0.4309	1.3177	0.4392	1.3431	0.4343	1.3281	0.4274	1.3070
12	0.4103	1.2547	0.4061	1.2419	0.3887	1.1887	0.3646	1.1150	0.3313	1.0131
13	0.4078	1.2471	0.4026	1.2312	0.3853	1.1783	0.3620	1.1070	0.3296	1.0080
14	0.3008	0.9199	0.2727	0.8339	0.2489	0.7612	0.2292	0.7009	0.2084	0.6373
15	0.2219	0.6786	0.2286	0.6991	0.2468	0.7547	0.2726	0.8336	0.3002	0.9180
16	0.3025	0.9251	0.3187	0.9746	0.3393	1.0376	0.3658	1.1187	0.3982	1.2177
17	0.3032	0.9272	0.3156	0.9651	0.3297	1.0083	0.3457	1.0572	0.3664	1.1205
18	0.3030	0.9266	0.2937	0.8982	0.2873	0.8786	0.2807	0.8584	0.2783	0.8511
19	0.3027	0.9257	0.2728	0.8343	0.2488	0.7609	0.2297	0.7024	0.2102	0.6428
20	0.3015	0.9220	0.2697	0.8248	0.2462	0.7529	0.2274	0.6954	0.2085	0.6376
21	0.2207	0.6749	0.1882	0.5755	0.1740	0.5321	0.1625	0.4969	0.1500	0.4587

y = -0.581 (between subchannels 4 and 5)

y = 0.0 (between subchannels 10 and 11)

y = +0.581 (between subchannels 17 and 18)

TABLE B-5. Case 2 COBRA Subchannel Average Velocities

UB = 0.164 ft/sec

		Window Number									
		1		3		5		7		9	
	Subchannel Number	U (ft/sec)	U/UB	U (ft/sec)	U/UB	U (ft/sec)	U/UB	U (ft/sec)	U/UB	U (ft/sec)	U/UB
	1	0.1166	0.7110	0.1746	1.0646	0.2270	1.3841	0.2807	1.7116	0.3006	1.8329
	2	0.1565	0.9543	0.2184	1.3317	0.2686	1.6378	0.3176	1.9366	0.3576	2.1805
	3	0.1557	0.9494	0.1897	1.1567	0.2089	1.2738	0.2165	1.3201	0.2379	1.4506
y = -0.581	4	0.1523	0.9287	0.1365	0.8323	0.1190	0.7256	0.0982	0.5988	0.0779	0.4750
	5	0.1495	0.9116	0.0951	0.5799	0.0549	0.3348	0.0203	0.1238	0.0000	0.0000
	6	0.1484	0.9049	0.0928	0.5659	0.0536	0.3268	0.0198	0.1207	-0.0000	0.0000
	7	0.1084	0.6610	0.0649	0.3957	0.0377	0.2299	0.0139	0.0848	-0.0000	0.0000
	8	0.1574	0.9598	0.2315	1.4116	0.3045	1.8567	0.3810	2.3232	0.4299	2.6213
	9	0.2205	1.3445	0.3085	1.8811	0.3973	2.4226	0.4707	2.8701	0.5171	3.1530
	10	0.2203	1.3433	0.2889	1.7616	0.3485	2.1250	0.4057	2.4738	0.4439	2.7067
y = 0.0	11	0.2174	1.3255	0.2240	1.3659	0.2219	1.3530	0.2135	1.3018	0.1851	1.1287
	12	0.2146	1.3085	0.1546	0.9427	0.0894	0.5451	0.0328	0.2000	-0.0027	-.0165
	13	0.2134	1.3012	0.1515	0.9238	0.0873	0.5323	0.0319	0.1945	-0.0027	-.0159
	14	0.1495	0.9116	0.0940	0.5732	0.0536	0.3268	0.0198	0.1207	-0.0000	0.0000
	15	0.1169	0.7128	0.1749	1.0665	0.2273	1.3860	0.2810	1.7134	0.2998	1.8280
	16	0.1568	0.9561	0.2187	1.3335	0.2689	1.6396	0.3176	1.9366	0.3552	2.1659
	17	0.1560	0.9512	0.1900	1.1585	0.2092	1.2756	0.2155	1.3140	0.2312	1.4098
y = +0.581	18	0.1526	0.9305	0.1368	0.8341	0.1192	0.7268	0.0985	0.6006	0.0773	0.4713
	19	0.1498	0.9134	0.0955	0.5823	0.0551	0.3360	0.0203	0.1238	0.0000	0.0000
	20	0.1488	0.9073	0.0932	0.5683	0.0538	0.3280	0.0199	0.1213	-0.0000	0.0000
	21	0.1088	0.6634	0.0652	0.3976	0.0378	0.2305	0.0139	0.0849	-0.0000	0.0000

TABLE B-6. Case 3 COBRA Subchannel Average Velocities

UB = 0.327 ft/sec

		Window Number									
		1		3		5		7		9	
	Subchannel Number	U (ft/sec)	U/UB	U (ft/sec)	U/UB	U (ft/sec)	U/UB	U (ft/sec)	U/UB	U (ft/sec)	U/UB
	1	0.2235	0.6836	0.2877	0.8798	0.3615	1.1055	0.4409	1.3483	0.5078	1.5529
	2	0.3028	0.9260	0.3696	1.1303	0.4419	1.3514	0.5055	1.5459	0.5533	1.6920
	3	0.3041	0.9300	0.3474	1.0624	0.3787	1.1581	0.4063	1.2425	0.4392	1.3431
	4	0.3032	0.9272	0.2873	0.8786	0.2655	0.8119	0.2420	0.7401	0.2218	0.6783
	5	0.3022	0.9242	0.2296	0.7021	0.1726	0.5278	0.1258	0.3847	0.0856	0.2618
y = -0.581	6	0.2990	0.9144	0.2241	0.6853	0.1690	0.5168	0.1244	0.3804	0.0860	0.2630
	7	0.2200	0.6728	0.1570	0.4801	0.1158	0.3541	0.0834	0.2550	0.0573	0.1752
	8	0.3033	0.9275	0.3785	1.1575	0.4717	1.4425	0.5488	1.6783	0.6074	1.8575
	9	0.4094	1.2520	0.5030	1.5382	0.5807	1.7758	0.6542	2.0006	0.7213	2.2058
	10	0.4112	1.2575	0.4753	1.4535	0.5495	1.6804	0.6007	1.8370	0.6467	1.9777
y = 0.0	11	0.4101	1.2541	0.4317	1.3202	0.4369	1.3361	0.4312	1.3187	0.4223	1.2914
	12	0.4092	1.2514	0.3529	1.0792	0.2813	0.8602	0.2072	0.6336	0.1397	0.4272
	13	0.4063	1.2425	0.3463	1.0587	0.2744	0.8391	0.2014	0.6159	0.1356	0.4147
	14	0.2999	0.9171	0.2293	0.7012	0.1696	0.5187	0.1212	0.3706	0.0817	0.2498
	15	0.2239	0.6847	0.2878	0.8801	0.3609	1.1037	0.4403	1.3465	0.5076	1.5523
	16	0.3039	0.9294	0.3697	1.1306	0.4420	1.3517	0.5064	1.5486	0.5555	1.6988
	17	0.3042	0.9303	0.3473	1.0621	0.3788	1.1584	0.4084	1.2489	0.4454	1.3621
	18	0.3032	0.9272	0.2872	0.8783	0.2648	0.8098	0.2421	0.7404	0.2255	0.6896
	19	0.3022	0.9242	0.2295	0.7018	0.1707	0.5220	0.1228	0.3755	0.0834	0.2550
y = +0.581	20	0.3004	0.9187	0.2242	0.6856	0.1658	0.5070	0.1189	0.3636	0.0806	0.2465
	21	0.2197	0.6719	0.1572	0.4807	0.1176	0.3596	0.0855	0.2615	0.0586	0.1792

TABLE B-7. Case 1 Heater Rod Power Measurements

Window 1: Power Skew: 2:1
Flow Rate: 2.47 gpm
Bundle Velocity: 0.327 ft/sec
T_{in} = 56.2 °F
T_{out} = 88.0 °F
ΔT_B = 31.8 °F

y location
0.0
±0.030
±0.581

Rod Number	Voltage (V)	Current (A)	P=VI (kW)	6 rod P_{total}(kW)	P_{avg} (kW/rod)
1	147.0	7.75	1.139		
2	147.0	7.75	1.139		
3	146.7	7.8	1.144	6.797	1.133
4	146.7	7.75	1.137		
5	144.8	7.75	1.122		
6	144.8	7.70	1.115		
7	103.8	5.5	0.571		
8	103.8	5.5	0.571		
9	103.6	5.5	0.570	3.409	0.568
10	103.6	5.5	0.570		
11	102.5	5.5	0.564		
12	102.5	5.5	0.564		

TABLE B-7. (continued)

Window 3: Power Skew: 2:1
Flow Rate: 2.47 gpm
Bundle Velocity: 0.327 ft/sec
T_{in} = 61.7 °F
T_{out} = 95.6 °F
ΔT_B = 33.9 °F

y location
0.0
±0.581

Rod Number	Voltage (V)	Current (A)	P=VI (kW)	6 Rod P_{total}(kW)	P_{avg} (kW/rod)
1	147.9	7.8	1.154		
2	147.9	7.9	1.168		
3	148.0	7.9	1.169	6.925	1.154
4	148.0	7.9	1.169		
5	145.2	7.8	1.133		
6	145.2	7.8	1.133		
7	103.6	5.5	0.570		
8	103.5	5.5	0.569		
9	103.3	5.5	0.568	3.405	0.568
10	103.4	5.5	0.569		
11	102.6	5.5	0.564		
12	102.7	5.5	0.565		

TABLE B-7. (continued)

Window 5: Power Skew: 2:1
Flow Rate: 2.47 gpm
Bundle Velocity: 0.327 ft/sec
T_{in} = 59.1 °F
T_{out} = 88.0 °F
ΔT_B = 28.9 °F

y location
0.0
-0.030
±0.581

Rod Number	Voltage (V)	Current (A)	P=VI (kW)	6 Rod P_{total}(kW)	P_{avg} (kW/rod)
1	147.7	7.8	1.152		
2	147.7	7.8	1.152		
3	147.3	7.9	1.164	6.870	1.145
4	147.4	7.9	1.164		
5	144.4	7.75	1.119		
6	144.4	7.75	1.119		
7	103.8	5.5	0.571		
8	103.8	5.5	0.571		
9	103.4	5.5	0.569	3.386	0.564
10	103.4	5.5	0.569		
11	102.4	5.4	0.553		
12	102.4	5.4	0.553		

TABLE B-7. (continued)

Window 7: Power Skew: 2:1
Flow Rate: 2.47 gpm
Bundle Velocity: 0.327 ft/sec
T_{in} = 60.1 °F
T_{out} = 88.6 °F
ΔT_B = 28.5 °F

y location
0.0
±0.581

Rod Number	Voltage (V)	Current (A)	P=VI (kW)	6 Rod P_{total}(kW)	P_{avg} (kW/rod)
1	147.4	7.8	1.150		
2	147.4	7.9	1.164		
3	146.6	7.9	1.158	6.923	1.154
4	146.5	7.9	1.157		
5	145.2	7.9	1.147		
6	145.2	7.9	1.147		
7	104.3	5.5	0.574		
8	104.4	5.5	0.574		
9	104.0	5.6	0.582	3.440	0.573
10	104.0	5.5	0.572		
11	103.4	5.5	0.569		
12	103.4	5.5	0.569		

TABLE B-7. (continued)

Window 9: Power Skew: 2:1
Flow Rate: 2.47 gpm
Bundle Velocity: 0.327 ft/sec
T_{in} = 61.2 °F
T_{out} = 90.2 °F
ΔT_B = 29.0 °F

y = 0.0 only

Rod Number	Voltage (V)	Current (A)	P=VI (kW)	6 Rod P_{total}(kW)	P_{avg} (kW/rod)
1	147.5	7.75	1.143		
2	147.5	7.75	1.143		
3	146.4	7.75	1.135	6.802	1.134
4	146.2	7.75	1.133		
5	145.0	7.75	1.124		
6	145.0	7.75	1.124		
7	103.9	5.5	0.571		
8	103.9	5.5	0.571		
9	102.8	5.5	0.565	3.402	0.567
10	102.7	5.5	0.565		
11	102.8	5.5	0.565		
12	102.8	5.5	0.565		

TABLE B-8. Case 2 Heater Rod Power Measurements

Window 1: Power Skew: 1:0
Flow Rate: 1.25 gpm
Bundle Velocity: 0.164 ft/sec
T_{in} = 60.6 °F
T_{out} = 93.1 °F
ΔT_B = 32.5 °F

y location
0.0
±0.581

Rod Number	Voltage (V)	Current (A)	P=VI (kW)	6 Rod P_{total}(kW)	P_{avg} (kW/rod)
1	131.7	6.9	0.910		
2	131.8	7.0	0.923		
3	131.8	7.0	0.923	5.423	0.904
4	132.0	6.9	0.911		
5	129.1	6.8	0.878		
6	129.1	6.8	0.878		

Window 3: Power Skew: 1:0
Flow Rate: 1.25 gpm
Bundle Velocity: 0.164 ft/sec
T_{in} = 59.3 °F
T_{out} = 92.4 °F
ΔT_B = 33.1 °F

y location
0.0
±0.581

Rod Number	Voltage (V)	Current (A)	P=VI (kW)	6 Rod P_{total}(kW)	P_{avg} (kW/rod)
1	132.1	6.9	0.911		
2	132.2	6.9	0.912		
3	132.5	7.0	0.928	5.437	0.906
4	132.6	7.0	0.928		
5	129.2	6.8	0.879		
6	129.2	6.8	0.879		

TABLE B-8. (continued)

Window 5: Power Skew: 1:0
Flow Rate: 1.25 gpm
Bundle Velocity: 0.164 ft/sec
T_{in} = 59.5 °F
T_{out} = 92.6 °F
ΔT_B = 33.1 °F

y location
0.0
±0.581

Rod Number	Voltage (V)	Current (A)	P=VI (kW)	6 Rod P_{total}(kW)	P_{avg} (kW/rod)
1	132.6	6.9	0.915		
2	132.7	6.95	0.922		
3	132.2	7.0	0.925	5.437	0.906
4	132.1	7.0	0.925		
5	128.7	6.8	0.875		
6	128.7	6.8	0.875		

Window 7: Power Skew: 1:0
Flow Rate: 1.25 gpm
Bundle Velocity: 0.164 ft/sec
T_{in} = 62.6 °F
T_{out} = 96.1 °F
ΔT_B = 33.5 °F

y = 0.0 only

Rod Number	Voltage (V)	Current (A)	P=VI (kW)	6 Rod P_{total}(kW)	P_{avg} (kW/rod)
1	132.3	6.9	0.913		
2	132.3	6.95	0.919		
3	132.3	7.0	0.926	5.472	0.912
4	132.6	7.0	0.928		
5	129.4	6.9	0.893		
6	129.4	6.9	0.893		

TABLE B-9. Case 3 Heater Rod Power Measurements

Window 1: Power Skew: 1:0
Flow Rate: 2.47 gpm
Bundle Velocity: 0.327 ft/sec
T_{in} = 61.1 °F
T_{out} = 93.3 °F
ΔT_B = 32.2 °F

y location
0.0
±0.581

Rod Number	Voltage (V)	Current (A)	P=VI (kW)	6 Rod P_{total}(kW)	P_{avg} (kW/rod)
1	185.3	9.8	1.816		
2	185.3	9.8	1.816		
3	184.6	9.9	1.828	10.841	1.807
4	184.2	9.9	1.824		
5	181.5	9.8	1.779		
6	181.6	9.8	1.780		

Window 3: Power Skew: 1:0
Flow Rate: 2.47 gpm
Bundle Velocity: 0.327 ft/sec
T_{in} = 61.9 °F
T_{out} = 97.5 °F
ΔT_B = 35.6 °F

y location
0.0
±0.030
±0.581

Rod Number	Voltage (V)	Current (A)	P=VI (kW)	6 Rod P_{total}(kW)	P_{avg} (kW/rod)
1	185.0	9.8	1.813		
2	185.2	9.9	1.833		
3	184.4	9.9	1.826	10.897	1.816
4	184.8	9.9	1.830		
5	182.5	9.9	1.807		
6	182.5	9.8	1.789		

TABLE B-9. (continued)

Window 5: Power Skew: 1:0
Flow Rate: 2.47 gpm
Bundle Velocity: 0.327 ft/sec
T_{in} = 61.2 °F
T_{out} = 91.8 °F
ΔT_B = 30.6 °F

y location
0.0
±0.020
±0.030
±0.040
±0.581

Rod Number	Voltage (V)	Current (A)	P=VI (kW)	6 Rod P_{total}(kW)	P_{avg} (kW/rod)
1	185.2	9.9	1.833		
2	185.1	10.0	1.851		
3	184.3	9.9	1.825	10.892	1.815
4	184.6	9.9	1.828		
5	181.4	9.8	1.778		
6	181.3	9.8	1.777		

Window 7: Power Skew: 1:0
Flow Rate: 2.47 gpm
Bundle Velocity: 0.327 ft/sec
T_{in} = 59.7 °F
T_{out} = 88.7 °F
ΔT_B = 29.0 °F

y location
0.0
+0.025
±0.581

Rod Number	Voltage (V)	Current (A)	P=VI (kW)	6 Rod P_{total}(kW)	P_{avg} (kW/rod)
1	185.4	9.85	1.826		
2	185.5	9.9	1.836		
3	184.3	9.95	1.834	10.95	1.825
4	184.2	9.95	1.833		
5	183.2	9.9	1.814		
6	182.4	9.9	1.806		

TABLE B-9. (continued)

Window 9: Power Skew: 1:0
Flow Rate: 2.47 gpm
Bundle Velocity: 0.327 ft/sec
T_{in} = 60.2 °F
T_{out} = 89.0 °F
ΔT_B = 28.8 °F

y location
0.0
+0.581

Rod Number	Voltage (V)	Current (A)	P=VI (kW)	6 Rod P_{total}(kW)	P_{avg} (kW/rod)
1	185.4	9.9	1.835		
2	185.2	9.9	1.833		
3	184.7	9.95	1.838	10.915	1.819
4	183.0	9.9	1.812		
5	181.2	9.95	1.803		
6	181.2	9.9	1.794		

APPENDIX C

UNCERTAINTY ANALYSIS

APPENDIX C

UNCERTAINTY ANALYSIS

Accuracies of the results of the combined free and forced convection study were estimated using the uncertainty method presented by Schenck.[1] Consider the general case of a result R, which is a function of the two measured variables X_m and Y_m:

$$R + r = F(X_m + x,\ Y_m + y).$$

If this function is continuous and differentiable, it can be shown with 95 percent confidence that the result R lies within the uncertainty interval W such that

$$W_r^2 = \left(\partial R/\partial X_m\right)^2 \ W_x^2 + \left(\partial R/\partial Y_m\right)^2 W_y^2.$$

VELOCITY UNCERTAINTY

For the laser anemometer, the axial velocity is directly related to the Doppler frequency F_D by the relationship

$$U = \frac{F_D \ \lambda}{2\sin \theta/2}$$

$$W_U = (\partial U/\partial\lambda)^2 \ W_\lambda^2 + (\partial U/F_D)^2 \ W_{F_D}^2 + (\partial U/\partial\theta/2)^2 \ W_{\theta/2}^2$$

It was assumed that the uncertainty of the laser light wavelength is negligible so that the first term above goes to zero. By considering instrument accuracies, the Doppler frequency uncertainty was estimated to be $W_{F_D} \simeq \pm 0.05$ kHz from 0 to 150 kHz. The half angle of the laser beam intersection was determined to be $\theta/2 = 4.584° \pm 0.0353°$ by using the above uncertainty methods, and $\lambda = 6328$ Å. For the nominal Doppler

frequency range encountered in this study, 5.0 kHz < F_D < 50.0 kHz.

$$W_U^2 = \left(\frac{\lambda}{2\sin\,\theta/2}\right)^2 W_{F_D}^2 + \left(\frac{-\lambda F_D}{2}\,\csc\theta/2\,\cot\theta/2\right)^2 W_{\theta/2}^2$$

at $F_D = 5.0$ kHz

$$W_U^2 = \left(\frac{2.076 \times 10^{-6}}{2 \times 0.079914}\right)^2 \times (0.05 \times 10^3)^2$$

$$+ \left(\frac{2.076 \times 10^{-6} \times 5 \times 10^3}{2} \times 12.514 \times 12.473\right)^2$$

$$\times (0.000616)^2 = 4.2178 \times 10^{-7} + 2.490 \times 10^{-7}$$

$$W_U = \pm 8.19 \times 10^{-4} \text{ ft/sec} \quad \text{or}$$

$$\frac{W_U}{U} = \frac{\pm 8.190 \times 10^{-4}}{0.065} \qquad \pm 1.3\%$$

at $F_D = 50$ kHz

$$W_U^2 = 4.2178 \times 10^{-7} + 2.5012 \times 10^{-5}$$

$$W_U = \pm 5.043 \times 10^{-3} \text{ ft/sec} \quad \text{or}$$

$$\frac{W_U}{U} = \frac{\pm 5.043 \times 10^{-3}}{0.650} \simeq \pm 0.8\%$$

TEMPERATURE UNCERTAINTY

The accuracy of the thermocouple temperature measurement based on the average of two calibration checks was $W_T \simeq \pm 1.0°F$. For the temperature difference between any two points in the flow, $\Delta T = T_2 - T_1$, the uncertainty is

$$W_{\Delta T}^2 = \left(\frac{\partial \Delta T}{\partial T_2}\right)^2 W_{T_2}^2 + \left(\frac{\partial \Delta T}{\partial T_1}\right)^2 W_{T_1}^2 = 1^2 \times 1^2 + (-1)^2 \times 1^2$$

$$W_{\Delta T} = \pm 1.414°F$$

The nondimensional temperature for any location was represented by

$$\overline{T} = \frac{T - T_{in}}{T_{out} - T_{in}} = \Delta T / \Delta T_B$$

Consider a nominal bundle temperature rise, $\Delta T_B = 30°F$. When $\overline{T} = 1.0$, $\Delta T = 30°F$, and the uncertainty in the nondimensional temperature is

$$W_{\overline{T}}^2 = \left(\frac{1}{\Delta T_B}\right)^2 W_{\Delta T}^2 + \left(\frac{-\Delta T}{\Delta T_B^2}\right) W_{\Delta T_B}^2$$

$$= \left(\frac{1}{30}\right)^2 \times (1.414)^2 + \left(\frac{-30}{30^2}\right)^2 \times (1.414)^2$$

$$W_{\overline{T}} = \pm 0.067 \quad \text{or}$$

$$\frac{W_{\overline{T}}}{1.0} \approx \pm 6.7\%$$

Likewise for $\overline{T} = 0.5$ and $\overline{T} = 1.5$

$$\frac{W_{\overline{T}}}{0.5} = \pm 10.5\%$$

$$\frac{W_{\overline{T}}}{1.5} = \pm 5.7\%$$

REFERENCE

1. H. Schenck, Jr., Theories of Engineering Experimentation. McGraw-Hill Book Company, New York, NY, 1961.

DISTRIBUTION

No. of Copies

OFFSITE

A. A. Churm
ERDA Chicago Patent Group
Chicago Operations Office
9800 South Cass Avenue
Argonne, IL 60439

27 ERDA Technical Information Center

2 R. J. Bariboldi
ERDA Chicago Operations Office
9800 South Cass Avenue
Argonne, IL 60439

Acting Director, Program Analysis & Evaluation Division
Energy Research & Development Administration
Idaho Operations Office
550 2nd Street
Idaho Falls, ID 83401

R. J. Neuhold
Energy Research and Development Administration
Components Engineering and Development Branch
Division of Reactor Research and Development
Washington, DC 20545

Energy Research and Development Administration
Systems and Application Studies Branch
Division of Controlled Thermonuclear Research
Washington, DC 20545

No. of Copies

S. Fabic
U.S. Nuclear Regulatory Commission
Division of Reactor Safety Reseach
Washington, DC 20555

W. Hodges
U.S. Nuclear Regulatory Commission
Division of Technical Review
Reactor Systems Branch
Washington, DC 20555

Z. Rostoczy
U.S. Nuclear Regulatory Commission
Division of Technical Review
Reactor Systems Branch
Washington, DC 20555

L. S. Tong
U.S. Nuclear Regulatory Commission
Division of Reactor Safety Research
Washington, DC 20555

M. Fontana
Oak Ridge National Laboratory
P.O. Box Y
Oak Ridge, TN 37830

W. T. Sha
Argonne National Laboratory
9700 South Cass Avenue
Argonne, IL 60439

T. Fernandez
Electric Power Research Institute
3412 Hillview Avenue
P.O. Box 10412
Palo Alto, CA 94304

B. R. Sehgal
Electric Power Research Institute
3412 Hillview Avenue
P.O. Box 10412
Palo Alto, CA 94304

No. of
Copies

J. Lipps
General Electric Company
Breeder Reactor Development
Operation
310 Deguigne Drive
Sunnyvale, CA 94086

N. E. Todreas
Department of Nuclear
Engineering
Massachusetts Institute of
Technology
Cambridge, MA 02139

A. A. Bishop
Department of Chemical
Engineering
University of Pittsburgh
Pittsburgh, PA 15213

R. A. Markley
Westinghouse Electric
Corporation
Waltz Mill Site
P.O. Box 158
Madison, PA 15663

D. Spencer
Westinghouse Electric
Corporation
Waltz Mill Site
P.O. Box 158
Madison, PA 15663

C. L. Caso
Westinghouse Electric
Corporation
P.O. Box 355
Pittsburgh, PA 15230

No. of
Copies

ONSITE

ERDA Richland Operations Office

H. E. Ransom

4 Westinghouse-Hanford

J. Hanson
J. Muraoka
J. F. Wett
J. M. Yatabe

47 Battelle-Northwest

J. M. Cuta
D. E. Fitzsimmons
C. R. Hann
B. M. Johnson
D. K. Kreid
W. W. Laity
C. A. McMonagle
D. E. Olesen
M. G. Patrick
L. T. Pedersen
M. S. Quigley (25)
C. W. Stewart
A. M. Sutey
D. S. Trent
C. L. Wheeler
R. D. Widrig
F. R. Zaloudek
Technical Information (5)
Technical Publications